Microfluidics for Liquid Biopsy toward Early Stage Cancer Diagnosis

By

Yang Yang

Submitted to the graduate degree program in Department of Chemistry and the Graduate Faculty of the University of Kansas in partial fulfillment of the requirements for the degree of Doctor of Philosophy.

Chair: Dr. Yong Zeng

Dr. Cindy L. Berrie

Dr. Robert C. Dunn

Dr. Michael A. Johnson

Dr. Fengjun Li

Date Defended: January 17th, 2020

The dissertation committee for Yang Yang certifies that this is the approved version of the following dissertation:

Microfluidics for Liquid Biopsy toward Early Stage Cancer Diagnosis

Chair: Dr. Yong Zeng

Date Approved: January 27th, 2020

Abstract

Cancer is the second leading cause of death in the United States. The most effective way to improve survival rate is to diagnose cancer at the early stage. Cancer screening has been developed for early stage cancer diagnosis. However, conventional imaging-based cancer screening methods still have many limitations to achieve early stage cancer diagnosis. For example, high doses of radiation may be delivered by some imaging methods. The size of the tumor must be big enough to be detectable. Moreover, many imaging-based methods fail to differentiate cancer tumor from benign tumor, due to the lack of detailed information. These limitations abate the capability of imaging-based cancer screening methods for early stage cancer diagnosis. In addition, further tests such as tissue biopsy may be required as supplement. Nevertheless, the invasiveness, consumption of time, localized sampling, and failure in monitoring inhibit the applications of tissue biopsy. Therefore, cancer screening methods using liquid biopsy is appealing to early stage cancer diagnosis. Liquid biopsy analyzes biomarkers in body fluids, particularly blood, for cancer diagnosis. Compared with tissue biopsy, liquid biopsy is non-invasive, rapid, less painful and risky, and capable of longitudinal monitoring. These advantages make liquid biopsy ideal for early stage cancer diagnosis. Many types of cancer biomarkers have been investigated, including circulating tumor cells (CTCs), circulating tumor DNA (ctDNA), and extracellular vesicles (EVs). However, the rarity of CTCs in blood, and the incapability of providing proteomic information in ctDNA impede their applications for early stage cancer diagnosis.

Contrarily, EVs, particularly exosomes, benefit from its abundance and comprehensive molecular profile. In the first and second projects, we have developed a microfluidic continuous-flow platform (ExoSearch chip) for rapid exosome isolation streamlined with *in situ*, multiplexed detection of exosomes. Three tumor markers on exosome surface (CA-125, EpCAM, and CD24) were detected simultaneously by a mixture of three distinct fluorophores labeled respective antibodies. In the third project, we have developed a pneumatically gated microfluidic communicating vessel (μCOVE) chip for rapid and sensitive immunomagnetic enzyme-linked immunosorbent assay (ELISA). In the last project, we have further developed the μCOVE chip for on-chip exosome capture, lysis, and digital detection of exosomal proteins. We conclude that these microfluidic platforms will contribute to liquid biopsy toward early stage cancer diagnosis.

Acknowledgements

First of all, I would like to thank my research advisor, Dr. Yong Zeng, for his generous support, patience, guidance, and encouragement. His passion of research, desire of keeping learning new things, and extensive knowledge in science build a role model for me. His attitude toward career and life will always inspire me. I also want to thank Dr. Peng Zhang, Dr. Yutao Li, Xin Zhou, Yaohua Zhang and Gopi Ravichandran from Dr. Zeng's group for their valuable help and advice. I want to thank all the faculty and staff in the Department of Chemistry, especially my committee members and academic advisor, Dr. Cindy Berrie, Dr. Robert Dunn, Dr. Michael Johnson, Dr. Fengjun Li from the Department of Electrical Engineering and Computer Science, and Megan Belaire for their generous help.

I want to thank my friends in China and the United States. Tianxiang Chen, Yang Qu, Han Mei, Xi Zhao, Weitian Yan, Zhe Yang, Zheng Zhao, Wenting Hu, and Lin Zeng. Sorry I could not name everyone here, but it is very lucky to have so many friends who care about me.

I specifically appreciate my beloved and adorable wife, soulmate and best friend, Ruiying Gao, a Ph.D. candidate and future art historian. She has been unconditionally supportive, taking care of me both in my life and my academic progress. She always encourages me when I feel losing my directions. Her love is the most precious thing to me. I am also deeply grateful to my parents and relatives in China for understanding my

absence in so many important family events. My father and mother are so supportive both emotionally and financially to my dream, and I really love and miss them.

It is unbelievable that I have spent six years at the University of Kansas and will soon leave Lawrence for my new career. I will never forget my beautiful time here.

Table of Contents

List of Figures

List of Tables

Chapter 1 Introduction

1.1 Early Stage Cancer Diagnosis

Cancer is a type of disease caused by uncontrolled abnormal cell division and growth. Twenty one percent of total deaths are caused by cancer, making it the second leading cause of death in the United States.[1] In addition, the estimated new cases in 2019 are about 1.8 million, and the estimated deaths are about 6 hundred thousand.[2] Considering that cancer remains a big threat to health, improving survival rate becomes an urgent goal for cancer treatment. If cancers can be diagnosed at the early stage, the five-year survival rate improves significantly (Figure 1-1, data from National Cancer Institute). These data suggest that the most effective way for decreasing cancer mortality is to achieve early stage cancer diagnosis.

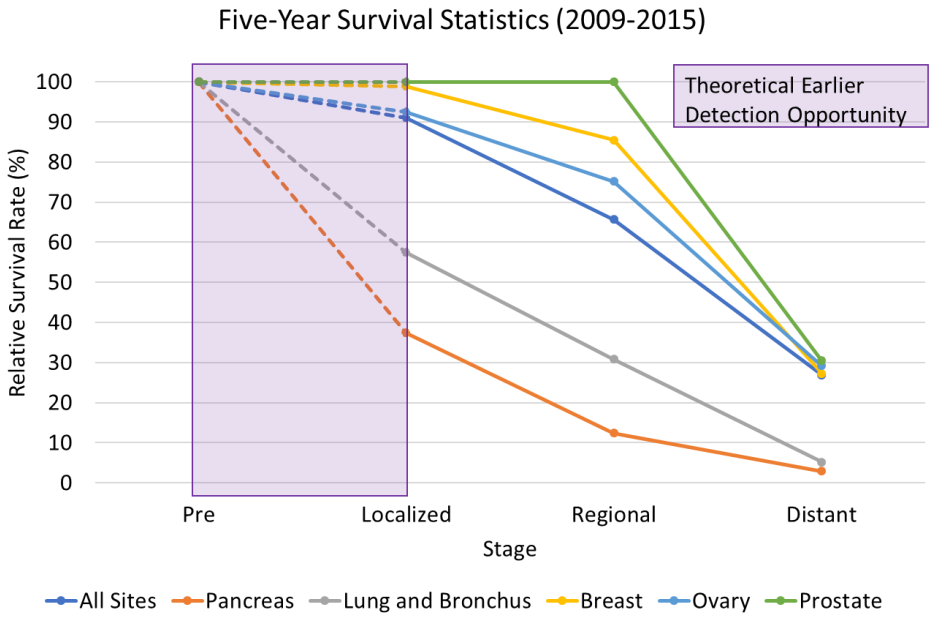

Figure 1-1. Five-year survival rate at different cancer stages. Survival rate is decreasing as cancer is spreading.

A variety of cancer screening methods have been developed for cancer diagnosis. Cancer imaging is one of the commonly used approaches, including computed tomography (CT),[3,4] positron emission tomography (PET),[5,6] ultrasounds,[7,8] and magnetic resonance imaging (MRI).[9,10] Although those imaging-based cancer screening methods play important roles in the early stage cancer diagnosis, they still have many limitations. For example, some cancers (*e.g.*, colorectal,[11] lung,[12] and breast,[13] *etc.*) can be detected by using the imaging-based methods while others cannot. Moreover, some of the methods deliver high doses of radiation, which may increase the risk of cancer. Furthermore, cancer imaging methods are limited by the size of tumor. Only tumors with certain sizes (no less than 1 mm in diameter) are detectable in cancer imaging tests, restraining imaging-based methods for the early stage cancer diagnosis.[14] Cancer imaging methods also lack detailed information and may not differentiate cancerous tumors from benign tumors.[15] Therefore, further tests (*e.g.*, tissue biopsy) are required.

Tissue biopsy is the method of retrieving a sample of tissue to examine the presence of a disease. The process is normally guided by cancer imaging to provide corroborative information and it has been widely used for cancer diagnosis.[16] However, if a tumor has spread, it is not practical to collect the tissue. In addition, due to its invasiveness, tissue biopsy fails to be done frequently for treatment monitoring. It takes days to weeks to get results from tissue biopsy. Because of these disadvantages, the development of low-cost, less invasive and rapid new cancer screening methods is extremely appealing to early stage cancer diagnosis.

1.2 Liquid Biopsy and Extracellular Vesicles

Recently, liquid biopsy has been developed for cancer screening. Unlike tissue biopsy that analyzes a sample of tissue, liquid biopsy analyzes biomarkers in body fluid, particularly blood, for cancer diagnosis (Figure 1-2). Compared with tissue biopsy, liquid biopsy has many advantages, such as non-invasiveness, less pain and risk, quick analysis, comprehensive tumor profile, and longitudinal monitoring.[17]

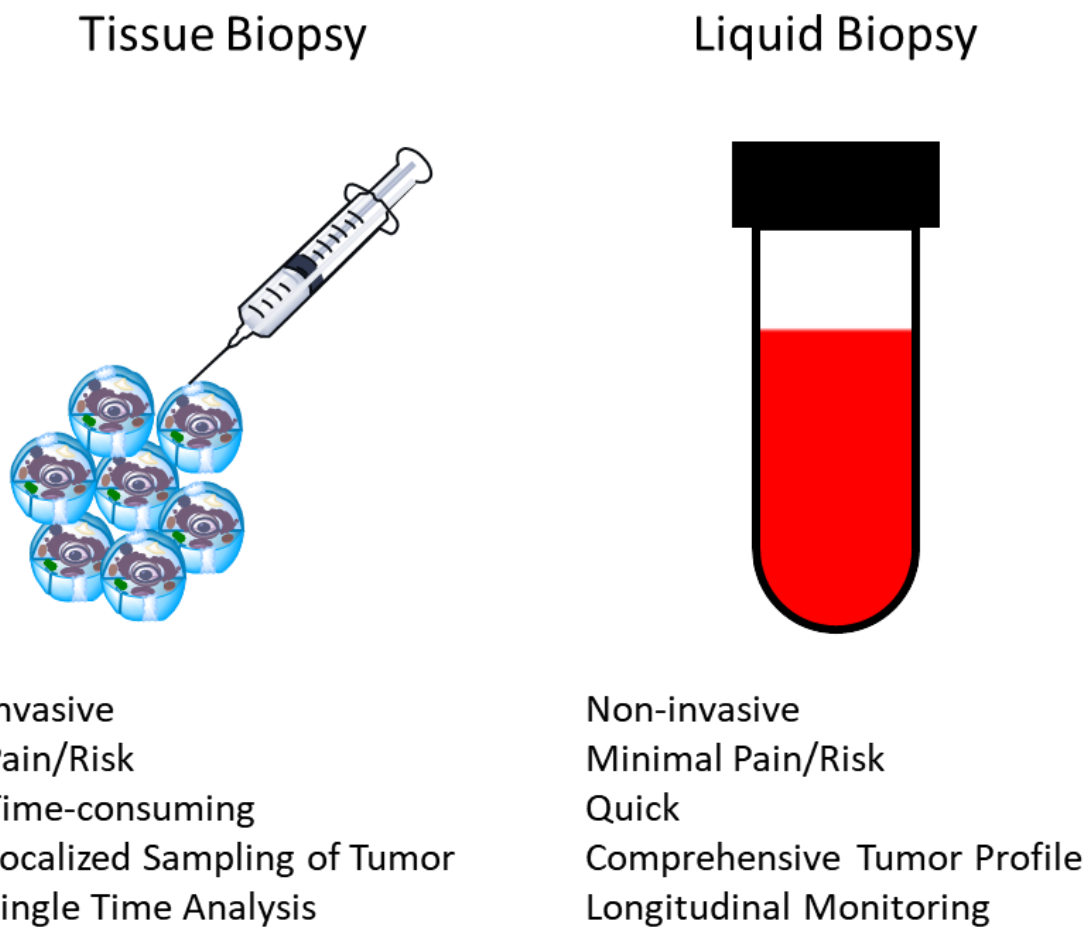

Figure 1-2. Advantages of liquid biopsy over tissue biopsy. Unlike tissue biopsy, liquid biopsy analyzes biomarkers in blood for cancer diagnosis.

The circulating components derived from cancers, including circulating tumor cells (CTCs), circulating tumor DNA (ctDNA) and extracellular vesicles (EVs), can be used as cancer biomarkers in liquid biopsy. CTCs are tumor cells shed from the primary tumor into peripheral blood. They can provide both qualitative and quantitative information through proteomic, genomic, and transcriptomic profiling (Table 1-1). Such properties make CTCs applicable for cancer diagnosis,[18,19] prognosis,[20,21] monitoring,[22,23] and therapeutics.[24,25]

In addition to CTCs, another widely used cancer biomarker is ctDNA. ctDNA is fragmented DNA (80 to 200 bp) originated from cancer cells in bloodstream. It can provide genetic information such as mutations, amplifications, methylations, deletions and translocations (Table 1-1). Many applications of ctDNA have been developed, including cancer diagnosis,[26,27] monitoring,[28,29] and genetic evolution in response to therapy.[30,31]

Table 1-1. Applications of CTCs, ctDNA, and EVs (exosomes)

	CTCs	ctDNA	EVs (exosomes)
Applications	Proteomics, Genomics, Cytogenetics, Transcriptomics, Drug Screening	Mutations, Amplifications, Methylations, Deletions, Translocations	Surface and intravesicular proteins, Genetic analysis, RNA profiling

CTCs and ctDNA are most intensively studied cancer biomarkers for liquid biopsy. Currently the US Food and Drug Administration (FDA) has approved CellSearch platform as the only clinical application of CTCs,[32] and cobas EGFR Mutation Test v2 as the only clinical application of ctDNA.[33] However, many drawbacks of these two cancer biomarkers restrict their applications as tools of liquid biopsy for early stage cancer

diagnosis. For example, the rarity of CTCs requires isolation and enrichment prior to analysis. The concentration of CTCs in whole blood is ~1–10 CTCs per mL,[34] much lower than the concentrations of white blood cells (4–10 million per mL)[35] and red blood cells (4–6 billion per mL).[36] This leads to the poor efficiency of CTCs isolation and enrichment from blood. In addition, the lack of proteomic information, low sensitivity of mutation detection, and low predictive value of single or small sets of mutations limit the clinical applications of ctDNA. Therefore, a high abundance cancer biomarker with comprehensive information is in demand in liquid biopsy for early stage cancer diagnosis.

EVs are membranous particles, ranging from 30 nm to 10 μm in diameter, released by all types of cells.[37] EVs carry biomolecules such as nucleic acids and proteins, and are present in most of body fluids, especially blood.[37,38] Based on their biogenesis and secretory pathways, EVs can be classified into two major categories: microvesicles (MVs) and exosomes (Figure 1-3).

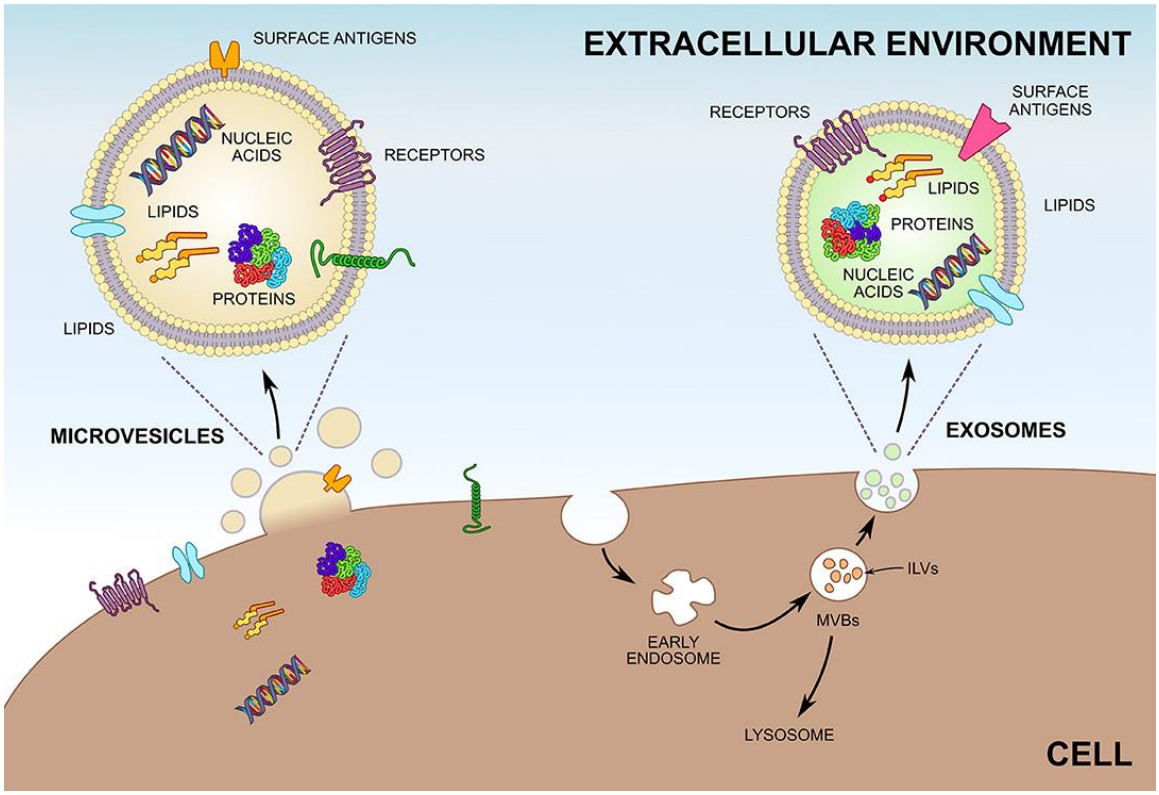

Figure 1-3. Biogenesis of microvesicles (MVs) and exosomes. Unlike MVs, which are shed directly from the plasma membrane, most exosomes are formed by invagination of endosomes and are stored within multivesicular bodies (MVBs) before release. Exosomes inside MVBs are also called intraluminal vesicles (ILVs). Upon fusion of MVBs with the plasma membrane exosomes are released into the extracellular environment. Both MVs and exosomes enclose greatly varying compositions of proteins, lipids, and nucleic acids and can be characterized by differing surface antigens (reprinted with permission).[39]

Among many types of EVs, exosomes hold a great potential as cancer biomarkers for early stage cancer diagnosis. Exosomes are cell-derived nano-sized membranous vesicles (30–150 nm) secreted from multivesicular bodies into extracellular environments (Figure 1-4), including blood, urine, and saliva.[38]

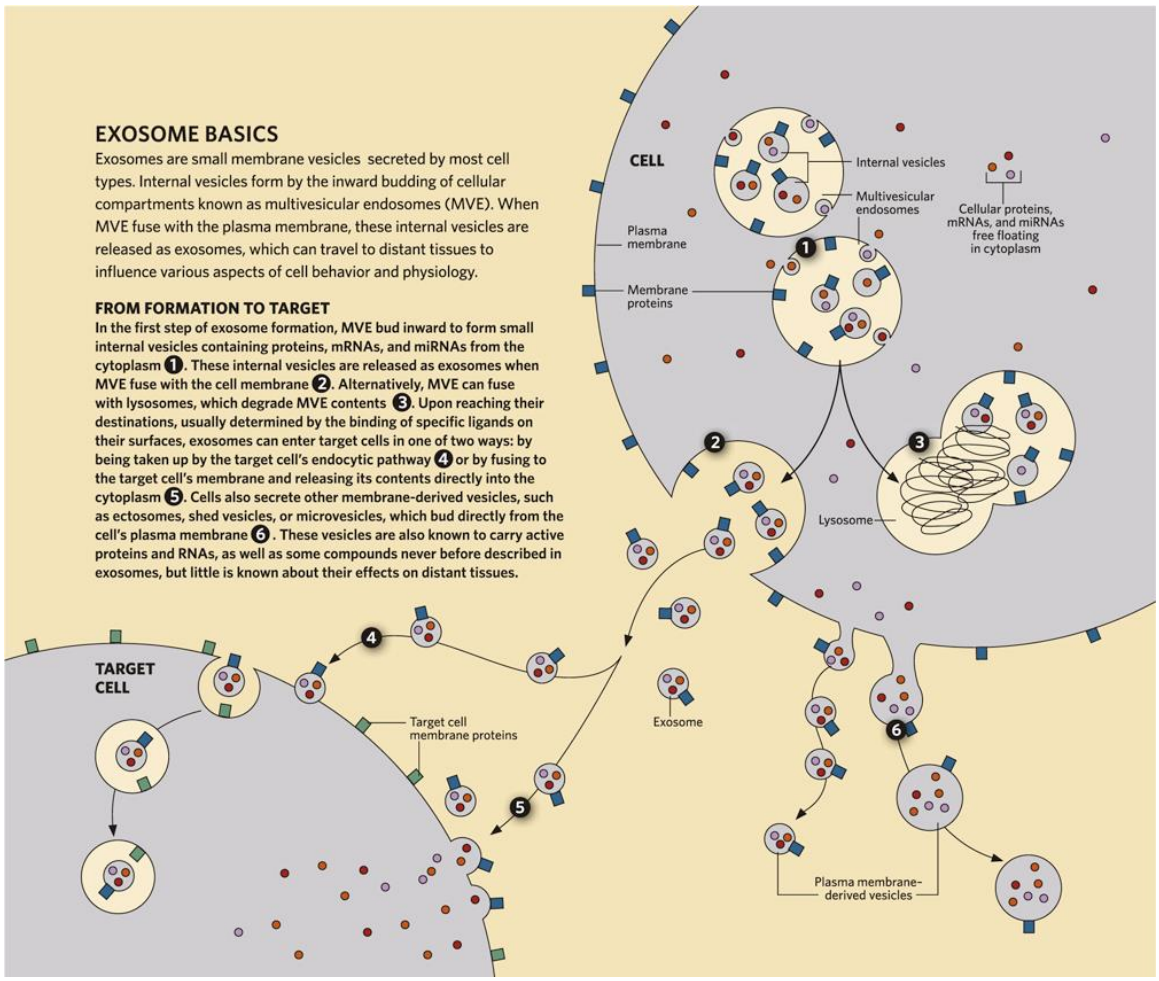

Figure 1-4. Exosome basics (reprinted with permission).[40]

Exosomes were initially considered as cellular waste products,[41] but recent studies have revealed their participation in various physiological and pathological processes, such as intercellular communication[42,43] as well as cancer progression and metastatization.[44,45] Exosomes consist of proteins, mRNAs and micro RNAs (miRNAs) (Table 1-1), reflecting the cell of origin (Figure 1-5).[38,46,47] Moreover, exosomes are over expressed by tumor cells compared with normal cells.[48,49]

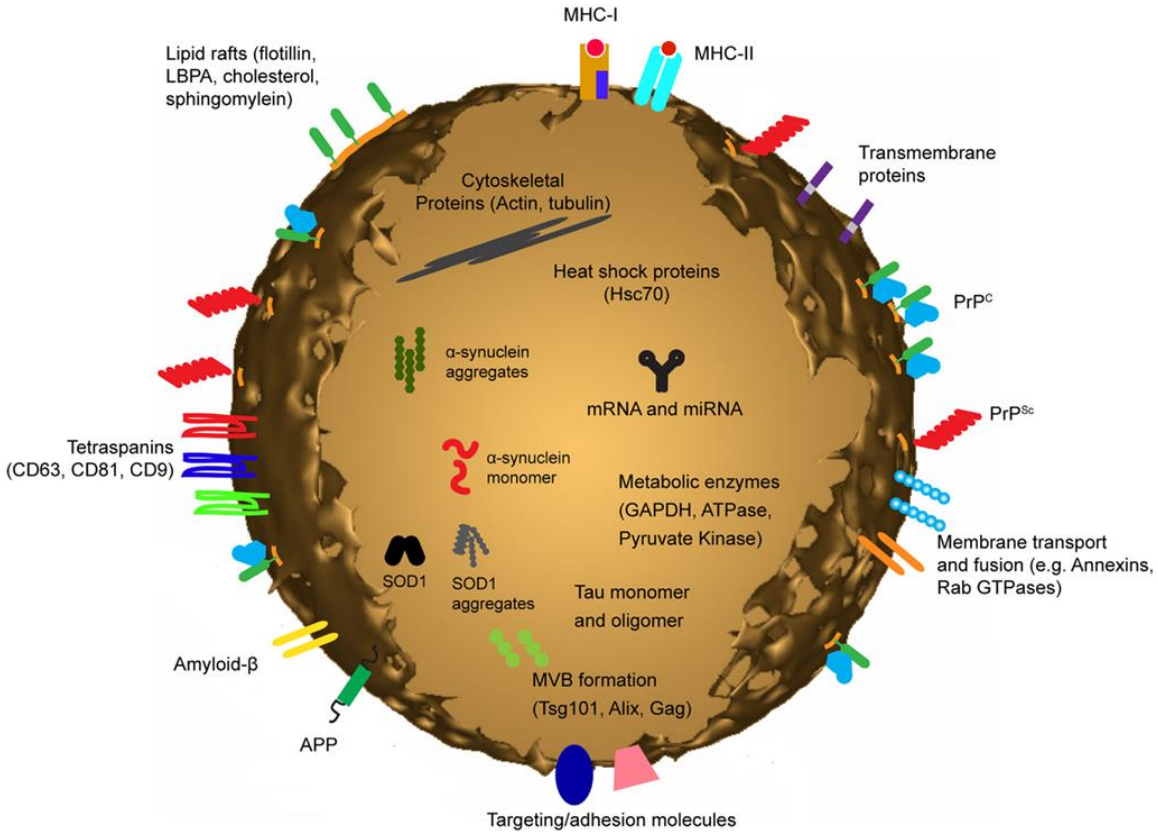

Figure 1-5. Exosomes are small membrane bound vesicles sharing similar topology to the plasma membrane. They contain mRNA and miRNA, and a vast array of different proteins depending on their host cell (reprinted with permission).[50]

Although a variety of methods have been developed, currently exosome isolation remains challenging and lacks standardized protocol.[17,38,51,52] The most commonly used method, differential ultracentrifugation, is time-consuming, yields low recovery and purity,[53] and may cause the damage and loss of exosomes.[51] Size-based exosome isolation methods such as filtration and size-exclusion chromatography (SEC) can yield moderate purity but low recovery.[51] Polymer-based precipitation can yield high recovery but low purity.[17] Immunoaffinity capture methods can isolate exosomes with high purity and specificity, but is limited to certain subpopulations of exosomes.[17,54] Even though the lack of standardized protocols and high variations between different isolation techniques

(*e.g.*, ultracentrifugation, size-base, precipitation, and immunoaffinity capture) challenge the clinical applications of exosomes, their biological properties still make exosomes ideal cancer biomarkers in liquid biopsy for early stage cancer diagnosis (Table 1-2). Recently, various commercial exosome isolation kits are being developed because of increasing interests in studying exosomes.[55]

Table 1-2. Comparison between CTCs, ctDNA, and Exosomes.

Applications	CTCs	ctDNA	Exosomes
Tumor Heterogeneity	Yes	No	Yes
Genetics (Mutations, Amplifications, Methylations, Deletions, Translocations)	Yes	Yes	Yes
Proteomics	Yes	No	Yes
RNA Profiling	Yes	No	Yes
Phenotypic Analysis of Cells	Yes	No	No
Biobanking Preservation	No	Yes	Yes

1.3 Immunoassays

Expression levels of tumor-related exosomal proteins can indicate the presence of cancers,[56] which requires quantitative protein analysis. Immunoassays utilize antibodies to specifically recognize and measure proteins. Because of the high sensitivity, specificity, precision, and throughput, immunoassays, particularly enzyme-linked immunosorbent assay (ELISA), are known as gold standard for protein quantification. In general, immunoassays can be categorized into three formats: direct, indirect, and sandwich platforms (Figure 1-6). In direct immunoassays, the dye-labeled (fluorescence or luminescence) primary antibody binds to the analyte coated on a solid surface. In indirect immunoassays, the primary antibody first binds to the analyte coated on a solid

surface, followed by the dye-labeled secondary antibody binding to the primary antibody. In sandwich immunoassays, the capture antibody is first immobilized on a solid surface, followed by binding of the analyte and dye-labeled detection antibody. The quantitative information relies on measuring the signals from the dye.

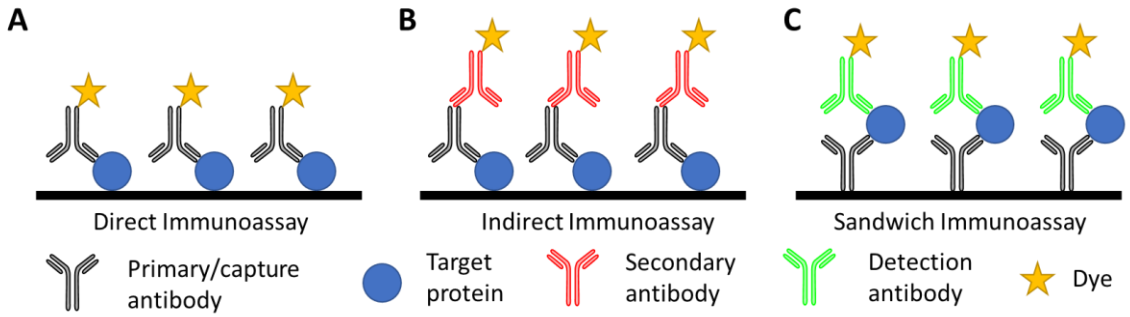

Figure 1-6. Formats of immunoassays. (**A**) Direct immunoassays. The dye-labeled primary antibody binds to the target protein immobilized on a solid surface. (**B**) Indirect immunoassays. The primary antibody binds to the target protein immobilized on a solid surface, followed by the dye-labeled secondary antibody binding to the primary antibody. (**C**) Sandwich immunoassays. The target protein binds to the capture antibody immobilized on a solid surface, followed by the dye-labeled detection antibody binding to the target protein.

In addition, ELISA has been developed and widely used in immunoassays. Instead of labeling the detection antibody with a dye, an enzyme is conjugated with the detection antibody. The signal is generated by enzymatic reactions between the enzyme and the enzymatic substrate (Figure 1-7). Compared with traditional immunoassays, ELISA significantly improves the sensitivity and reduces the limit of detection, as a result of signal amplification by enzymatic reactions. Over the past few decades, enormous new ELISA platforms have been innovated. Conventional ELISA is performed on a 96-well plate. Owing to the automated equipment (*i.e.*, liquid handler and microtiter plate reader),

higher-throughput 384- and 1536-well formats have been developed.[57,58] Moreover, the development of surface modification methods contributes to enhanced immobilization of antibody with improved bioanalytical performance,[59,60] comparing to passive absorption in conventional ELISA. One of the current trends in ELISA moves toward microfluidic ELISA for ultra-sensitive protein quantification. To date, numerous commercial platforms of immunoassays such as ExoTEST, ExoELISA Complete Kit and ExoQuant ELISA Kit have been developed for exosomal protein detection.

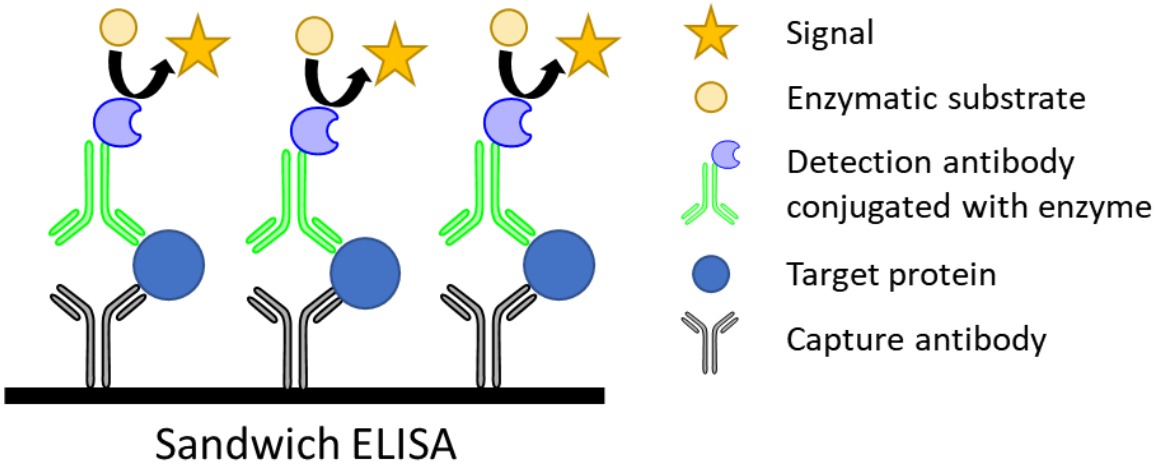

Figure 1-7. Sandwich ELISA. The capture antibody is firstly immobilized on a solid surface. The target protein is then captured, followed by the enzyme-labeled detection antibody binding to the target protein. Signals are generated by the enzymatic reaction of the substrate.

1.4 Microfluidics and Digital Measurements

The definition of microfluidics is broad and complex. In general, microfluidics is a growing technique that manipulates small scales of fluids (nanoliter to microliter) with precise control. A microfluidic device is also referred as "lab-on-a-chip" and "micro total analysis system (μTAS)," since a single device can integrate with many functional

components (*e.g.*, isolation,[61] purification,[62] separation,[63] detection,[64] *etc.*). Due to its flexibility, microfluidics has been used in multiple disciplines, including physics, chemistry, engineering, and biotechnology.

Microfluidic devices can be fabricated from diverse materials, including silicon, glass, paper, and polymers. Silicon and glass were the first materials used to fabricate microfluidic devices,[65,66] owing to the microfabrication technology originated from semiconductor industry. Nonetheless, the microfabrication process of silicon and glass is cumbersome, high-cost and complicated. Therefore, researchers started to use alternative materials. Microfluidic paper-based analytical devices (μPAD) were firstly developed twelve years ago.[67] The fabrication relying on printing hydrophobic patterns is simple and inexpensive, yet the evaporation of reagents and the difficulty in precise control of flow challenge the utilization of μPAD. Polymeric materials can be divided into two types: thermoplastics such as poly(methyl methacrylate) (PMMA), and elastomers such as poly(dimethylsiloxane) (PDMS). Since the first introduction of PDMS to microfluidics in 1988,[68] it has become the dominant materials to fabricate microfluidic devices.[69] Benefiting from its elastomeric properties, PDMS facilitates the fabrication of multi-layer microfluidic devices with pneumatic valves and pumps to precisely control fluids.[70] Based on the structures, the pneumatically actuated microvalves are categorized into two types: normally-open[70-72] and normally-closed valves,[73-75] as shown in Figure 1-8. Additionally, if multiple microvalves are arrayed (three or more) and actuated in a proper manner, they can be transformed as micropumps.[76] Figure 1-9 shows an example of a two-layer PDMS microfluidic chip with pneumatic micropumps and microvalves fabricated in our lab.

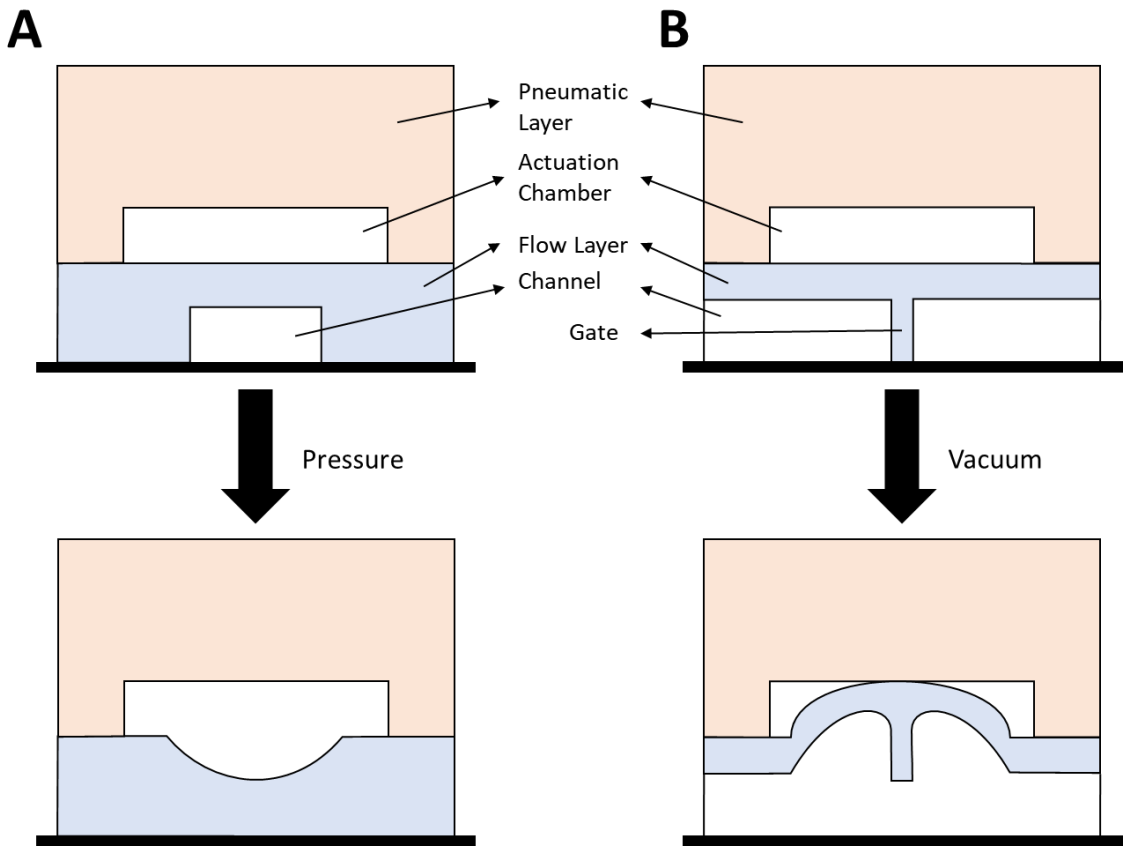

Figure 1-8. Pneumatically actuated microvalves. (**A**) A normally-open microvalve is closed by pressure. (**B**) A normally-closed microvalve is opened by vacuum.

PDMS microfluidic devices are easy to fabricate as a single mold can produce dozens of microfluidic chips. Moreover, a microfluidic device is low-cost and highly affordable. Furthermore, microfluidic devices can yield high throughput, as an array of reactors can be replicated on a single chip and the operation can be fully automated. Most importantly, due to the ability to control small amounts of fluids, microfluidics can significantly reduce sample consumptions, increase the sensitivity, and achieve rapid analysis. Such advantages expand the utilization of microfluidics in numerous applications, including immunoassays,[77-79] polymerase chain reaction (PCR),[80-82] cell

counting and sorting,[83-85] DNA sequencing,[86,87] drug discovery,[88,89] single-cell analysis,[90-93] as well as liquid biopsy.[94-99]

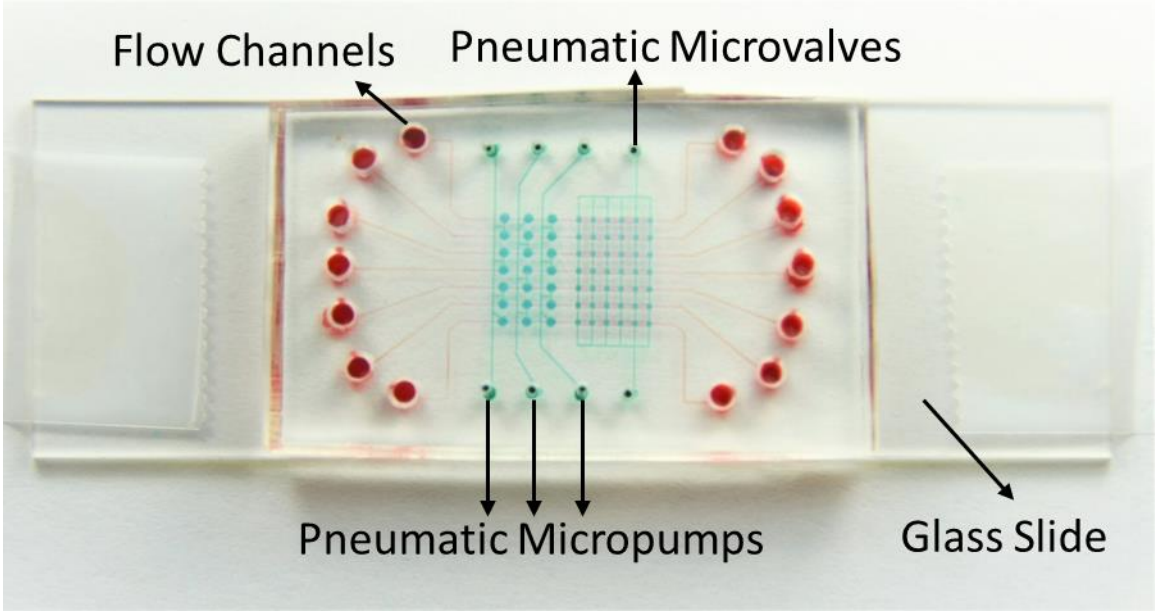

Figure 1-9. Photograph of a two-layer PDMS microfluidic chip with multiple flow channels, micropumps, and microvalves. The flow channels on the bottom layer are in red, and the pneumatic micropumps and microvalves on the top layer are in green.

Unlike analog measurements that rely on detecting signal intensity in a bulk solution, digital measurements rely on counting on/off signal readouts (Figure 1-10). As a consequence, digital measures are characterized by extremely low background and limit of detection, as well as high sensitivity. The inherent ability of microfluidic devices to manipulate tiny amount of fluids makes them a perfect fit in digital measurements. The limit of detection of some assays is down to single-molecule level.[100,101]

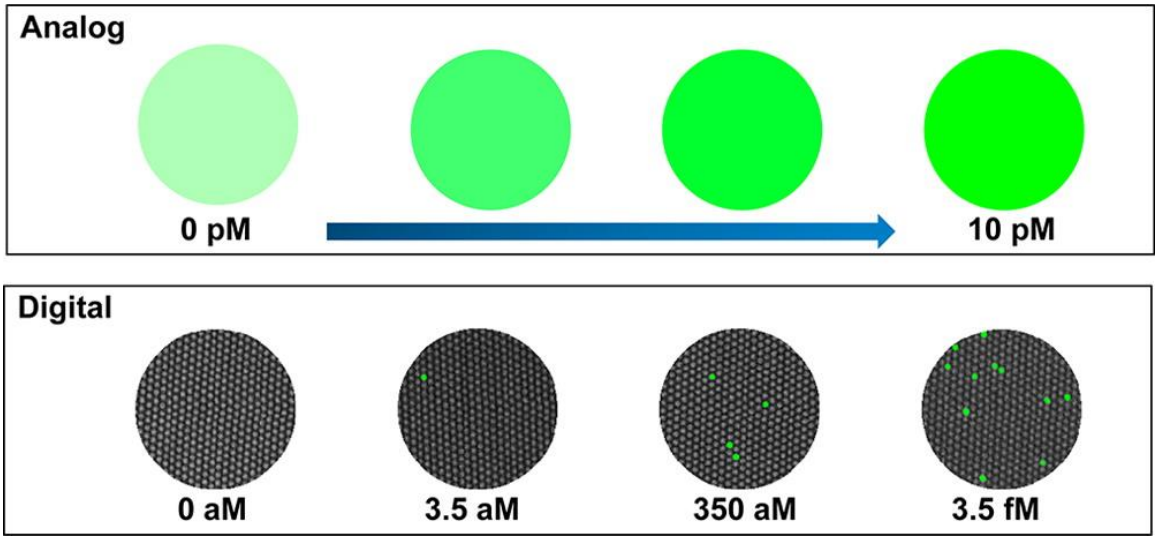

Figure 1-10. Top: Analog measurements give increasing intensity as the concentration increases. Bottom: In contrast, digital measurements are independent of intensity and simply rely on a signal/no signal readout (reprinted with permission from American Chemical Society).[102]

A variety of microfluidic digital detection platforms have been developed for highly sensitive molecular profiling, including droplet,[103-105] microwell,[106,107] microchannel with chamber,[80,93,108] and printing.[109] However, most of them require multi-phase (oil/water) based sample dispersion and geometry of the microfluidic devices. For example, droplet-based methods need immersible phase to encapsulate aqueous droplets (Figure 1-11A), and microwell-based methods need oil to sweep out excess reagents for isolating individual microwells (Figure 1-11B), introducing extra complexity in experimental operations. We tried to address this issue in Chapter 5 by developing a novel microfluidic platform for single-phase signal digitization.

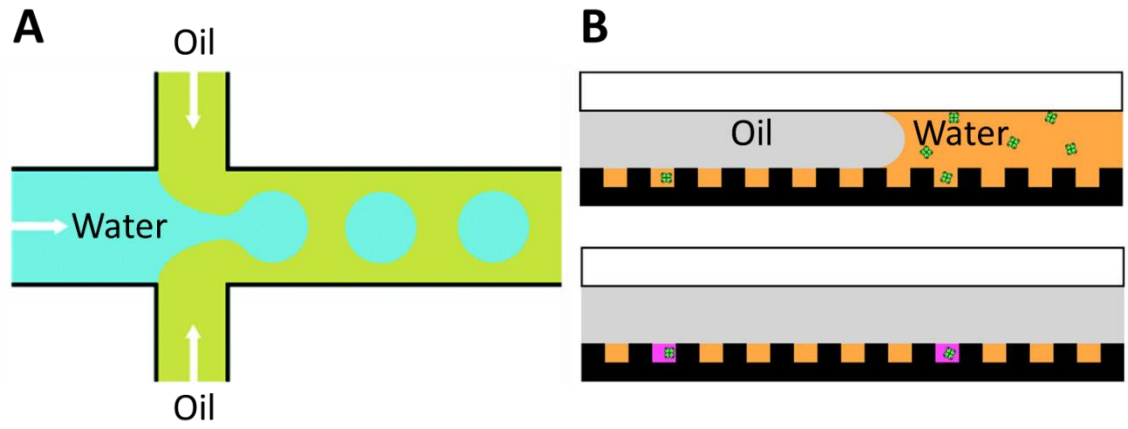

Figure 1-11. (**A**) Aqueous phase is dispersed into continuous oil phase to generate droplets (reproduced with permission from the Royal Society of Chemistry).[110] (**B**) Oil phase flows into the channel to displace the aqueous phase and to seal the microwells. (reproduced with permission from American Chemical Society).[111]

1.5 Chapter Overview

Tumor-derived circulating exosomes, enriched with a group of tumor antigens, have been recognized as a promising biomarker source for cancer diagnosis *via* a less invasive procedure. Quantitatively pinpointing exosome tumor markers is appealing yet challenging. In the first and second projects (Chapter 2 and Chapter 3), we developed a simple microfluidic approach (ExoSearch chip) which provides enriched preparation of blood plasma exosomes for *in situ*, multiplexed detection using immunomagnetic beads.[99] The ExoSearch chip offers a robust, continuous-flow design for quantitative isolation and release of blood plasma exosomes in a wide range of preparation volumes (10 μL to 10 mL). We employed the ExoSearch chip for blood-based diagnosis of ovarian cancer by multiplexed measurement of three exosomal tumor markers (CA-125, EpCAM, CD24) using a training set of ovarian cancer patient plasma, which showed significant diagnostic power and was comparable with the standard Bradford assay. This work provides an

essentially needed platform for the utilization of exosomes in clinical cancer diagnosis, as well as fundamental exosome research.

Rapid, sensitive analysis of protein biomarkers is of tremendous biological and clinical significance. Immunoassay is a workhorse tool for protein analysis and has been under continuous investigations to develop new methods and to improve the analytical performance. In the third project (Chapter 4), we have developed a pneumatically gated microfluidic communicating vessel (μCOVE) chip for rapid and sensitive immunomagnetic ELISA.[79] A distinct feature of our device is that it employs the communicating vessel principle as a simple means to generate fast transient hydrodynamic flow to enable effective flow washing without the need of excessive incubation, which, compared to conventional microfluidic flow-based immunoassays, greatly simplifies and expedites the assay workflow. The stationary multi-phase microfluidic techniques have been developed for fast bead washing. However, they have some limitations, such as the need of careful control of interfacial properties, large bead quantity required for reliable interphase bead transport, and relatively high bead loss during surface tension-gated traverse. Our signal-phase μCOVE chip can overcome such limitations and facilitate the manipulation of magnetic beads to streamline the assay workflow.

We showed that the μCOVE device afforded highly sensitive quantification of carcinoembryonic antigen (CEA) and epidermal growth factor receptor (EGFR) proteins with the limit of detection (LOD) down to the sub-picogram per mL level. Direct detection of EGFR in the crude A431 cell lysate was also demonstrated to further validate the ability of our device for rapid and quantitative analysis of complex biological

samples. Overall, the μCOVE chip presents a unique platform that combines the merits of the stationary multi-phase systems and the flow-based microfluidics. This novel immunoassay microsystem holds promising potential for a broad range of biological and clinical applications, owing to its simplicity and high performance.

In the last project (Chapter 5), we have integrated the design of the μCOVE chip with downstream lysis and detection chambers to achieve on-chip exosome capture, lysis, and digital detection of exosomal proteins. We intentionally chose a special enzymatic substrate, enzyme-labeled fluorescence 97 phosphatase substrate (ELF 97) for single-phase signal digitization, because of the insolubility of its dephosphorylated product (ELF 97 alcohol). Furthermore, a special detection chamber was fabricated to enhance the localization of ELF 97 alcohol precipitates. We validated the feasibility of this chip by microfluidic digital sandwich ELISA to quantify the human epidermal growth factor receptor 2 (HER2) standard proteins and its expression level in exosomes secreted from MDA-MB-453 cells. This prototype of microfluidic platform is very promising for a broad range of clinical applications.

Chapter 2 Development of A Microfluidic ExoSearch Chip for Exosome Isolation[*]

2.1 Introduction

Extracellular vesicles, particularly exosomes, have become essential for intercellular communications involved in many pathophysiological conditions, such as cancer progression and metastasis.[46,112-116] Exosomes are a distinct population of small microvesicles (30–150 nm) that are released from multivesicular bodies (MVBs) through an endolysosomal pathway, as opposed to other subcellular membrane derived vesicles.[38,46] Studies have shown that exosomes are abundant in cancer patient blood.[49,117,118] Probing of tumor-derived circulating exosomes has been emerging to better aid in non-invasive cancer diagnosis and monitoring of treatment response.[119] However, exosome biogenesis at the molecular level is still not well understood, as well as clinical utilization of exosomes lags, due to current technical challenges in rapid isolation and molecular identification of exosomes.[38,120]

The most common procedure for purifying exosomes involves a series of high-speed ultracentrifugation steps in order to remove cell debris and pellet exosomes. However, this procedure does not discriminate exosomes from other vesicular structures or large protein aggregates.[121-123] Moreover, the isolation protocols are extremely tedious, time-consuming (> 10 h), and inefficient, especially for blood samples, making clinical application difficult.[124-127] Although physical size is employed to define exosomes, this property has not completely distinguished exosomes as a specific population apart from

[*] Published on *Lab Chip* **2016**, *16*, 489-496.

other vesicles that originate from different cellular locations, such as apoptotic vesicles, exosome-like vesicles, membrane particles, and ectosomes.[115] Exosomes carry specific proteins, RNAs, and mitochondrial DNA, that represent their cells of origin.[128,129] The molecular signature of exosomes is essential for defining exosome populations and origins.[130,131] However, conventional flow cytometry for molecular marker identification is limited by detectable size (> 200 nm), thereby excluding the majority of exosomes.[132] Standard benchtop ultracentrifugation, western blotting and enzyme-linked immunosorbent assay (ELISA) require lengthy processes and large amounts of purified, concentrated exosomes from blood (~2 mL) or cell culture media (~300 mL).[122,133]

Herein, we developed a simple and robust microfluidic continuous-flow platform (ExoSearch chip) for rapid exosome isolation. Several microfluidic approaches have been previously developed for exosome studies,[134,135] such as isolation,[136,137] quantification,[138,139] and molecular profiling.[140-142] However, these platforms require either complicated fabrication or sophisticated sensing methods. We previously developed a microfluidic system for integrated exosome lysis and detection of intravesicular protein markers that exosomes carry.[135] Nevertheless, the previous approach involves off-chip exosome capture using a small amount of magnetic beads and thus lacks the ability to prepare large-scale enriched exosomes for variable downstream molecular characterizations. Therefore, we developed the ExoSearch chip which enabled on-chip continuous-flow mixing and immunomagnetic isolation. Compared to other existing microfluidic methods, the ExoSearch chip possesses distinct features: first, the continuous-flow operation affords dynamic scalability in processing sample volumes from microliter for on-chip analysis to milliliter preparation for variable downstream

measurements; second, because of its simplicity, cost-effectiveness, and robustness, the ExoSearch chip holds the potential to be developed into a viable technology in point-of-care and clinical settings.

2.2 Experimental

2.2.1 ExoSearch Chip Fabrication and Operation

The microfluidic chip was fabricated using a 10:1 mixture of PDMS base and curing agent over a master wafer, and then bounded with a microscope glass slide. The master was the pattern of SU-8 photoresist on a 4-inch silicon wafer and was silanized to facilitate the generation of many replicas as needed. A 2 mm magnet disk was molded into a PDMS layer during the curing process at the desired location; the magnet is removable for switching off magnetic force. A surface treatment for the PDMS chip was applied to avoid non-specific adsorption and generation of bubbles in the microchannel, using a blocking buffer (2.5% BSA and 0.01% Tween-20 in 1× PBS) with 30 min flushing at a flow rate of 1 μL min^{-1}. A programmable syringe pump (picoliter precision) with two 20 μL microsyringes was used to provide the optimized flow rate for continuous, on-line mixing of the plasma sample and immunomagnetic beads. The magnetic beads (2.8 μm, 0.1 mg mL^{-1}) were conjugated with capture antibodies for isolating intact plasma exosomes. A washing buffer (1% BSA in 1× PBS) was applied for 5 min after exosome capturing.

The size distribution and concentration of nanoparticles can be measured by nanoparticle tracking analysis (NTA) based on analyzing Brownian motion. NTA was performed using NanoSight V2.3 following the standard protocols. By monitoring the

trajectory of microvesicle movement, the particle numbers within the size range of 0–500 nm were estimated in serial dilutions. The concentrations were calibrated back to the human plasma concentration. For consistent reading, the measurement settings were optimized, and five replicas were performed to obtain the average measurements. Transmission electron microscopy (TEM) and image analysis were performed for characterizing the morphology and size of the exosomes captured on the bead surface. The agar and resin embedding protocols were employed to ensure that the exosome morphology was maximally maintained under TEM imaging. Ultra-thin sections (80 nm) were cut on a Leica Ultracut-S Ultramicrotome and viewed after counterstaining in a JEOL JEM-1400 Transmission Electron Microscope operating at 80 kV. Micrographs were prepared to a known scale, and exosome sizes were measured and calculated using TEM imaging software with a ruler function at 20 K magnification and normalized to the scale bar.

2.2.2 Reagents, Data Collection and Analysis

The capture antibodies used in this study are CD9 biotin (C3-3A2, Ancell), CD81 biotin (1.3.3.22, Ancell), and CD63 biotin (H5C6, BioLegend). Exosome capture beads (Dynabeads M-270 Streptavidin, 2.8 μm in diameter) were obtained from Invitrogen and coupled with capture antibody through biotin-streptavidin linkage per the instruction, generating typical binding capacity of ~10 μg biotinylated antibody per 1 mg of beads. Antibody-coated beads (0.1 mg mL^{-1}) were introduced into microfluidic device for mixing with human blood plasma at variable flow rates precisely controlled by a programmable syringe pump. The human blood plasma was obtained from University of

Kansas Cancer Center's Biospecimen Repository following consents and standard protocols.

Fluorescence images were collected by an inverted epifluorescence microscope with a 20× (N.A. = 0.35) Zeiss objective lens and a scientific CMOS camera (OptiMOS, QImaging). The camera exposure time was set to 2000 ms with a 10 MHz frequency controlled by the open source software Micro-Manager 1.4.

2.3 Results and Discussion

2.3.1 Working Principles of the ExoSearch Chip

Exosomes contain a variety of surface markers originating from their host cells.[143,144] Selective isolation and specific analysis of disease-responsive exosome subpopulations are essential to evaluate the clinical relevance of circulating exosomes.[132,145-147] To this end, the ExoSearch chip is designed to specifically isolate exosome subpopulations and simultaneously measure a panel of tumor markers for better defining disease, compared to single-marker detection. As shown in Figure 2-1A, the ExoSearch chip consists of a Y-shaped injector, a serpentine fluidic mixer for bead-based exosome capture (~25.5 cm in length), and a microchamber (4 mm in diameter) with a replaceable magnet for collection and detection of exosomes. The microchannel is 300 μm wide and 50 μm deep. Such microfluidic geometry was adapted from our previous studies on on-chip mixing and magnetic bead capture.[135] The operation was simply driven by a programmable microsyringe pump with picoliter resolution. In brief, a plasma sample and immunomagnetic beads were introduced at the same flow rate from the injection channels (Figure 2-1B) through the long serpentine channel where they were

uniformly mixed to facilitate exosome binding with the beads (Figure 2-1C). No significant aggregation of beads by interactions with exosomes or other plasma components was observed during flow mixing at the bead concentrations and flow rates used here (Figure 2-1B and C). Magnetic beads with bound exosomes can be retained as a tight aggregate in the downstream microchamber by magnetic force (Figure 2-1D). The amount of beads retained in the chamber was found to be proportional to the injection volume, allowing for quantitative isolation and detection of exosomes.[135] Total analysis was completed with as low as 20 μL plasma samples in ~40 min. The beads were then released by removing the magnet and collected off the chip to yield purified and enriched exosome samples for variable benchtop measurements, such as morphological studies by transmission electron microscopy (Figure 2-1E and Figure 2-2).

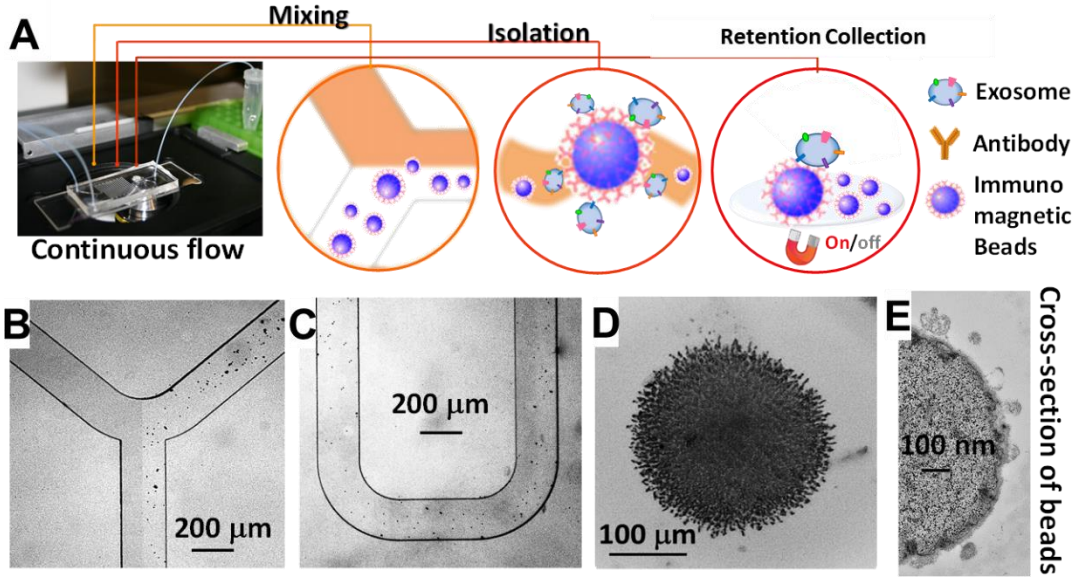

Figure 2-1. (**A**) Workflow of the ExoSearch chip for continuous mixing and isolation. (**B**)–(**C**) Bright-field microscope images of immunomagnetic beads manipulated in the microfluidic channel for mixing and isolation of exosomes. (**D**) Exosome-bound immunomagnetic beads aggregated in the microchamber with an on/off switchable magnet for continuous collection and release of exosomes. (**E**) TEM image of an exosome-bound immunomagnetic bead in a cross-sectional view.

While a 20 μL sample volume was used throughout this study, the smallest sample volume that can be reliably handled was estimated to be 10 μL, given the dead volume of the system (*i.e.*, syringes, tubing and the chip). Our previous results showed that the magnetic bead aggregate formed in the chamber increased linearly in size by a factor of 8 with a 50-fold increase in the total injected bead number.[135] Note that ~10^6 beads formed an aggregate of ~1 mm size. Based on the chamber size (4 mm in diameter) and the bead concentration used (~10^6 per mL), it is reasonable to estimate that this device can readily process 10 mL of plasma in a single continuous run. The processing capacity can be increased by operating in a repetitive capture-and-release manner (Figure 2-2). The single-channel device is readily scaled up to multi-channel systems for high-throughput exosome immuno-isolation and analysis.

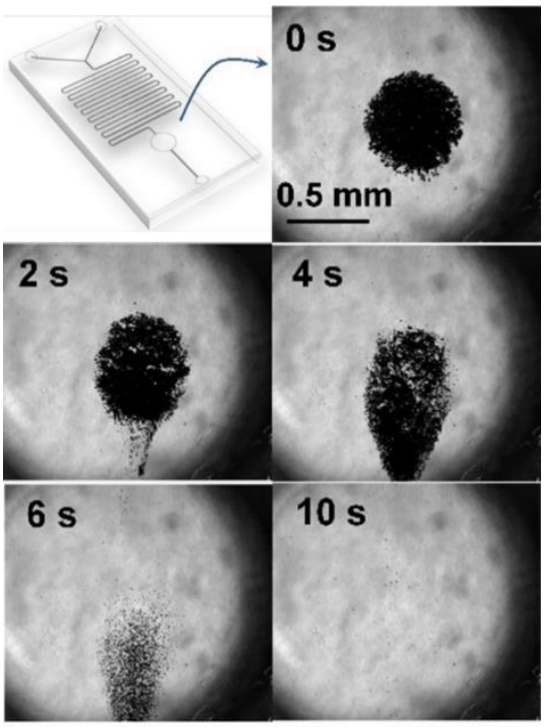

Figure 2-2. The sequential snapshots showing the release process of bead aggreagates after switching off the magnetic field during continuous flow in ExoSearch chip.

2.3.2 Characterization of Microfluidic Continuous-flow Mixing for Exosome Isolation

We systematically characterized the on-chip mixing behavior of particles in various sizes for efficient exosome isolation. First, fluorescently labeled nanoparticles (50 nm) and micro-sized magnetic beads (2.8 μm) were flowed through the ExoSearch chip, respectively, in order to mimic the mixing process for exosome isolation (Figure 2-3A). In both cases, two streams were well mixed passively by the serpentine channel, showing uniform distribution of particles across the channel width. Mixing of fluorescently labeled exosomes with antibody-conjugated microbeads was then studied. We observed uniform distributions of both exosome stream and microbeads that emitted bright fluorescence due to the binding of exosomes on the bead surface (Figure 2-3A). The microbeads were dominant for effective mixing which leads to much faster mixing. The minimum flow travel distance required for complete mixing in the microchannel was measured for each case, which exhibited a linear semi-log response to the flow rates applied (50 to 10^4 nL min^{-1}) (Figure 2-3B). Higher mixing efficiency was observed at relatively low flow rates for all three cases. Low-Reynolds-number conditions allow the exosomes and magnetic-bead suspension to flow side by side. Thus, complete mixing is critical and determines the effective residence time (incubation time), which in turn determines the effective capture. In the serpentine microchannel, mixing is promoted by the Dean flow and inertial lift.[148] For larger particles, the lift force increases rapidly and positions the particles across the channel.[149] Therefore, compared to the smaller exosomes and nanoparticles, the micro-sized magnetic beads showed faster mixing (Figure 2-3). In addition, in such a mixing system, the shear stress is low and particularly

suitable for isolating and collecting intact exosomes.[148,149] For all flow rates we studied (50 to 10^4 nL min^{-1}), effective mixing was completely achieved, which can significantly reduce the incubation time for efficient immunomagnetic capture of exosomes.[150] We also investigated the exosome capture efficiency by comparing the fluorescence intensity of flows at the inlet and outlet of the capture chamber.

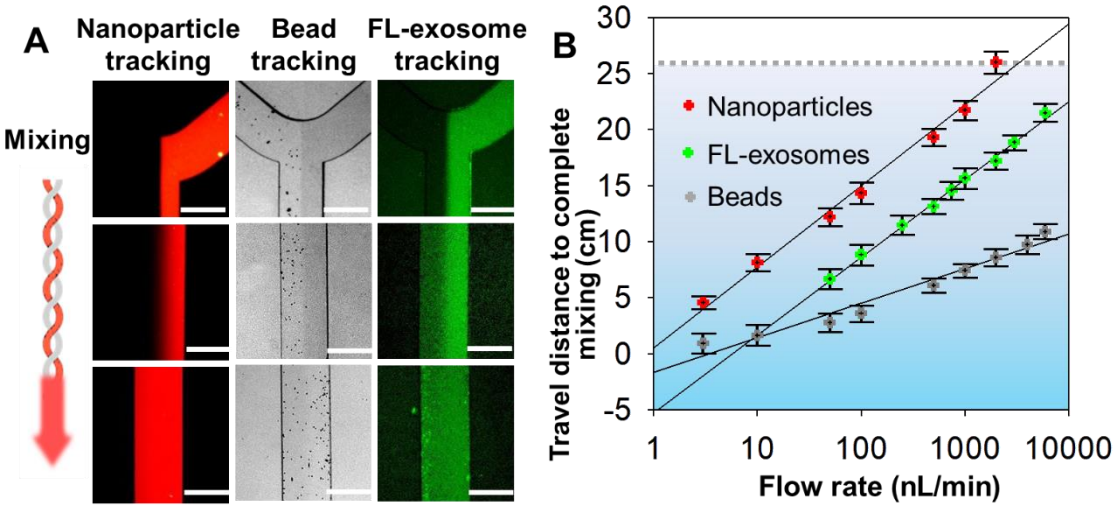

Figure 2-3. Microfluidic continuous-flow mixing for efficient exosome isolation. (**A**) Two-stream particle mixing in the microchannel. Left: Fluorescence charge-coupled device (CCD) images of the mixing process for a stream of Texas Red labeled nanoparticles (50 nm) co-flowed with a bead solution. Middle: Immunomagnetic beads (2.8 μm) tracked under bright field for mixing with human blood plasma. Right: Mixing of fluorescently labeled exosomes with antibody beads. Exosomes were purified from ovarian cancer patient plasma by ultracentrifugation. Scale bars: 300 μm. (**B**) Plots of the minimum travel length required for uniform mixing over a flow rate range. The grey dashed line indicates the mixing channel length in the ExoSearch chip.

The capture efficiency of 42–97.3% was achieved at flow rates from 50 to 10^4 nL min^{-1} (Figure 2-4). Subsequent studies were performed at the flow rate of 1 μL min^{-1}, which resulted in a fairly good capture efficiency of 72%. This flow speed allows exosome isolation from a 20 μL plasma sample in 20 min. For preparing enriched

exosomes from large-volume samples, the throughput can be increased by using a relatively faster flow rate or expanding the single-channel device to a multi-channel system. For instance, a 2 mL blood plasma can be processed within 3 h (10 μL min^{-1}) without the need of manual intervention, which is at least 3 times faster than standard ultracentrifugation for processing the same amount of plasma with only 25% exosome recovery rate.[151]

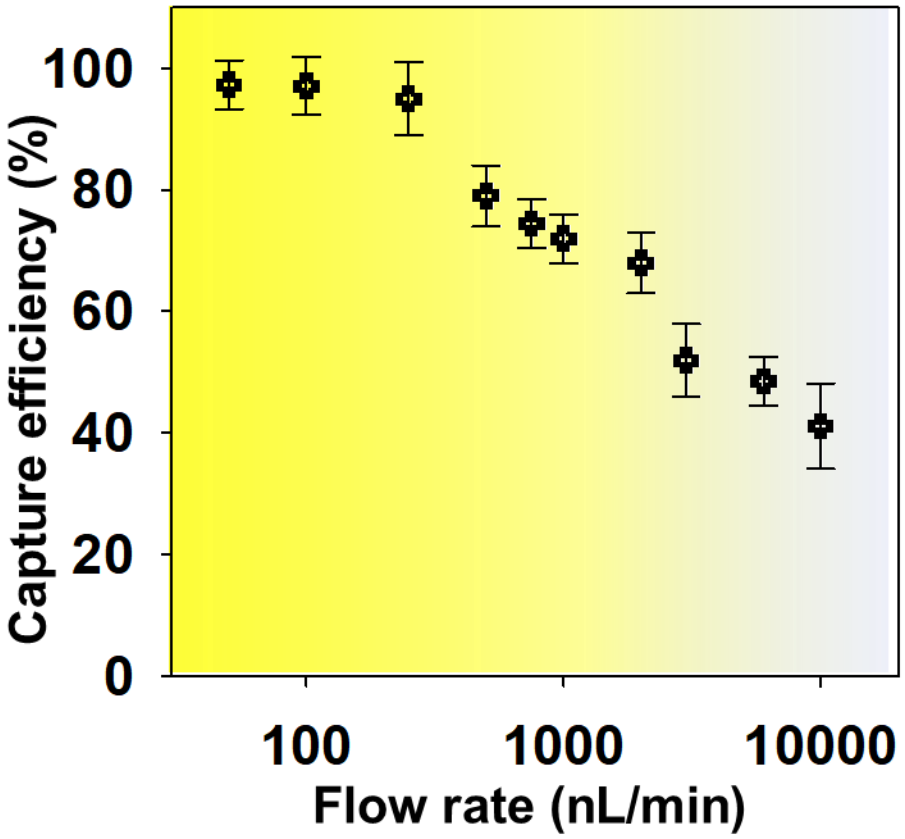

Figure 2-4. Exosome capture efficiency as a function of the mixing flow rate measured using purified, fluorescently labeled exosomes and capture beads. RSD is ~5% from replicate measurements.

2.3.3 Specificity for Isolating Tumor-derived Exosomes

Recent studies have suggested that both tumor cells and normal cells secrete exosomes, although significantly higher amounts of exosomes have been observed from tumor cells.[152] Therefore, specific isolation, purification, and characterization of tumor cell derived exosomes are essential.[153] We characterized the specificity for on-chip immunomagnetic isolation of exosomes from ovarian cancer patient blood plasma. On-chip isolation of variable exosome subpopulations was conducted by targeting both ovarian tumor-associated markers (EpCAM and CA-125) and common exosomal markers (CD9, CD81, and CD63). EpCAM is a cargo protein in exosomes and is highly overexpressed in multiple types of carcinomas, including ovarian tumors. CA-125 antigen is the most commonly measured biomarker for epithelial ovarian tumors, which accounts for 85–90% of ovarian cancer.

The exosome-bound beads were washed on the chip and then released and concentrated for morphology evaluation and counting of intact exosomes using TEM, as presented in Figure 2-5A. Significantly higher amounts of round membrane vesicles (smaller than 150 nm) were observed for EpCAM+, CA-125+, and CD9+ subpopulations from ovarian cancer plasma, compared to healthy controls. Negative control beads with IgG conjugation showed no capture of vesicles, demonstrating a good specificity of immunomagnetic isolation. The relative expression levels of the five surface markers were measured by counting the number of intact exosomes bound to the beads (n = 25). The results showed a ~3–5 fold increase in expression levels of the five markers from the ovarian cancer patient, compared to the healthy control (Figure 2-5B, p = 0.001).

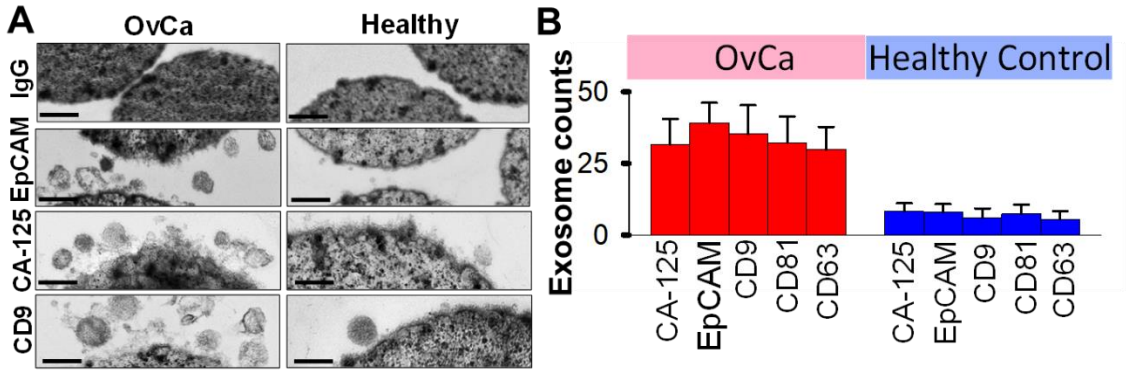

Figure 2-5. Microfluidic ExoSearch chip for specific isolation of ovarian cancer plasma derived exosomes. (**A**) TEM images of on-chip immunomagnetically isolated exosomes from ovarian cancer plasma, compared to healthy control. Scale bar is 100 nm. IgG-conjugated immunomagnetic beads were negative control beads. (**B**) Exosome counts analyzed from surfaces of variable capture beads (EpCAM+, CA-125+, CD9+, CD81+, CD63+) using TEM particle analysis (n = 25, CV = 2.8–10%). Single bead diameter was 2.8 μm and sliced bead layer was 80 nm thick.

To verify the results of on-chip isolation, we conducted nanoparticle tracking analysis (NTA) of ultracentrifugation-isolated exosomes to measure their size distributions and concentrations. As shown in Figure 2-6, on-chip isolated exosomes (CD9+) exhibited a notably narrower range with the log-normal fitted size distribution (R^2 > 0.98). The size smaller than 150 nm is a commonly used criterion to differentiate exosomes from larger microvesicles.[115] Compared to ultracentrifugation approaches, microfluidic immunoaffinity isolation yields a higher percentage of vesicles smaller than 150 nm (~79.7% *vs.* 60.7%), suggesting that the developed ExoSearch chip offers high specificity in the isolation of circulating exosomes.

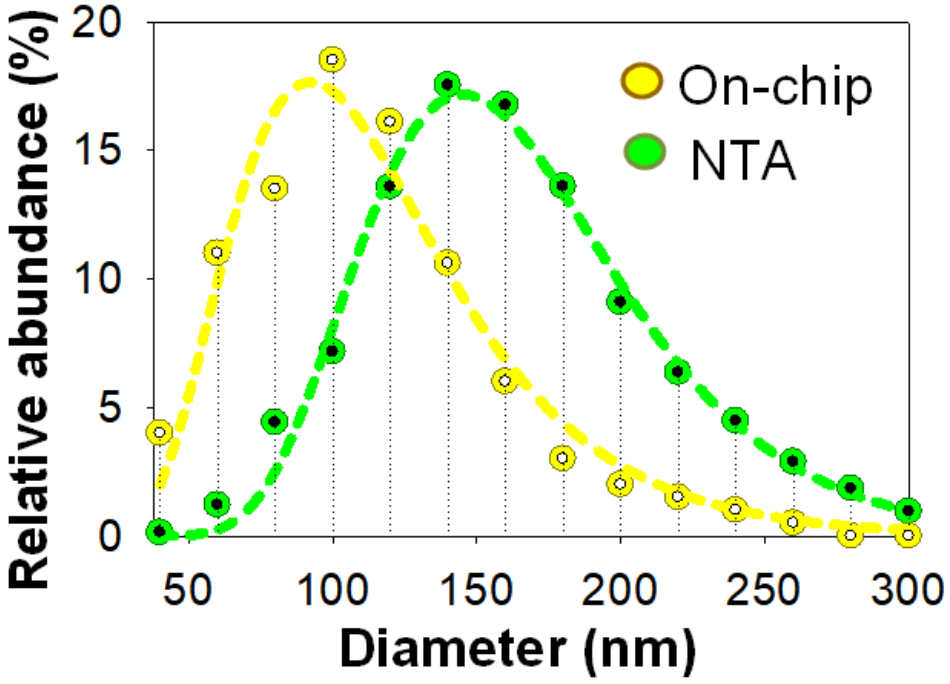

Figure 2-6. Size distribution of on-chip isolated exosomes (CD9+) using TEM particle analysis, compared to standard NTA analysis of ultracentrifugation-purified exosomes. Dashed lines were log-normal fit ($R^2 > 0.98$).

2.4 Conclusions

We demonstrated the feasibility of ExoSearch chip for rapid isolation of exosomes. To date, as a difficult surgery, conventional tissue biopsy for pathological diagnosis of ovarian cancer is extremely invasive. General imaging screenings, including tomography (CT) scans and magnetic resonance imaging (MRI) scans, are costly and unavailable in a majority of clinics. Therefore, blood-based assay for pre-screening is highly valuable and can dramatically decrease healthcare costs. This work, as a proof-of-concept, is an essential step and could serve as a basic platform for developing clinical tests, as well as fundamental laboratory research.

Chapter 3 Clinical Applications of Microfluidic ExoSearch Chip for Multiplexed Exosome Detection towards Blood-based Ovarian Cancer Diagnosis[*]

3.1 Introduction

Previously we developed a simple and robust microfluidic continuous-flow platform (ExoSearch chip) for rapid exosome isolation.[99] Here, we further combined on-chip continuous-flow mixing and immunomagnetic isolation streamlined with *in situ*, multiplexed detection of exosomes. We previously developed a microfluidic system for integrated exosome lysis and detection of intravesicular protein markers that exosomes carry.[135] However, on-chip isolation and enrichment of exosomes streamlined with multiplexed detection of marker combinations have not been established yet. In addition, the previous approach involves off-chip exosome capture using a small amount of magnetic beads and thus lacks the ability to prepare large-scale enriched exosomes for variable downstream molecular characterizations. The ExoSearch chip exceeds other existing microfluidic methods in several aspects, especially expediting multiplexed quantification of marker combinations in one sample significantly (~40 min). The one-step exosome assay enabled by the ExoSearch chip has been applied for ovarian cancer diagnosis *via* quantifying a panel of tumor markers from exosomes in a small volume of blood plasma (20 μL), which showed significant diagnostic accuracy and was comparable with the standard Bradford assay.

[*] Published on *Lab Chip* **2016**, *16*, 489-496.

3.2 Experimental

3.2.1 ExoSearch Chip Fabrication and Operation

The fabrication and preparation of the ExoSearch chip and magnetic beads is explained in Chapter 2. Afterwards, a mixture of three probing antibodies (anti CA-125/A488, anti EpCAM/A550, anti CD24/A633) labeled with distinct fluorescent dyes was introduced for 10 min incubation at a slow flow rate of 100 nL min^{-1}, followed by 5 min washing. The non-specific adsorption, specificity of probing antibodies, and incubation were well characterized.

For comparison with standard benchtop approaches, differential centrifugations were carried out on the collected fresh frozen blood plasma (2 mL) to obtain exosomes. The amount of protein recovered from pellets was measured by the Bradford assay (BioRad). The exosome vesicles were conserved at −80 °C until use. Nanoparticle tracking analysis (NTA) was performed as described in Chapter 2.

3.2.2 Reagents, Antibodies and Human Blood Plasma Samples.

The detection antibodies used in this study are CA-125 (B2626M, Meridian Life Science) conjugated with Alexfluor-488, EpCAM (323/A3, Thermo Scientific Pierce) conjugated with Alexfluor-550, CD24 (eBioSN3, eBioscience) conjugated with Alexfluor-633, HE4 (EPR4743, abcam) conjugated with Cyanine 5. The capture antibodies used in this study are CD9 biotin (C3-3A2, Ancell), CD81 biotin (1.3.3.22, Ancell), and CD63 biotin (H5C6, BioLegend). Exosome capture beads (Dynabeads M-270 Streptavidin, 2.8 μm in diameter) were prepared as describe in Chapter 2. Antibody-coated beads (0.1 mg mL^{-1}) were mixed with human blood plasma in the microfluidic

device by programmable syringe pumps. The human blood plasma was obtained from University of Kansas Cancer Center's Biospecimen Repository following consents and standard protocols.

3.2.3 Western Blotting

Tris-glycine pH 8.3, 4–12% precast polyacrylamide slab mini-gels with Blot Module (BioRad) was used for performing western blotting following the standard protocol. Ultracentrifugation-purified exosomes were lysed and prepared by adding protease inhibitors and running buffer (0.1% SDS), and heating at 65 °C for 5 min. After electrophoresis at 125 V for 2 h, gels were electro transferred to cellulose membranes (0.2 μm) at 25 V for 2.5 h in an ice bucket. After washing twice(1× PBS, 0.5% Tween-20, pH 7.4), the membranes were blocked with 5% dry milk overnight at 4 °C with shaking. The solution of primary biotinylated antibody (1:1500) was added into blocking buffer for 2 h incubation with shaking at room temperature. After incubation, the membrane was washed 3 times for 10 min each. The secondary antibody streptavidin-HRP (Invitrogen, ELISA grade, 1.2 mg mL^{-1}) diluted 1:2500 in the blocking solution was added for 1 h incubation at room temperature with agitation. After that, the washing step was repeated three times. The membrane was subsequently developed with chromogenic substrate reagent (BioRad) until the desired band intensity was achieved. Imaging was performed by using ChemiDoc imager (BioRad).

Table 3-1. Human Blood Plasma Samples Used in this Study

	No.	Age	Cancer Stage	Treatment
OvCa Patients	1	72	III	N
	2	67	II	N
	3	70	III	N
	4	80	III	N
	5	65	III	N
	6	61	III	N
	7	76	III	N
	8	74	II	N
	9	64	III	N
	10	78	III	N
	11	66	III	N
	12	75	II	N
	13	67	III	N
	14	55	III	N
	15	53	III	N
Healthy	1	51	N/A	N/A
	2	53		
	3	50		
	4	52		
	5	53		

De-identified samples and matching information were obtained from University of Kansas Cancer Center's Biospecimen Repository following consents and standard protocols.

3.2.4 Data Collection and Analysis

Fluorescence images were collected by an inverted epifluorescence microscope with a 20× (N.A. = 0.35) Zeiss objective lens and a scientific CMOS camera (OptiMOS, QImaging). The camera exposure time was set to 2000 ms with a 10 MHz frequency controlled by the open source software Micro-Manager 1.4. The filter sets of FITC, Rhodamine and Cy-5 were used for multiplexed three-color fluorescence detection with a LED light source for excitation. Fluorescence image analysis was performed using ImageJ (NIH, https://imagej.nih.gov/ij/) with an in-house written Macro to determine 1000 points randomly across consistent regions of bead aggregates for obtaining

averaged fluorescence intensity. Two fluorescence images were collected right before and after antibody detection in three fluorescence channels, respectively, for calculating the difference of fluorescence signals. The measured fluorescence signal was then normalized to the background.

3.3 Results and Discussion

3.3.1 Working Principle of the ExoSearch Chip

The assay workflow is described almost the same as in Chapter 2, except for the addition of the detection antibody mixture for multiplexed detection. As shown in Figure 3-1A, a plasma sample and immunomagnetic beads were introduced at the same flow rate from the injection channels (Figure 3-1B) through the long serpentine channel (Figure 3-1C) where they are uniformly mixed to facilitate exosome binding with the beads. Then the beads were retained as a tight aggregate in the downstream microchamber by magnetic force (Figure 3-1D). A mixture of antibodies labeled with unique fluorescent dyes was injected into the chamber to stain the exosomes for multi-color fluorescence imaging. Total analysis is completed with as low as 20 μL plasma samples in ~40 min.

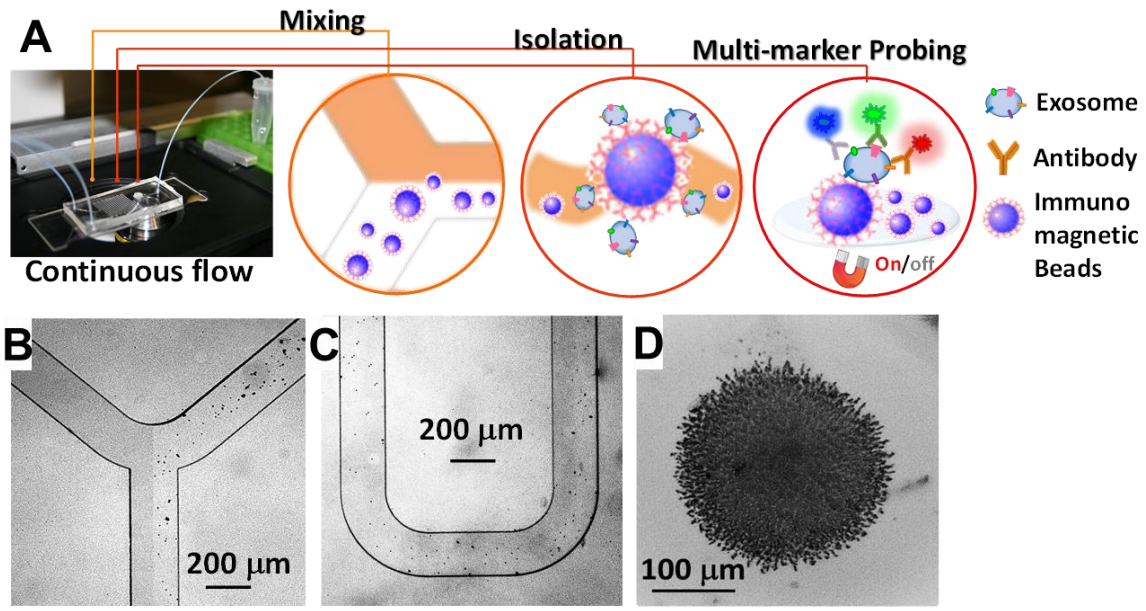

Figure 3-1. (**A**) Workflow of the ExoSearch chip for continuous mixing, isolation and *in situ*, multiplexed detection of circulating exosomes. (**B**)–(**C**) Bright-field microscope images of immunomagnetic beads manipulated in the microfluidic channel for mixing and isolation of plasma exosomes. (**D**) Exosome-bound immunomagnetic beads aggregated in the microchamber with a magnet and were stained by a mixture of three probing antibodies labeled with distinct fluorescent dyes for *in situ*, multiplexed detection of exosomes.

3.3.2 Quantitative and Multiplexed Exosomal Marker Detection

We first characterized the ExoSearch chip for quantitative isolation and detection of exosomes. Figure 3-2A shows the fluorescence images of exosomes isolated from serial dilutions of purified, fluorescently labeled plasma exosomes. The concentrations of purified plasma exosomes were determined by NTA measurements. Employing the same mixing and isolating conditions, increased fluorescence signals (ΔFL) were observed and found to be proportional to exosome concentrations. Using fluorescently labeled anti-EpCAM as the detection antibody, exosome titration curves were obtained for a healthy plasma sample and ovarian cancer plasma, which exhibited good linear response as seen in Figure 3-2B (R^2 > 0.98, CV = ~5%). The small variation of measurements indicates the

good robustness of the method. Moreover, a much higher ΔFL signal (~30-fold increase) was observed for the ovarian cancer sample, compared to the healthy control under the same concentration. These results demonstrated the ability of the ExoSearch chip to quantitatively measure exosome surface markers for differentiating changes associated with disease. The results were consistent with other recent reports that EpCAM is highly overexpressed in ovarian tumor exosomes.[154] The quantitative detection of intact exosomes was achieved with a limit of detection of 7.5×10^5 particles per mL (LOD, S/N = 3), which is 1000-fold sensitive than western blotting.[141] While such sensitivity is comparable with that of the previously reported microfluidic method,[141] our method features simple fabrication, easy operation, and low cost.

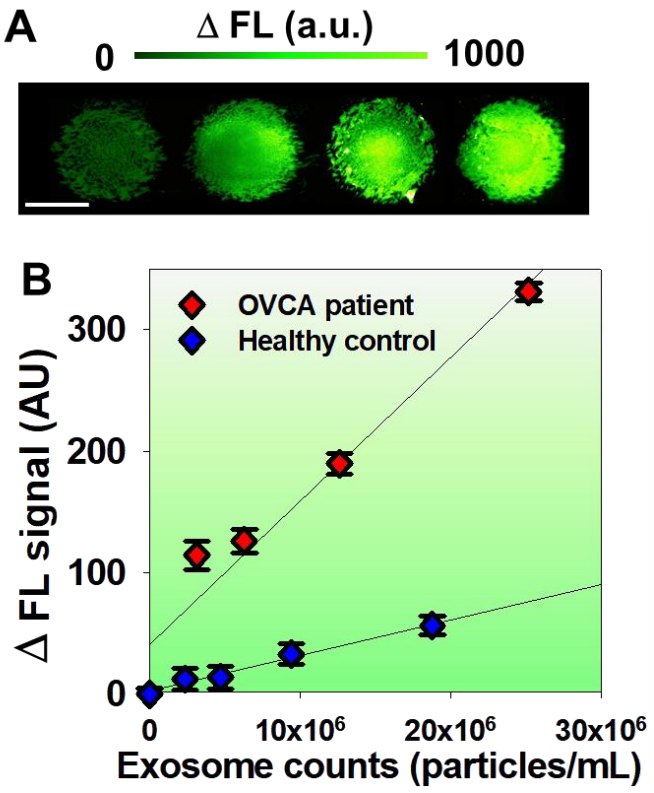

Figure 3-2. (**A**) CCD images of bead aggregates in the ExoSearch chip captured with fluorescence-labeled plasma exosomes in serial dilutions (from left to right: 5×10^5, $1 \times$

10^6, 5×10^6, 1×10^7 particles per mL). Scale bar was 100 μm. (**B**) Calibration curves for quantitative detection of intact exosomes ($R^2 > 0.98$, CV = ~5%). Exosomes were purified from one healthy control plasma and one ovarian cancer patient plasma using ultracentrifugation. Concentrations were measured by NTA.

In situ, multiplexed biomarker detection was then developed for rapid and quantitative microfluidic analysis of ovarian tumor derived plasma exosomes. We chose the common exosome marker CD9 as the capture antibody for selective isolation of exosomes because of the consistently high expression of CD9 we observed from human plasma derived exosomes (Figure 3-3).

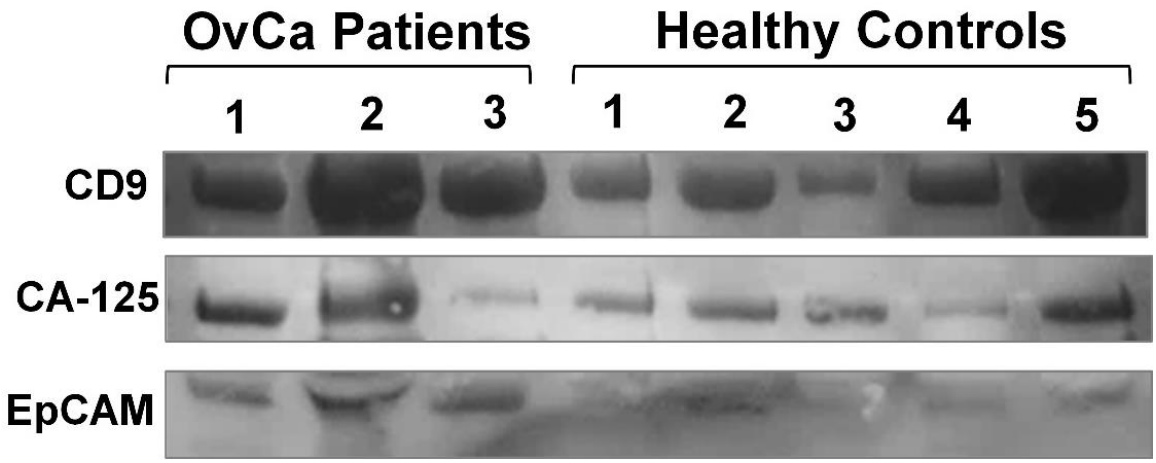

Figure 3-3. Western blotting analysis of expression levels of exosomal surface marker CD9, CA-125, and EpCAM. The plasma exosome samples were prepared from ovarian cancer patients and healthy controls using standard ultracentrifugation.

In addition to the established ovarian cancer biomarker CA-125, human epididymis protein 4 (HE4) has been recognized for improving the diagnostic specificity of CA-125 in pathological tests. We did not observe substantial expression of HE4 from the exosome samples (Figure 3-4), which could be due to the different secretion pathway

of HE4.[129] This observation was consistent with other recent reports.[141,155] Previous observations have indicated that CD24 could be a significant marker in ovarian tumor prognosis and diagnosis.[156] Therefore, we developed a multiplexed sandwich immunofluorescence assay to quantify isolated exosomes by targeting three markers, CA-125, EpCAM, and CD24 from the same population of exosomes, as exemplified in Figure 3-5A. Quantitative tests of raw human plasma collected from 20 subjects (n_{OvCa} = 15, $n_{healthy}$ = 5) were conducted for three-marker classification of ovarian tumor derived exosomes, and a distinctive three-marker expression pattern was observed for ovarian cancer patients (Figure 3-5B). The average expression levels of individual exosomal markers from ovarian cancer patients were statistically higher as compared to healthy controls (CD24: 3-fold increase, p = 0.003; EpCAM: 6.5-fold increase, p = 0.0009; CA-125: 12.4-fold increase, $p < 0.0001$).

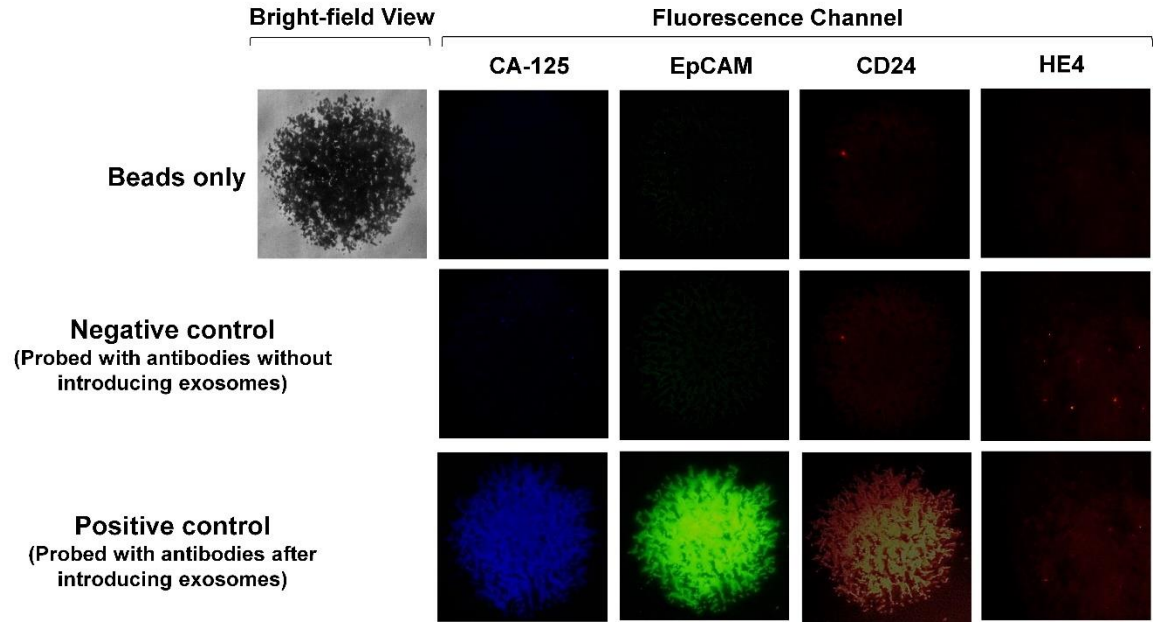

Figure 3-4. CCD captured microscopic images of bead aggregates under negative and positive control experimental conditions. Image size is 200 μm × 200 μm.

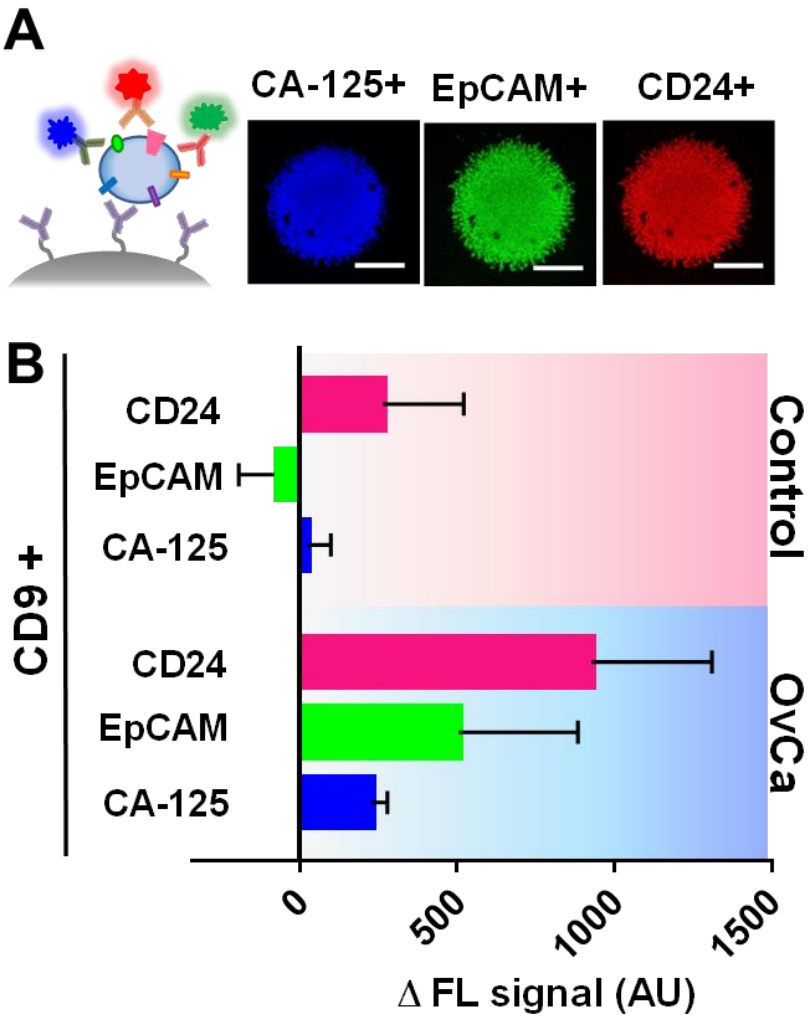

Figure 3-5. (**A**) CCD images of multiplexed three-color fluorescence detection of tumor markers (CA-125, EpCAM, CD24) from captured exosome subpopulation (CD9+). Scale bar was 50 μm, indicating the bead aggregate size. (**B**) Average expression levels of three ovarian tumor markers measured by the ExoSearch chip from 20 human subjects (n_{OvCa} = 15, $n_{healthy}$ = 5). Error bars indicate standard deviations.

In order to characterize the non-specific adsorption and cross-reactivity of antibodies, the negative and positive control experiments were designed and conducted in parallel for testing the four antibodies we used in this study (CA-125, EpCAM, CD24, and HE4). The fluorescence background of magnetic beads themselves was measured and compared with fluorescence intensity after detection antibody probing and washing,

without introducing plasma exosome samples. The slight auto-fluorescence of capture beads and negligible non-specific adsorption fluorescence were observed. There is no cross-reaction between antibodies we used in this study. The positive control (ovarian cancer patient plasma exosomes) showed strong fluorescence signals after probing with antibodies for CA-125, EpCAM, and CD24. However, we did not observe acceptable positive response from HE4 antibody probing, as HE4 was not expressed on the exosome surface which demonstrates the negligible non-specific adsorption onto captured exosomes (Figure 3-4).

In addition, Figure 3-5B shows low signal intensities for these three markers when their expression levels are low in healthy exosomes. This result also indicates negligible non-specific interference from non-specific antibody adsorption or cross-reactivity. In order to achieve an accurate fluorescence readout, we set the same image threshold (0–255 grey scale). Meanwhile, for each sample analysis, we collected one image of the PDMS microchamber as the background, one image of bead aggregates right before the antibody probing step, and one image of bead aggregates after the antibody probing and washing step. The difference of fluorescence signals before and after antibody probing was calculated, and then normalized to background. We designed a macro function of ImageJ for randomly picking up 1000 points in the consistent area of sample signals and measuring the average of mean gray value of fluorescence intensity.

3.3.3 ExoSearch Chip for Blood-based Ovarian Cancer Diagnosis

Currently, there is no single marker that can detect early-stage ovarian cancer with desired sensitivity and specificity (> 98%).[157] A large number of combinations of

biomarkers have been investigated to improve diagnostic sensitivity and specificity.[158] Circulating exosomes, enriched with a group of tumor antigens, provide a unique opportunity for cancer diagnosis using multi-marker combination. To this end, we employed the ExoSearch chip for blood-based diagnosis of ovarian cancer by simultaneously detecting three tumor antigens present in the same exosome subpopulation. Standard Bradford assay of total protein levels in ultracentrifugation-purified exosomes from matched human subjects was performed for parallel comparison.

Estimating the required sample size to adequately train developed diagnostic assay is of great practical importance.[159] We calculated the required sample size for evaluating diagnostic accuracy by comparing the area under a receiver operator characteristic (ROC) curve with a null hypothesis value of 0.5. ROC curve is a plot of false positive rate (1 − specificity) of a test on the x-axis against its true positive rate (sensitivity) on the y-axis for all possible cut-off points. The sample size takes into account the required significance level of 0.05 and 80% power of the test. The statistical power 0.8 and sample ratio of 3 were chosen for statistical judgment with 0.2 probability of type I error (false positive) and 0.2 probability of type II error (false negative). Thus, the sample size computational table was listed below in Table 3-2. The sample size of total 20 (15 ovarian cancer patients and 5 healthy controls) is adequate to evaluate diagnostic accuracy with acceptable diagnostic power.

Table 3-2. Sample Size Justification with Desired Errors

		Type I error	
		0.20	0.05
Type II error	0.20	**15 + 5**	27 + 9
	0.05	27 + 9	42 + 14

Both ExoSearch and Bradford assay showed significantly increased level of exosome proteins from ovarian cancer patients, compared to healthy controls (Figure 3-6, Bradford assay $p = 0.001$; ExoSearch chip $p < 0.001$). Particularly, the ExoSearch chip gave individual exosomal protein expression levels and the levels of CA- 125 and EpCAM showed extremely significant differences between ovarian cancer patients and healthy controls (EpCAM, $p = 0.0009$; CA-125, $p < 10^{-4}$).

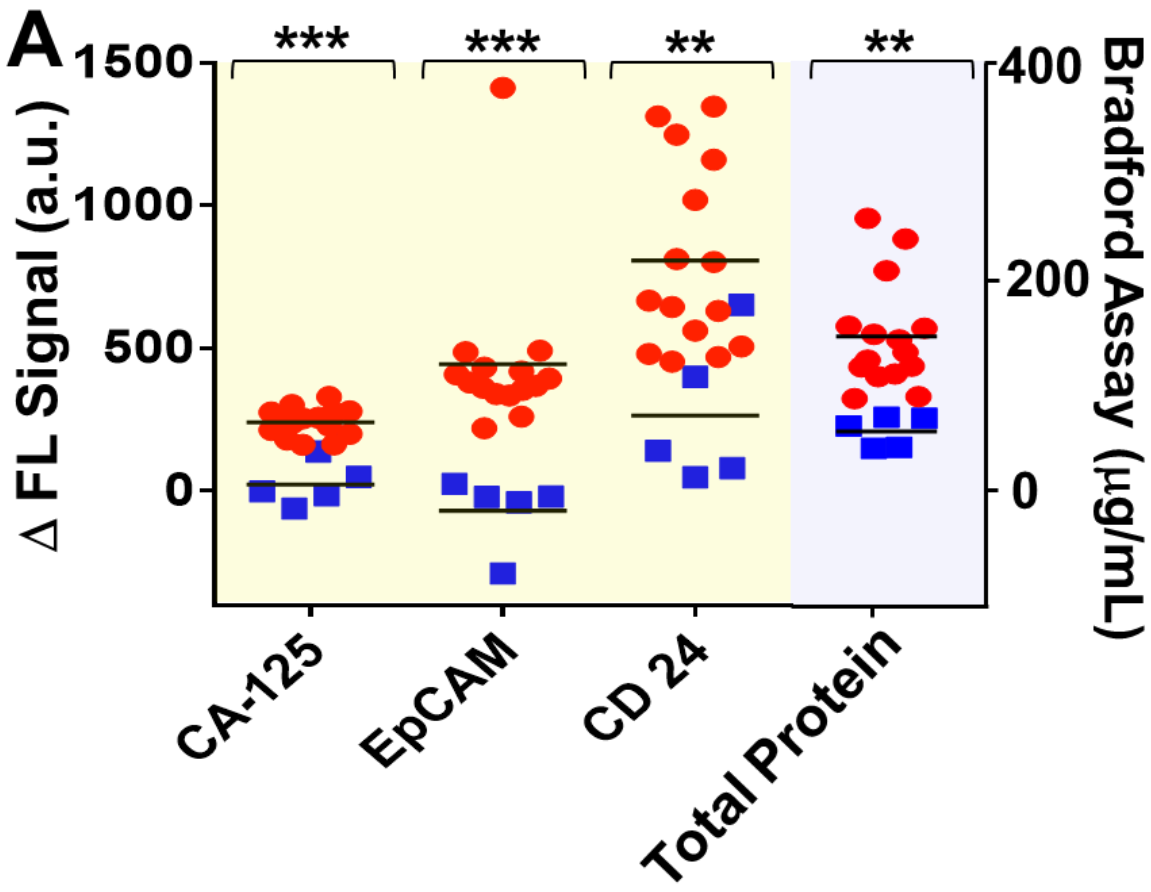

Figure 3-6. Scattering plots of expression levels of three tumor markers (CA-125, $p < 10^{-4}$; EpCAM, $p = 0.0009$; CD24, $p = 0.003$) from blood plasma derived exosomes ($n_{OvCa} = 15$, $n_{healthy} = 5$), compared to the standard Bradford assay of total proteins ($p = 0.0013$) in ultracentrifugation-purified exosomes from matched human subjects. Black lines indicate the average expression levels of each group. Ovarian cancer patients were represented by red dots, and healthy controls were represented by blue dots.

Sensitivity and specificity are terms used to evaluate a clinical test. The area under the ROC curve (a.u.c.) represents the overall accuracy of a test, with a value approaching 1.0 indicating a high sensitivity and specificity. The a.u.c. is a global measure of diagnostic accuracy.[160,161] By comparison of areas under ROC curves, we can estimate which one of the tests is more suitable for distinguishing health from disease. The accuracy classification for a diagnostic test is listed in Table 3-3.

Table 3-3. Accuracy Classification by a.u.c. for a Diagnostic Test.

a.u.c Range	**Classification**
0.9 < a.u.c. < 1.0	Excellent
0.8 < a.u.c. < 0.9	Good
0.7 < a.u.c. < 0.8	Fair
0.6 < a.u.c. < 0.7	Poor

To determine the diagnostic accuracy of the ExoSearch chip assay, we analyzed the true positive rate (sensitivity) and false positive rate (1 − specificity) using ROC curves. The areas under the curves obtained for CA-125, EpCAM, and CD24 were 1.0, 1.0 and 0.91, respectively, which were comparable with the standard Bradford assay (a.u.c. = 1.0, 95% CI) (Figure 3-7). However, the diagnostic accuracy of using exosomal particle concentrations measured by NTA was relatively poor with an a.u.c. of only 0.67 (Figure 3-7B and Figure 3-8, 95% CI). It could be attributed to the variation of NTA measurement which gives a relatively large uncertainty in size and concentration.[158,162]

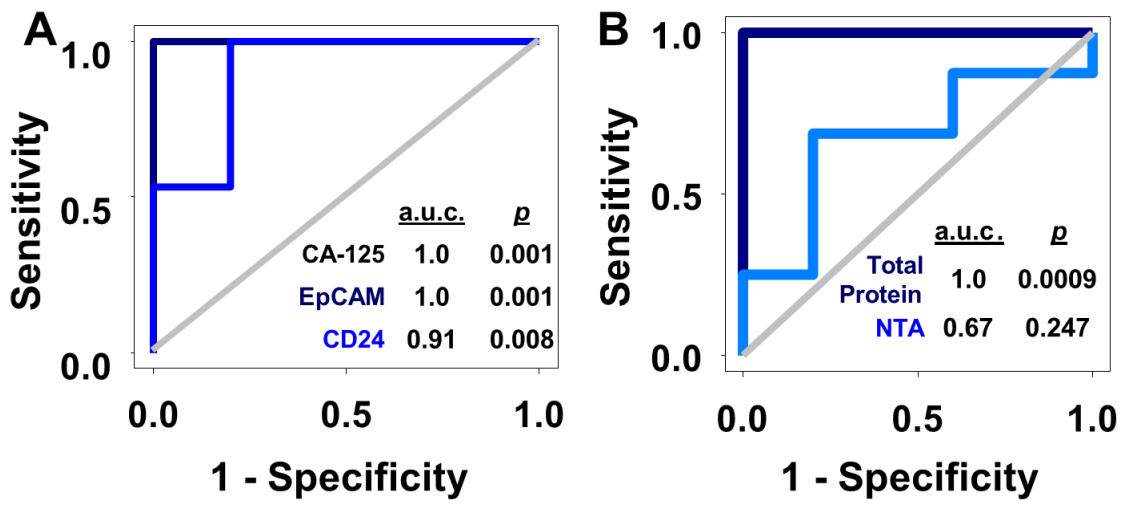

Figure 3-7. (**A**) ROC analysis of the ExoSearch chip assay for *in situ*, multiplexed detection of three ovarian tumor exosomal markers (CA-125 a.u.c. = 1.0, $p = 0.001$; EpCAM a.u.c. = 1.0, $p = 0.001$; CD24 a.u.c. = 0.91, $p = 0.008$). Confidence interval (CI) is 95%. (**B**) ROC analysis of standard benchtop measurements (Bradford assay of total exosome protein, and NTA of exosome concentration) of blood plasma exosomes from matched patients in Figure 3-7A.

In addition, the results were consistent with recent reports showing that counting exosomes alone was insufficient for cancer diagnosis and targeting specific exosome phenotypes could markedly improve the diagnostic accuracy.[48] By ROC analysis (Table 3-4), the ExoSearch chip assay was highly accurate in discriminating plasma exosomes from ovarian cancer patients *vs.* healthy individuals. The above results suggested that the ExoSearch chip enables sensitive multiplexed exosomal marker detection for blood-based diagnosis of ovarian cancer with significant predictive power. The combination of plasma exosomal markers CA-125, EpCAM, and CD24 provided desirable diagnostic accuracy for non-invasive, early detection of ovarian cancer (Table 3-4).

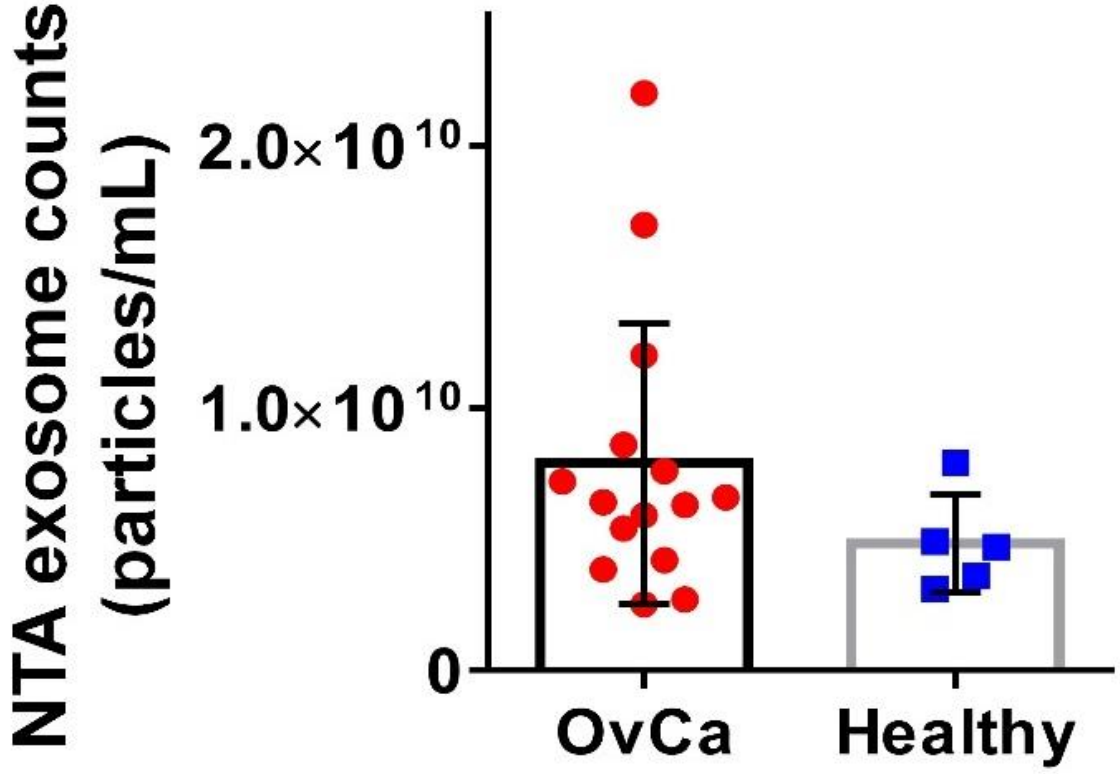

Figure 3-8. The plasma exosome particle concentrations from 20 human subjects measured by NTA (n_{OvCa} = 15, $n_{healthy}$ = 5). Slightly higher average amount of plasma exosomes (1.5-fold) was observed from ovarian cancer patients, compared to healthy controls (p = 0.25). The difference was not significant.

Table 3-4. Diagnostic Accuracy Analysis by Receiver Operating Characteristic Curve

Test Variables	**ExoSearch Chip**			**Bradford Assay**	**NTA**
	CA-125	EpCAM	CD24	Total Exosomal Protein	Particle Concentration
ROC Curve Area	1.000	1.000	0.9067	1.000	0.6750
Standard Error	0.000	0.000	0.0903	0.000	0.1322
95% CI	1.000 to 1.000	1.000 to 1.000	0.729 to 1.084	1.000 to 1.000	0.413 to 0.936
P Value	0.0010	0.0010	0.0078	0.0009	0.2477

3.4 Conclusions

Because exosomes differ 5-fold in size and 10^4-fold in concentration in biological samples, and can contain other membrane derived subcellular structures,[38] accurate measurement of exosome concentration in biofluids is challenging. For conventional approaches, such as NTA and flow cytometry, exosome quantitation is limited primarily by minimum detectable vesicle sizes, resulting in relatively large variation (CV = ~20%).[162,163] The ExoSearch chip enables simultaneous, quantitative evaluation of multiple markers from the same exosome subpopulation with much improved measurement reproducibility (CV < 10%), indicating the good robustness of this method. Such robustness is essential for precision medicine and diagnostics involving exosomes. In addition, the continuous-flow design affords capability for obtaining distinct populations of exosomes from a wide range of preparation volumes (10 μL to 10 mL), which is useful for downstream comparative molecular profiling or therapeutic use.

As surrogates of tumor cells, exosomes hold great promise for precise and personalized cancer diagnosis. Combinations of exosomal protein markers may constitute a "cancer signature" and provide improved detection as the first step in multimodal screening.[163] Nevertheless, to the best of our knowledge, multiplexed assay of exosomes is not yet well established. We demonstrated the feasibility of ExoSearch chip for non-invasive diagnosis of ovarian cancer using a combination of three exosomal tumor markers (CA-125, EpCAM, CD24), which showed comparable accuracy and diagnostic power (a.u.c. = 1.0, $p = 0.001$) with the standard Bradford assay (a.u.c. = 1.0, $p = 0.0009$). However, the ExoSearch chip requires only 20 μL of human plasma for

multiplexed detection of the three tumor proteins within 40 min, as compared to ~1 mL of plasma and ~12 h required by the Bradford assay.

To date, conventional tissue biopsy for pathological diagnosis of ovarian cancer is extremely invasive as a difficult surgery. General imaging screenings, including tomography (CT) scans and magnetic resonance imaging (MRI) scans, are costly and unavailable in a majority of clinics. Therefore, blood-based assay for pre-screening is highly valuable and can dramatically decrease healthcare costs. The ExoSearch chip provides a cost-effective, accessible approach for specific, rapid isolation of blood diagnostic exosomes, paving the way for clinical utilization of exosomes. We will further validate the diagnostic effectiveness of the ExoSearch chip in various sample cohorts and enhance the disease discrimination power, including the use of large-scale sample size and benign tumor group as a positive control. This microfluidic platform could be used for developing clinical tests in other diseases, as well as fundamental laboratory research.

Chapter 4 Microfluidic Communicating Vessel Chip for Expedited and Automated Immunomagnetic Assays*

4.1 Introduction

Immunoassay based on specific antibody-antigen interactions has been one of the most versatile and widely used bioassays in chemistry, life sciences, and medicine.[164] An immunoassay enables sensitive and specific measurements of a broad spectrum of targets, ranging from small molecule compounds (*e.g.*, drugs and toxins)[165] to macromolecules like peptides and proteins, to bioparticles such as extracellular vesicles and virus,[99,166,167] and to bacterial and mammalian cells.[168,169] Microfluidics is well poised to develop new-generation immunological technologies because of its unique advantages in combining precise flow control, promoted biochemical reactions in small volumes, circuit-level integration, and system automation.[170,171] Numerous microfluidics-based immunoassays have been developed to improve analysis sensitivity, speed, and multiplicity;[171,172] and the technologies are continuously evolving, driven by the pressing needs for better analytical tools for emerging applications ranging from single-cell analysis[173-176] to point-of-care diagnosis[177,178] and to precision medicine.[179,180]

A typical protocol of a conventional immunoassay, such as enzyme-linked immunosorbent assay (ELISA), encompasses a series of washing, mixing, and incubation steps, which are labor intensive as well as time consuming (several hours or even up to 2 days), and consume large volumes of reagents. Standard immunoassay protocols can be substantially simplified and expedited by leveraging microfluidic technology to

* Published on *Lab Chip* **2018**, *18*, 3830-3839.

accelerate and minimize the processing steps. For instance, hydrodynamic flow washing in microchannels obviates the need for repetitive washing steps with large volumes of buffers required by microplate ELISA to effectively reduce non-specific background.[181] Moreover, several wash-free immunoassays have been developed with different microfluidic techniques, including a microfluidic droplet splitting system coupled with surface-enhanced Raman scattering (SERS) detection,[182] an integrated microfluidic homogeneous AlphaLISA chip,[183] and a microfluidic giant magnetoresistive (GMR) biosensor platform.[184] Eliminating excessive washing in the immunoassay protocol affords significant advantages in improving the analytical performance as it 1) simplifies and expedites the assay by removing multiple time-consuming steps; 2) avoids potential variation in analysis, and 3) enhances detection sensitivity by minimizing dissociation of analytes, especially weakly bound protein complexes. Despite these benefits, the aforementioned wash-free microfluidic methods require sophisticated chip design, fabrication, and operation expertise, which limit their broad applications.

Magnetic separation of analyte binding beads is a versatile method for sample preparation and bioassays because of its simplicity and ease of automation.[185] Combining magnetic bead manipulation and unique microscale surface effects, a multi-phase microfluidic strategy has been recently developed to largely simplify and expedite the workflow of bioassays. In this strategy, the aqueous assay reagents are dispensed into an array of stationary droplets,[186-190] open reservoirs,[191-194] or microchambers[195] isolated by an immiscible phase, *e.g.*, oil or air, and external magnetic field is used to pull the affinity magnetic beads across these compartments sequentially to complete the sample preparation and/or detection workflow. This stationary multi-phase strategy exploits the

surface tension-caused volume pinning effect to separate analyte-bound beads from the bulk media with small-volume carryover, which enables rapid and automated bioassays without tedious washing. Despite their advantages, the stationary multi-phase microfluidics requires tight control of the properties of interfaces between the phases and demands a large amount of beads to generate sufficient magnetic forces to overcome surface tension. Bead loss may occur during such surface tension-gated traverse. Moreover, small carryover of unbound materials by unwashed bead clusters can result in non-specific signals that can limit the analytical sensitivity or cause false positives in clinical applications, especially for extremely sensitive amplification-based assays.

Distinct from the previous microfluidic immunoassays implemented with either flow-based or stationary multi-phase microsystems, herein we report a single-phase, pneumatically gated microfluidic communicating vessel chip (μCOVE) for simplified and expedited immunoassays (Figure 4-1). First, while our device adapts the similar format of reagent loading and immunomagnetic assay workflow for the stationary multi-phase microsystems, an array of pneumatically actuated gates instead of an immiscible phase is used for the compartmentalization of aqueous reagents. Thus, our single-phase platform takes advantage of stationary microfluidics to simplify and streamline the assay workflow, while avoiding the aforementioned limitations associated with the multi-phase operation. Furthermore, in contrast to the stationary assay systems, μCOVE employs a hydrostatic pressure-driven flow, the simplest approach for fluid control in a microfluidic system, to afford rapid yet effective washing of immunomagnetic beads. Overall, our device based on the communicating vessel principle presents a novel immunoassay platform that combines the advantages of the stationary multi-phase microfluidics in

simplicity and streamlined operation and the benefits of effective washing provided by the flow-based microfluidics. As of a proof-of-concept, we validated our platform by detecting two protein biomarkers commonly targeted for cancer diagnosis, the carcinoembryonic antigen (CEA) and epidermal growth factor receptor (EGFR). Our results demonstrated highly sensitive detection of these biomarkers down to the level of sub-picogram per mL. Direct measurement of the biomarker expression in the crude A431 cell lysate using different washing methods further verified the ability of the μCOVE device for rapid immunoassay without excessive washing steps. Owing to its simplicity and high performance, our system would provide a useful platform for clinical analysis of protein biomarkers to facilitate disease diagnosis and other applications such as point-of-care (POC) testing.

4.2 Materials and Methods

4.2.1 Chip Fabrication

Two-layer poly(dimethylsiloxane) (PDMS) microchips (Figure 4-1A) were fabricated using standard multilayer soft lithography. In brief, silicon wafers were cleaned with piranha solution (75% sulfuric acid and 25% hydrogen peroxide) and coated with an SU-8 photoresist (MicroChem) by spin-coating. The SU-8 microstructures were fabricated onto the wafers from the photomasks designed with AutoCAD, following the protocols recommended by the manufacturer for fabricating a 50 μm thick bottom flow layer (SU-8 2025) and a 100 μm thick top pneumatic layer (SU-8 100), respectively. The SU-8 molds were treated with trichloro(1*H*,1*H*,2*H*,2*H*-perfluorooctyl)silane (Sigma-Aldrich) by gas-phase silanization under vacuum for at least 4 h. To make the pneumatic

layer, PDMS base and a curing agent (Dow Corning) were mixed at a 10:1 ratio (35 g in total), poured onto the mold and cured in an oven at 70 °C for at least 2 h. The PDMS pieces were peeled off from the mold, cut, and punched to make pneumatic connection holes. A thin PDMS flow layer was made by spin coating the mold with 6 g of the prepolymer mixture (15:1) followed by curing at 70 °C for 30 min in an oven. The two layers were treated by UV/ozone briefly, manually aligned under a stereomicroscope, and permanently bonded by baking in a 70 °C oven. The two-layer PDMS slabs were then peeled off from the mold and reservoirs were punched. Lastly, an integrated microchip was fabricated by permanent bonding of the PDMS slab and glass slide using UV/ozone treatment (Figure 4-1B). The assembled chip was blocked by 5% bovine serum albumin (BSA, Fisher Scientific) overnight at 4 °C to reduce non-specific binding.

4.2.2 Magnetic Beads Preparation

100 μL of approximately 30 mg mL^{-1} carboxylic acid coated magnetic beads (Dynabeads M-270 Carboxylic Acid, Invitrogen) were transferred to a 1.5 mL microcentrifuge tube and washed twice with 100 μL of 25 mM 2-(*N*-morpholino)ethanesulfonic acid (MES, pH 5, Sigma-Aldrich) for 10 min. The beads were then activated with 50 μL of freshly prepared 50 mg mL^{-1} *N*-ethyl-*N*′-(3-dimethylaminopropyl)carbodiimide hydrochloride (EDC, Sigma-Aldrich) and 50 μL of 50 mg mL^{-1} *N*-hydroxysuccinimide (NHS, Sigma-Aldrich) with rotation at room temperature for 30 min. The activated beads were washed twice with 100 μL of 25 mM MES buffer (pH 5) and then mixed with 60 μg of the anti-CEA capture antibody (10-C10F, Fitzgerald) or the anti-EGFR capture antibody (DYC1854-2, R&D systems),

respectively. After overnight incubation with rotation at 4 °C, the beads were magnetically collected to remove the supernatant and blocked by 100 μL of 50 mM ethanolamine (Sigma-Aldrich) in phosphate-buffered saline (PBS, Corning Cellgro) for 60 min at room temperature with rotation. Finally, the capture antibody labeled magnetic beads were washed four times with 100 μL of washing buffer (0.1% BSA and 0.1% Tween-20 in PBS), resuspended in 200 μL PBS, and stored at 4 °C.

4.2.3 Microchip Immunomagnetic Assay

Protein standards and detection antibodies were prepared in PBS working solution (PBSW, pH 7.4) containing 1% bovine serum albumin (BSA) (Sigma-Aldrich). A series of protein standards was prepared by 10-fold dilution of the stock protein solution. 0.5 μg mL^{-1} streptavidin conjugated β-galactosidase (SβG, Life Technologies) and 0.2–0.5 mM resorufin β-D-galactopyranoside (RGP, Life Technologies) were prepared in PBSW with 2 mM $MgCl_2$ (Fluka Analytical) added. For CEA quantification, 3.2 pg mL^{-1} to 32 ng mL^{-1} CEA protein standards (30-1819, Fitzgerald), 43 μg mL^{-1} biotinylated anti-CEA detection antibody (61-C10GB, Fitzgerald) and 0.2 mM RGP were used in the microchip immunomagnetic assays. For EGFR quantification, 0.2 pg mL^{-1} to 2 ng mL^{-1} EGFR protein standards (DYC1854-2, R&D systems), 3.6 μg mL^{-1} biotinylated anti-EGFR detection antibody (DYC1854-2, R&D systems) and 0.5 mM RGP were used. For biological sample analysis, the non-denatured A431 whole cell lysate (L015V2, Abnova) was diluted by 1000 and 10000-fold in PBSW and used for the measurement of the EGFR expression level.

The on-chip assay was performed following the procedure illustrated in Figure 4-1C. The monolithic diaphragm gates were actuated at 90 kPa pressure and −87 kPa vacuum controlled by a homemade solenoid controller *via* a LabVIEW program. A 5% BSA blocked chip was washed with PBS and loaded with 10 μL assay reagents and 20 μL buffers in the individual vessels as specified as follows. A 20 μL protein sample was mixed with 1 μL of 15 mg mL^{-1} capture antibody labeled magnetic beads in the first reaction vessel and incubated for 2 h with rotation, during which the vessels were covered by PDMS slabs in order to minimize evaporation. After incubation, the magnetic beads were concentrated into the connecting channel by a magnet and the sample solution was removed by aspiration. With the pneumatic gate opened, the protein/bead complexes were magnetically drawn into the second vessel loaded with 20 μL of washing buffer within ~20 seconds. The second gate was then opened, and the bead complexes were magnetically pulled into the third vessel containing 10 μL of the biotinylated detection antibody and incubated for 1 h with the gates closed. Following the same operation, the immunocomplex-bound beads were pulled through the next buffer vessel for rapid washing and into the fifth vessel containing 10 μL of 0.5 μg mL^{-1} SβG for enzyme tagging. After 30 min incubation, the bead complexes were pulled through two buffer vessels into the detection microchamber and mixed with the RGP substrate loaded from the last vessel by diffusion. Fluorescence detection was performed after 30 min of enzymatic reaction. Fluorescence images were acquired using an inverted epifluorescence microscope equipped with a 10× objective and a scientific CCD camera (Carl Zeiss) and analyzed with ImageJ (NIH, https://imagej.nih.gov/ij/) to measure the fluorescence intensity.

4.3 Results and Discussion

4.3.1 Chip Design and Assay Principle

The μCOVE chip is designed to streamline and expedite the multi-step workflow of conventional magnetic bead-based immunoassays. Figure 4-1A and B display the prototype μCOVE chip that we have devised. To demonstrate the scalability of our design, the three-layer PDMS/glass chip integrates four parallel μCOVE units, each consisting of seven vessels of ~20 μL volume connected by the flow channels (~50 μm high) fabricated on the bottom PDMS membrane (~200 μm thick). The adjacent vessels are disconnected by the normally-closed gates that can be lifted by the pneumatic channels fabricated on the top PDMS layer. The vessel array is coupled with an enclosed detection microchamber at the end which is connected to a reservoir for loading the enzymatic substrate, RGP (Figure 4-1B). The immunoassay workflow based on the μCOVE chip is schematically illustrated in Figure 4-1C. Briefly, with all gates closed under pressure, the first vessel is loaded with the 20 μL sample mixed with antibody-coated magnetic beads and others are loaded with either 10 μL reaction reagents (*i.e.*, detection antibody, SβG, and RGP) or 20 μL washing buffers. After capturing the target proteins, the beads were pulled down by a magnet and 10 μL supernatant was removed from the sample vessel. The beads are pulled across a washing vessel with the two controlling gates opened one at a time. Similarly, the beads are then sequentially drawn across the downstream vessels containing the biotinylated detection antibody, washing buffer, and SβG to form the sandwiched immunocomplexes. Finally, the beads are pulled across two washing vessels into the detection chamber and mixed with the RGP substrate loaded from the last vessel by diffusion. The tagged enzyme converts RGP to fluorescent

resorufin molecules for quantitative measurement of the bead-captured proteins. Thus, the μCOVE chip combines magnetic bead manipulation and pneumatic microvalve actuation, both of which are amenable to microfluidic integration and automation to effectively streamline the workflows for sample preparation and bioassays.

A standard immunoassay protocol requires multiple washing steps that can be tedious. In addition to streamlining the workflow, a distinct feature of our design is that it exploits the hydrodynamic flow generated by the communicating vessels to expedite the washing steps and thus the entire assay. Rapid bead washing by the hydrodynamic flow in a μCOVE chip, herein referred as to hydrodynamic washing, is conceptually depicted in Figure 4-1D. It is well known that in communication vessels, the fluid flows to reach the same level in all of the vessels driven by the hydrostatic pressure $\Delta P = \rho g \Delta h$, where ρ is the density of the fluid, g is the gravitational acceleration, and Δh is the difference in elevation. We load the washing buffer vessels to a higher level than the reagent vessels, which creates a hydrostatic pressure between two adjacent vessels. Magnetic beads in a reagent vessel can be concentrated at the closed gate using a magnet. When the gate is lifted up, the beads will be pulled through the connecting channel and washed by a counter flow of washing buffer generated by the hydrostatic pressure between the connected vessels. As discussed in detail in the following sections, our results showed that hydrodynamic washing in our μCOVE chip is able to effectively suppress non-specific background without the need to re-disperse and wash the beads in the buffer vessels for an extended period, which largely reduces the overall analysis time (Table 4-1).

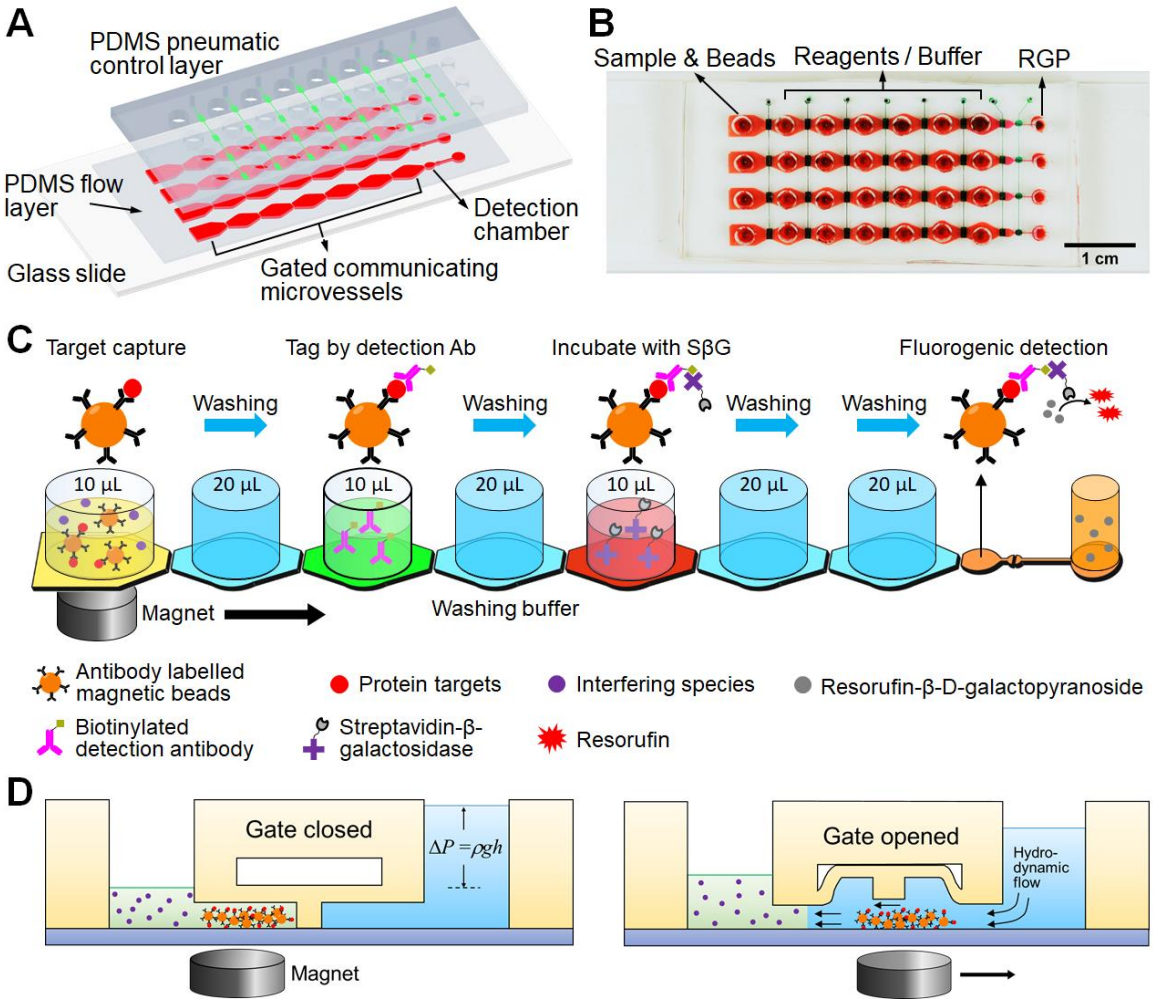

Figure 4-1. Microfluidic communicating vessel (µCOVE) chip for rapid magnetic bead-based ELISA. (**A**) Schematic illustration of the chip design. The three-layer PDMS/glass chip integrates four parallel units of gated communicating vessels, each consisting of seven vessels (~20 µL each) connected by the flow channels (red) in the bottom PDMS layer. The vessels are gated with an array of normally-closed microvalves actuated by the pneumatic channels (green) in the top layer. The vessel array ends with an enclosed detection microchamber connected to a reservoir for loading RGP. (**B**) Photograph of an assembled chip filled with red food dye in the communicating vessels and green dye in the pneumatic control channels. (**C**) Assay workflow. Immunomagnetic microbeads are added into the sample vessel for target capture. After incubation, the first two gates are pneumatically opened one at a time to pull the beads across the next washing buffer vessel with a magnet. The beads are sequentially moved through the vessels containing a biotinylated detection antibody, washing buffer, and streptavidin–β-galactosidase to form immunocomplexes. Finally, the beads are pulled across two washing vessels into the detection microchamber loaded with RGP from the end reservoir. The tagged enzyme converts RGP to fluorescent resorufin molecules for quantitative measurement of the bead-captured proteins. (**D**) Schematic illustration of rapid hydrodynamic washing in a µCOVE chip. The hydrostatic pressure caused by the different liquid levels between two

communicating vessels generates a counter flow to wash the beads during traverse. The washed beads are moved across the washing vessels without incubation to expedite the immunoassay. The drawing is not to scale.

4.3.2 μCOVE Operation

We first characterized the hydrodynamic flow induced by hydrostatic pressure for bead washing and pneumatically gated magnetic manipulation of beads as they are the key processes of the μCOVE operation. In our device, the vessels of ~20 μL volume were punched through ~5 mm thick PDMS chips with a 2.5 mm biopsy punch. A pair of gated communicating vessels was filled with 10 μL resorufin solution and 20 μL water, respectively, which are the typical liquid volumes used for the actual immunoassay. The normally-closed pneumatic gates were found to completely block the flow between two adjacent vessels, indicated by no observed transport of dye molecules across the gate (Figure 4-2A, images). As expected, when the gate was lifted up, the fluorescent solution was pushed away from the gate, indicating a stream flowing from the water vessel to the dye vessel. The fluorescence intensity measurement verified that this flow is effective to flush the dye solution away rapidly (Figure 4-2A, bar graph). This hydrostatic pressure-driven flow was further studied in a μCOVE chip filled with 20 μL aqueous suspension of fluorescent microparticles and 10 μL water. Using a high-speed sCMOS camera, we observed that the fluorescent microparticles traveled from the gate into the water vessel within ~120 ms after opening the gate (Figure 4-2B). The averaged velocity of the initial flow caused by the hydrostatic pressure was estimated to be 7.8 ± 1.7 mm s^{-1} by tracking the microparticles ($n > 50$) within a timeframe of ~120 ms. The flow rate declined over time, as the solution flowed from the particle vessel into the water vessel, diminishing the difference in the liquid levels in the two vessels. The solutions in the two communicating

vessels in our device were seen to approach approximately equal levels in one minute. Such a rapid hydrodynamic counter flow is essential to reduce the carryover and non-specific binding on the microbeads without extended incubation for bead washing.

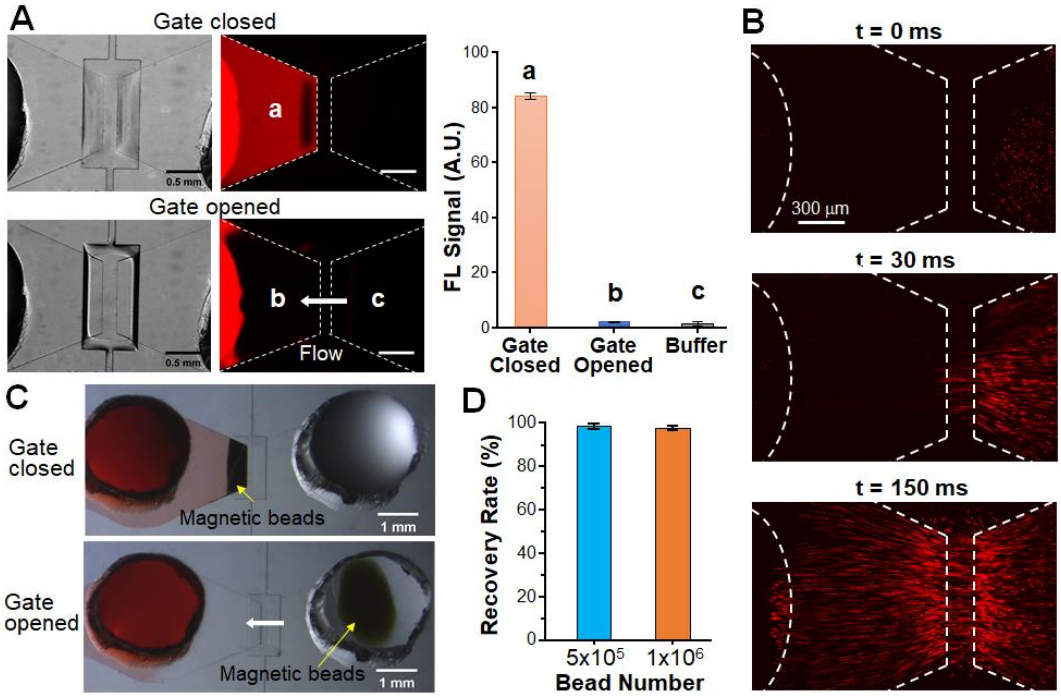

Figure 4-2. Characterization of μCOVE for rapid flow washing of magnetic beads. (**A**) Bright-field and fluorescence (left) microscopy images of the flow caused by the hydrostatic pressure in a μCOVE chip. The white lines indicate the microchannels and the gate that disconnects the left vessel filled with 10 μL of resorufin solution from the right vessel with 20 μL of water. When the gate was opened, the fluorescent solution was seen to be pushed away from the gate, indicating a stream flowing from the water vessel to the dye vessel. The fluorescence intensity at the indicated locations (a–c) was measured and plotted as the bar graph on the right. (**B**) Representative time-lapse images showing the flow of fluorescent microparticles (2 μm) after the gate was opened. The vessels were filled with 10 μL of water (left) and 20 μL of aqueous solution of microparticles (right), respectively. The averaged flow velocity was measured to be 7.8 ± 1.7 mm s^{-1} by tracking the trajectories of particles (n > 50). (**C**) Bright-field microscopy images showing magnetic beads being concentrated at the closed gate (top) and pulled through the opened gate (bottom) by a magnet against the water stream flowing into the dye solution vessel (white arrow). (**D**) Recovery rates of the magnetic beads pulled across all the vessels at different initial bead numbers.

We then demonstrated magnetic bead transfer under the hydrodynamic counter flow between a vessel loaded with 1×10^6 magnetic beads in 10 μL red food dye and the adjacent vessel filled with 20 μL water. As seen in Figure 4-2C, using a magnet, microbeads were concentrated at the closed gate and then pulled into the water vessel against the stream flowing into the dye-filled vessel after the valve was opened. No discernable loss of magnetic beads was observed after pulling through the gate under the counter flow and hydrodynamic washing effectively removed the dye solution. The magnetic bead concentration and transfer process can be completed within one minute, which is compatible with other multi-phase based methods.[191,194,196] The bead recovery rate of the μCOVE chip was further determined by pulling different amounts of magnetic beads conjugated with FITC-labeled BSA through all seven vessels in the chip. By measuring the fluorescence before and after the assay sequence, a total bead loss of $\leq 2\%$ was consistently observed for the range of bead quantity that we typically used with the current chip design, *i.e.*, from 5×10^5 to 1×10^6 beads (Figure 4-2D). In contrast, multi-phase separation/washing requires a critical bead mass to overcome the surface tension, which determines the bead loss and is directly affected by the sample matrices and buffer composition.[194,197] A recently developed AirJump method based on the air/aqueous interface requires many more beads to achieve a total bead loss of less than 15%[194] (Table 4-1).

Table 4-1. Comparison of Different Immunoassay Platforms

	96-well Plate ELISA	**IFAST**[192]	**AirJump**[194]	**SlipChip**[195]	**μCOVE** (this work)
Multi-phase System	No	Oil/Aqueous	Oil/Aqueous	Oil/Aqueous	No
Separation/ Washing Approach	Mechanical agitation	Volume pinning by surface tension	Volume pinning by surface tension	Serial dilution	Hydrodynamic counter flow
Wash Time per Step	~10 min (3×)	< 1 min bead aggregating & pulling	1-2 min bead aggregating & pulling	Slow (4 cycles of diffusion & bead mixing)	< 1 min bead aggregating & pulling
Minimal Bead Amount Tested	N/A	~3×10^6	~9×10^6	N/A	~5×10^5
Bead Loss	N/A	Bead loss during traverse	≤ 15%	≤ 3%	≤ 2%
Lowest concentration detected	20 pg mL^{-1} EGFR	20 pg mL^{-1} PSA	N/A (only for sample prep.)	400 pg mL^{-1} insulin (LOD: 76 pg mL^{-1})	0.2 pg mL^{-1} EGFR (LOD: 0.082 pg mL^{-1}); 3.2 pg mL^{-1} CEA (LOD: 1 pg mL^{-1})

4.3.3 μCOVE-based Immunoassays

We sought to develop the μCOVE chip for biomarker detection by targeting the human CEA and EGFR as the model targets. Overexpression of CEA and EGFR proteins has been widely used for clinical diagnosis and treatment of cancer, such as colorectal and lung cancer.[198,199] We first developed the μCOVE-based CEA ELISA in which the hydrodynamic washing method was used without extended incubation of magnetic beads in the washing buffer vessels (Figure 4-1D). Representative fluorescence images of the microreactor acquired after 30 min of enzymatic signal amplification reaction are displayed in Figure 4-3A, which shows a very low background level for the PBS blank

and increasing the fluorescence signal along with the CEA concentration. A logarithmic calibration curve was constructed by plotting the averaged fluorescence intensity in the microreactor as a function of the CEA concentration (Figure 4-3B). We demonstrated quantitative detection of the CEA over an extensive dynamic range of five orders of magnitude (3.2 pg mL^{-1} to 32 ng mL^{-1}). A low theoretical LOD of 1.0 pg mL^{-1} was determined by calculating the value of the blank signal plus three standard deviations (S.D.), which is comparable with the recently reported microfluidic methods[200,201] and biosensors,[202-205] for sensitive detection of CEA protein. It is noted that for this pilot assay development stage, the fluorogenic signal amplification was performed with 0.2 mM RGP and 30 min incubation, which were selected from the reaction conditions commonly used in the literature[206,207] and can be further optimized to improve the assay sensitivity (see Figure 4-3). An average of 7.1% relative standard deviation (RSD, n = 3) was obtained with multiple devices across the test concentration range, which is comparable with that reported for the commercial human CEA ELISA assays (*e.g.*, < 12% for the Invitrogen Kit; 4.4% for the Abcam SimpleStep Kit; and < 12% for the BioVision Kit). To characterize the specificity of our assay, we detected the CEA (3.2 ng mL^{-1}) in comparison with the PBS blank containing 1% BSA, IgG (1 ng mL^{-1}), and the EGFR (2 ng mL^{-1}) with anti-CEA mAb labeled magnetic beads, respectively. μCOVE-based ELISA detection of the CEA with a low background measured from the blank, IgG and EGFR was demonstrated, as shown in Figure 4-3C, which suggests the good specificity of the assay for the CEA.

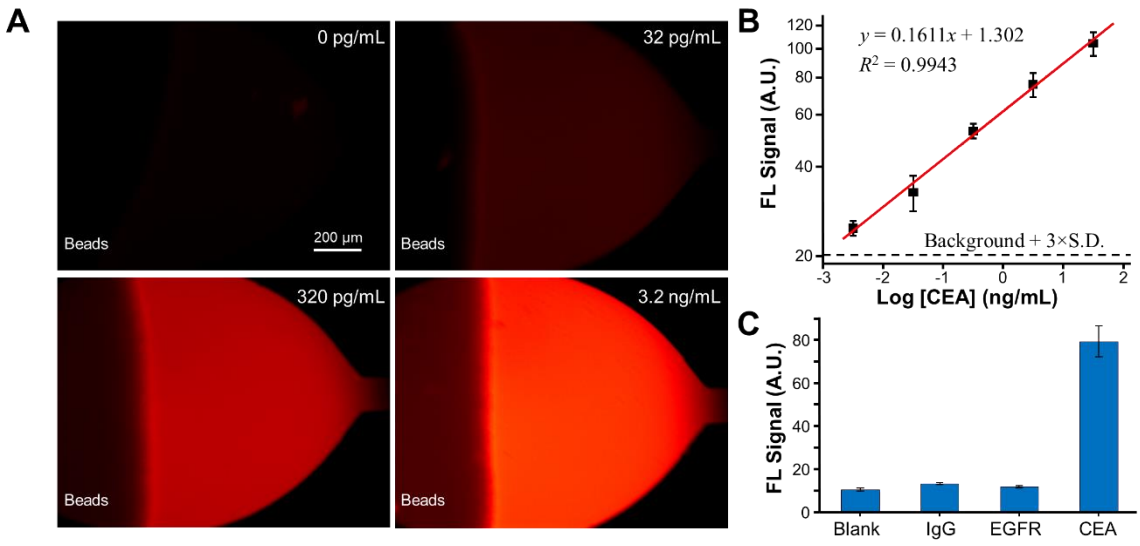

Figure 4-3. Detection of CEA using μCOVE chips. (**A**) Representative fluorescence images (false color) and (**B**) log–log calibration curve of detecting a serial dilution of CEA protein. Error bars represent one standard deviation (S.D., $n \geq 3$) obtained from different chips. The linear plot was obtained by least-squares fitting. Dashed line indicates the background plus three times the S.D. measured with the PBS blank. (**C**) Specificity evaluation of the CEA assay by measuring the PBS blank, IgG (1 ng mL^{-1}), EGFR (2 ng mL^{-1}), and CEA (3.2 ng mL^{-1}), respectively. Error bars indicate one S.D. (n = 3). Enzymatic detection conditions for (A–C): [RGP] = 0.2 mM; incubation time = 30 min. FL: fluorescence; A.U.: arbitrary unit.

To further assess the μCOVE chip for different analyte targets, we attempted to establish an immunoassay for the EGFR. The assay performance was optimized by fine tuning the assay protocol for the CEA, especially the enzymatic reaction for fluorescence readout. It was observed that increasing the RGP concentration from 0.2 mM to 0.5 mM led to only a slightly higher non-specific background but significant enhancement in signals (Figure 4-4A). Higher RGP concentrations were seen to result in much higher background levels, which may in part attributed to the faster hydrolysis rate. To determine the optimal reaction time with 0.5 mM RGP, we studied the real-time enzymatic depletion of the RGP substrate for measuring the EGFR at various

concentrations. As displayed in Figure 4-4B, a constant reaction rate over 60 min incubation was observed at the EGFR concentration of 20 pg mL^{-1}, while at 200 pg mL^{-1} a ~2.8-fold increased reaction rate was obtained within ~30 min and reduced afterwards, implying significant substrate depletion. Therefore, we chose to use the reaction time of 30 min in this work to afford a high sensitivity for quantitative detection of the EGFR. A shorter reaction time permits EGFR quantification at higher levels but will result in a lower readout signal and thus decreased detection sensitivity. Titration experiments using the optimized assay conditions showed quantitative detection of the EGFR with a calculated LOD of 0.082 pg mL^{-1} (Figure 4-4C). Such a LOD at the fg mL^{-1} level is comparable with that of some sensitive biosensors and microdevices, such as nanoparticle-based bio-bar codes assisted by PCR amplification,[208] whispering-gallery microcavity,[209] and microfluidic digital ELISA.[210] The detection signal was found to level off rapidly when the concentration was increased above 2 ng mL^{-1}, indicating a dynamic range of 4 orders of magnitude for EGFR detection. Specific detection of the EGFR was also validated by comparing with the measurements of the PBS blank, IgG, and CEA with the anti-EGFR immunomagnetic beads (Figure 4-4D). Collectively, these results for both CEA and EGFR assays demonstrate the effectiveness of the rapid hydrodynamic washing method implemented in our μCOVE device to remove the unbound agents and non-specific background to enhance the signal-to-noise ratio.

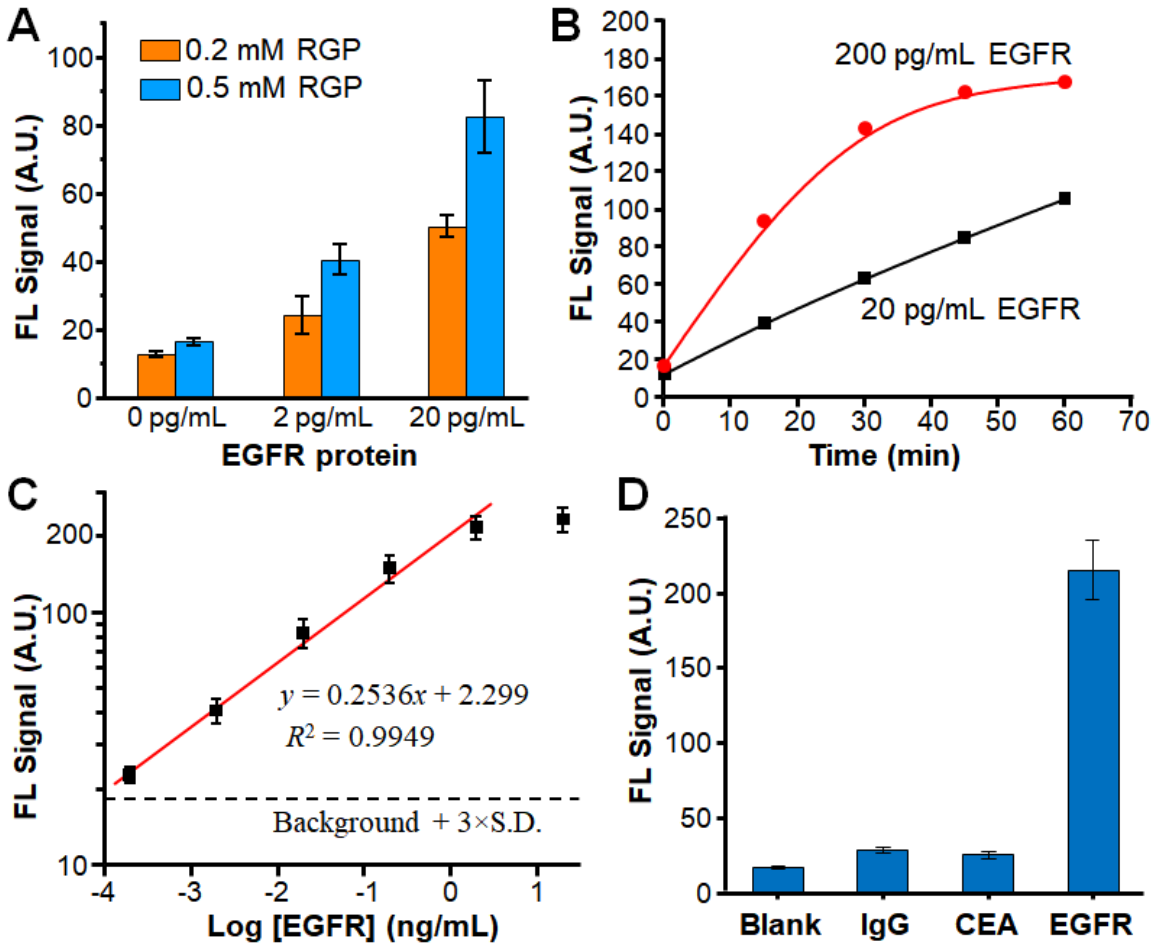

Figure 4-4. Development of μCOVE-based EGFR ELISA. (**A**) Effects of the RGP substrate concentration on enzymatic detection of the EGFR. Error bars represent one S.D. (n = 3). (**B**) Time-lapse measurements of β-gal catalyzed fluorogenic reaction for detection of EGFR at 20 and 200 pg mL^{-1}, respectively. 0.5 mM RGP was used in this case. (**C**) Calibration curve of detecting a serial dilution of the EGFR standard. Error bars represent one S.D. ($n \geq 3$) from different chips. The linear plot was obtained by least-squares fitting. The dashed line indicates the background plus three times the S.D. measured with the PBS blank. (**D**) Specificity evaluation of the EGFR assay by measuring the PBS blank, IgG (1 ng mL^{-1}), CEA (3.2 ng mL^{-1}), and EGFR (2 ng mL^{-1}), respectively. Error bars indicate one S.D. (n = 3).

To demonstrate the direct applicability of the μCOVE-based ELISA to the analysis of complex biological samples, we employed it to quantify the expression level of the EGFR in the crude A431 whole cell lysate. Human epidermoid carcinoma A431 cells overexpress the EGFR and thus are often used as a positive control cell line for

EGFR expression. BSA-coated magnetic beads were used as a negative control to assess the non-specific background. For comparison, two washing methods were used: the rapid hydrodynamic washing and the 10 min washing method in which the beads were pulled into a washing vessel and incubated for 10 min with rotation. As seen in Figure 4-5, measurements of the EGFR in the A431 crude lysate samples diluted to 0.376 and 3.76 μg mL^{-1} yielded the fairly consistent levels of the non-specific background and detection signals between the two washing methods. Additional 10 min washing reduced the background but also led to a lower detection signal. This is mainly owing to enhanced dissociation of antibody-captured targets and the loss of beads during washing. Two washing methods resulted in the comparable signal levels after background correction. The signal-to-background ratios for the hydrodynamic washing *vs.* the 10 min washing were calculated to be 6.41 ± 1.17 *vs.* 6.77 ± 1.21 (0.376 μg mL^{-1} lysate) and 7.08 ± 1.32 *vs.* 6.86 ± 0.85 (3.76 μg mL^{-1} lysate), respectively, which are not significantly different between the two methods as assessed by Student's t test. Applying the standard curve established immediately prior to the lysate measurements (Figure 4-4C), the average EGFR level in the original A431 cell lysate measured with the 0.376 and 3.76 μg mL^{-1} dilutions was calculated to be 326 ng mL^{-1} and 377 ng mL^{-1}, respectively, which closely matched with each other. These results further validate the effectiveness of rapid hydrodynamic washing for the μCOVE-based immunoassay, enabling rapid and quantitative analysis of proteins in complex biological matrices. The whole assay was completed in 4 h, including an excess of 2 h incubation for protein capture to ensure high sensitivity. The assay time can be further shortened to ~2 h for detection of relative abundant targets. This turnaround time is much shorter than conventional ELISA, which

normally takes 6 h to overnight,[181] and comparable to some point-of-care ELISA chips reported.[211]

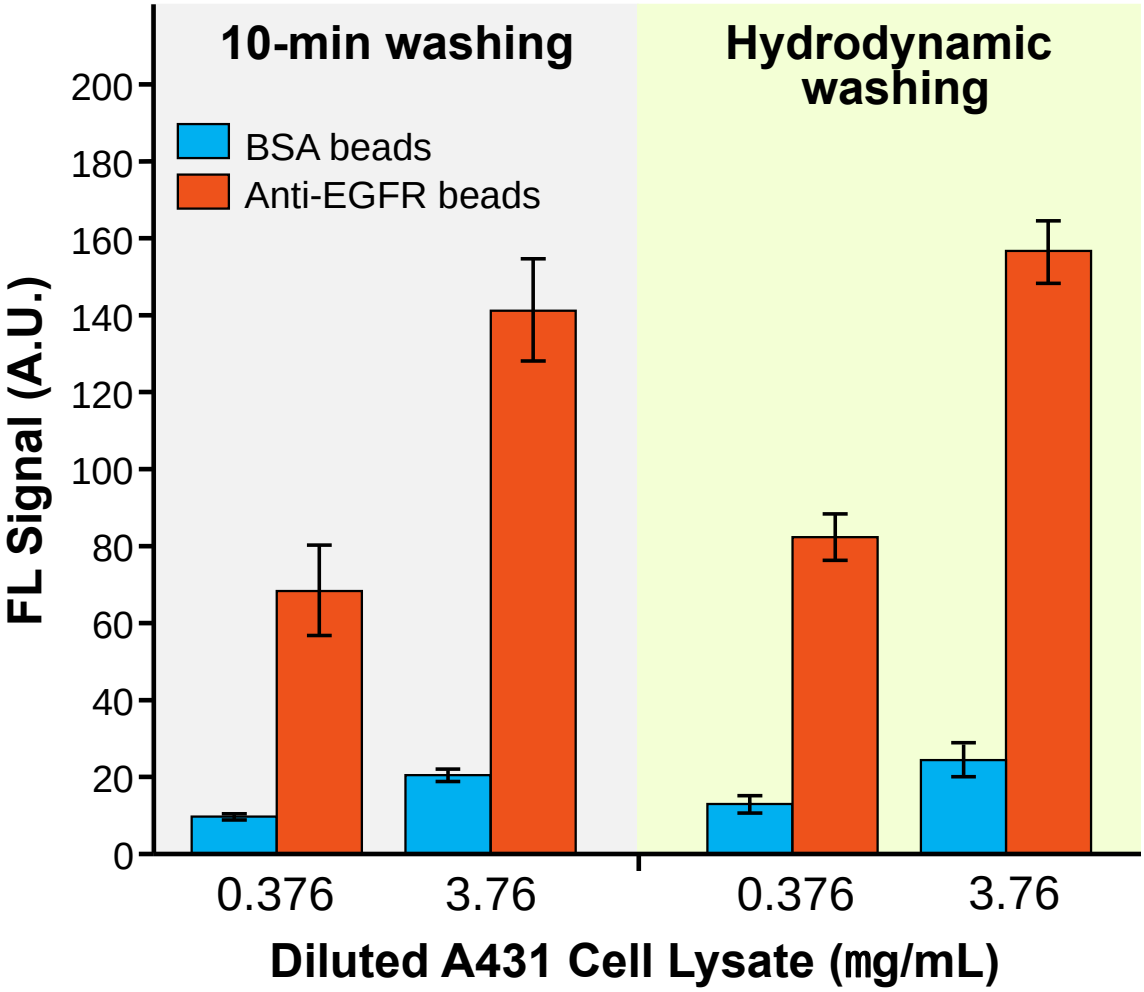

Figure 4-5. Detection of EGFR in the A431 cell lysate. The lysate (3.76 mg mL^{-1}) was prepared from human epidermoid carcinoma A431 cells overexpressing the EGFR and diluted in PBSW solution by 1000 and 10000 times. The diluted cell lysate samples were assayed using magnetic beads coated with the BSA and anti-EGFR antibody, respectively. The detection performance with the hydrodynamic washing was compared to that obtained by the 10 min washing method where beads were washed for additional 10 min in each washing vessel. Error bars represent one S.D. ($n \geq 3$).

4.4 Conclusion

In summary, we have developed a pneumatically gated μCOVE chip which employs the communicating vessel principle as a simple means to generate a fast transient hydrodynamic flow for effective washing without the need for excessive incubation. Compared to traditional microfluidic immunoassays, our method greatly shortens and simplifies the washing steps to expedite the assay workflow. In contrast to the stationary multi-phase microfluidics developed for fast immuno-bead washing (Table 4-1), the single-phase, pneumatically gated μCOVE chip not only facilitates the transfer of magnetic beads to streamline the assay workflow, but also overcomes the limitations associated with the multi-phase operation. Our proof-of-concept studies demonstrated that the μCOVE device can afford highly sensitive and quantitative detection of two protein biomarkers, the CEA and EGFR with a LOD as low as the sub-picogram per mL level. Direct detection of the expression of the EGFR in the crude A431 cell lysate was also investigated to further validate the device for fast washing to expedite the multi-step immunomagnetic assay, enabling rapid and quantitative protein analysis in complex biological matrices. Overall, our work should present a novel microfluidic platform that combines the merits of the stationary multi-phase microfluidics and the flow-based microfluidics. The simplicity and high analytical performance of this system would make it a useful platform for a broad range of applications in biological research and clinical diagnosis.

Chapter 5 Feasibility Study of An Integrated Microfluidic Chip for on-chip Exosome Isolation, Lysis, and Digital Detection of Exosomal Proteins

5.1 Introduction

Exosomes are nano-sized membranous vesicles (30–150 nm) released from multivesicular bodies into extracellular environments.[38] Exosomes carry many biomolecules, including proteins, mRNAs and micro RNAs (miRNAs), reflecting their cellular origin.[38,47] Studies have shown that exosomes get involved in many physiological and pathological processes such as cancer progression and metastasis,[44,45,116] and tumor-derived exosomes are highly expressed in cancer patient blood.[48,49] Therefore, exosomes are very promising cancer biomarkers for non-invasive cancer diagnosis.

The most common technique for exosome purification is multi-step ultracentrifugation. However, this technique is labor-intensive, time-consuming, and incapable of differentiating exosomes from other vesicles with similar size.[212] Loss, contamination, and damage of exosomes may occur during ultracentrifugation.[123] On the contrary, immunoaffinity capture based exosome purification can yield high purity, specificity, and recovery.[213]

We previously reported a microfluidic continuous-flow platform (ExoSearch chip) for exosome isolation by immunomagnetic beads streamlined with multiplexed detection of exosomes.[99] Although exosomes were rapidly and effectively isolated by immunomagnetic beads, removing unbound residue by washing was tedious due to the length of microchannels (~25.5 cm). Thus, we further developed a pneumatically gated microfluidic communicating vessel chip (μCOVE) for simplified and expedited

immunoassays.[79] Benefiting from the chip design, the beads were washed and isolated near-instantaneously with minimal residue and bead loss.

Here we developed a prototype of microfluidic chip integrating μCOVE units with a lysis chamber and a detection chamber with micropillars for on-chip exosome isolation, lysis, and digital detection of exosomal proteins (Figure 5-1). Different from analog detection that measures signal intensity in a bulk solution, digital detection directly measures signal counts. Taking advantage of its low limit of detection (LOD) and highly sensitivity, digital detection can even achieve single-molecule analysis.[100,101] Many digital detection methods have been developed, but the digitization of signals is highly dependent on multi-phase (oil/water) based sample dispersion and geometry of the microfluidic devices, including droplet,[103-105] microwell,[106,107] microchannel with chamber,[80,93,108] and printing.[109] In our work, we used enzyme-labeled fluorescence 97 phosphatase substrate (ELF 97) for digital signal generation. ELF 97 is normally used for cell staining and biomolecule labeling.[214,215] The dephosphorylated product, ELF-97 alcohol, is a fluorescent precipitate insoluble in water (Figure 5-3A). However, to our knowledge, ELF 97 has not been used in digital enzyme-linked immunosorbent assay (ELISA). The detection chamber fabricated with micropillars (Figure 5-1C) enhanced the localization of ELF 97 alcohol precipitates for digital signal readout. We validated our platform by detecting standard human epidermal growth factor receptor 2 (HER2) protein and its expression level in exosomes collected from MDA-MB-453 cell culture media.

5.2 Materials and Methods

5.2.1 Chip Fabrication

The microstructures on silicon wafers were fabricated by photolithography. The photomasks were designed with AutoCAD and printed on transparent plastic sheets. The silicon wafers were cleaned with piranha solution (75% sulfuric acid and 25% hydrogen peroxide) for 30 min. SU-8 photoresist (MicroChem) were spin coated onto the wafers with the parameters recommended by the manufacturer's protocol. For the flow layer, two-step exposure method was used to fabricate micropillars and the rest parts of channels. In brief, detection chambers with micropillars were firstly fabricated on SU-8 2010 (15 μm in thickness), followed by fabricating the rest parts of flow layer on additional 30 μm thick SU-8 2025 (45 μm in total). Pneumatic layer and surface patterning chip were fabricated on 50 μm and 30 μm thick SU-8 2025, respectively. The SU-8 molds were treated with trichloro(1*H*,1*H*,2*H*,2*H*-perfluorooctyl)silane (Sigma-Aldrich) by gas-phase silanization under vacuum for at least 4 h. The two-layer poly(dimethylsiloxane) (PDMS) microchips (Figure 5-1B) were fabricated using standard multilayer soft lithography. PDMS base and curing agent (Dow Corning) were mixed at a 10:1 ratio and degassed under vacuum for surface patterning chip, flow layer, and pneumatic layer. To make the surface patterning chip and the pneumatic layer, PDMS mixture was poured onto the mold and cured in an oven at 70 °C for at least 2 h. The PDMS pieces were peeled off from the mold, cut, and punched to make the inlet and outlet of the surface patterning chip as well as the pneumatic connection holes of the pneumatic layer. To make the flow layer, a thin PDMS membrane was spin coated onto the mold and cured at 70 °C for 30 min in an oven. The two layers were treated by

UV/ozone for 5 min, manually aligned under a stereomicroscope, and permanently bonded by baking at 70 °C overnight. The two-layer PDMS slabs were then peeled off from the mold and reservoirs were punched. To immobilize anti-HER2 capture antibody (DYC1129-2, R&D systems) on a glass slide, a piranha pre-cleaned glass slide was treated with 2% 3-aminopropyltriethoxysilane (APTES, Acros Organics) in anhydrous toluene (Acros Organics) for 4 h and heated for 2 h at 110 °C. Then the glass slide was treated with 2.5% glutaraldehyde (Fisher Scientific) in deionized water for 2 h at room temperature, attached with a surface patterning chip (Figure 5-1A), and incubated with 4 μL of 180 μg mL^{-1} anti-HER2 capture antibody in phosphate-buffered saline (PBS, Corning Cellgro) overnight at room temperature. The excess anti-HER2 capture antibody was washed with 0.1% bovine serum albumin (BSA, Thermo Fisher Scientific) in PBS, the surface patterning chip was peeled off, and the glass slide was aligned with the two-layer PDMS assay chip.

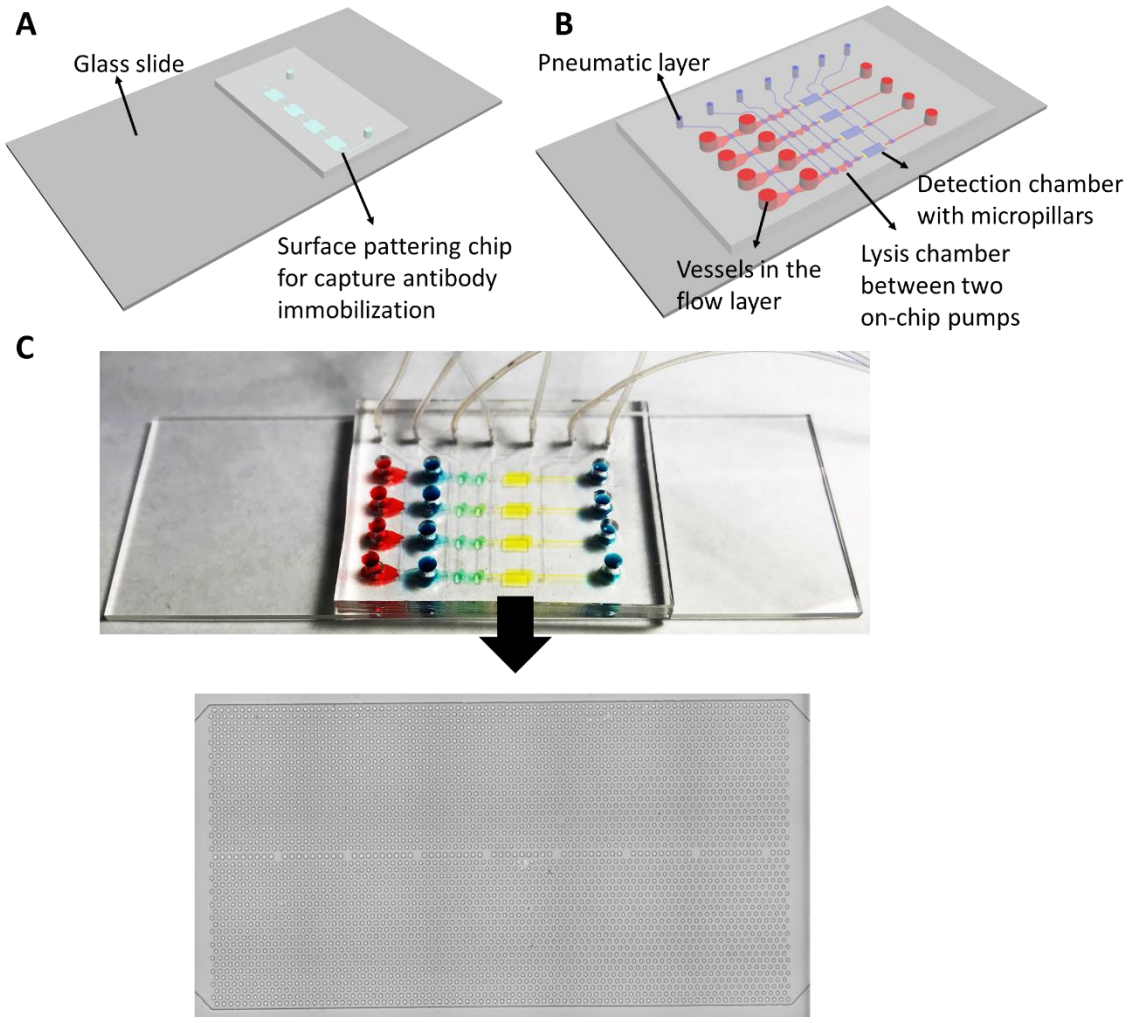

Figure 5-1. Integrated microfluidic chip for on-chip exosome isolation, lysis, and digital detection of exosomal proteins. (**A**) Schematic illustration of the surface patterning chip design. The surface patterning chip consists of four incubation chambers corresponding to the detection chambers on the two-layer microfluidic assay chip. (**B**) Schematic illustration of the two-layer microfluidic assay chip design. The microfluidic assay chip integrates four parallel channels (45 μm high, red), each consisting of two vessels (~10 μL), a lysis chamber with two on-chip pumps, a detection chamber with micropillars (15 μm high, yellow), and a waste reservoir. The on-chip valves and pumps are actuated by the pneumatic channels (purple) in the top layer. (**C**) A photograph of the chip filled with different food dyes in different functional units with gates closed, and a microscopic photograph of the detection chambers with micropillars.

5.2.2 Magnetic Beads Preparation

Briefly, 100 μL of 30 mg mL^{-1} carboxylic acid coated magnetic beads (Dynabeads M-270 Carboxylic Acid, Invitrogen) were transferred to a 1.5 mL microcentrifuge tube and washed twice with 100 μL of 25 mM 2-(*N*-morpholino)ethanesulfonic acid (MES, pH 5, Sigma-Aldrich) for 10 min. The beads were then activated with 50 μL of freshly prepared 50 mg mL^{-1} *N*-ethyl-*N*′-(3-dimethylaminopropyl)carbodiimide hydrochloride (EDC, Sigma-Aldrich) and 50 μL of 50 mg mL^{-1} *N*-hydroxysuccinimide (NHS, Sigma-Aldrich) with rotation at room temperature for 30 min. The activated beads were washed twice with 100 μL of 25 mM MES buffer (pH 5) and then mixed with 60 μL of 1 mg mL^{-1} anti-CD81 (302-820, Ancell) in 40 μL of 25 mM MES (pH 5) overnight at 4 °C with rotation. After incubation, the supernatant was removed and the beads were blocked by 100 μL of 50 mM ethanolamine (Sigma-Aldrich) in phosphate-buffered saline (PBS, Corning Cellgro) for 60 min at room temperature with rotation. Finally, the anti-CD81 labeled magnetic beads were washed four times with 100 μL of washing buffer (0.1% BSA and 0.1% Tween-20 in PBS), resuspended in 100 μL PBS, and stored at 4 °C.

5.2.3 Exosome Purification by Ultracentrifugation

Exosomes were purified by multi-step ultracentrifugation from MDA-MB-453 cell culture media, a generous gift from Prof. Liang Xu's group. First, 15 mL MDA-MB-453 cell culture media were centrifuged at 3000 RPM (30 min at 4 °C). The supernatants were then transferred to a new tube and centrifuged at 15000 g (45 min at 4 °C). The supernatants were again transferred to another new tube and centrifuged at 100000 g (2 h

at 4 °C). After ultracentrifugation, the supernatants were discarded, and the exosome pellets were suspended in 150 μL PBS, aliquoted, and stored at −80 °C. The concentration of exosomes was 3.57×10^{12} particles mL^{-1}, analyzed by nanoparticle tracking analysis (NTA, NanoSight).

5.2.4 Microfluidic Immunoassay and Exosomal Protein Analysis

The on-chip assay was performed following the procedure illustrated in Figure 5-2A. The on-chip pneumatic gates and valves were actuated at 40 kPa pressure and −70 kPa vacuum controlled by a homemade solenoid controller *via* a LabVIEW program. Standard HER2 protein (DYC1129-2, R&D systems) and exosomes were prepared in PBS working solution (PBSW, pH 7.4) containing 0.1% BSA. Biotinylated anti-HER2 detection antibody (DYC1129-2, R&D systems) was prepared in PBSW containing 0.05% Tween-20. Streptavidin conjugated alkaline phosphatase (ALP, R&D systems) and ELF 97 (Life Technologies) were prepared in 25 mM Tris (Fisher Scientific) containing 1% BSA, 0.05% Tween-20, 100 mM NaCl (Fisher Scientific), and 10 mM $MgCl_2$ (Thermo Fisher Scientific).

For standard HER2 quantification, 20 μL of a series of HER2 dilution (0.5 pg mL^{-1} to 100 pg mL^{-1}) was pumped from the second vessel through detection chamber by 5-step on-chip pumping (Figure 5-2B) for 2 h. For HER2 quantification in MDA-MB-453 exosomes, 5 μL of 10-fold dilution of purified exosomes was mixed with 2 μL of 30 mg mL^{-1} anti-CD81 labeled magnetic beads in the first vessel and incubated for 2 h with rotation. After incubation, the sample solution was removed by aspiration, and the magnetic beads were transferred into the second vessel by a magnet and washed with 10

μL washing buffer (0.05% Tween 20 in PBS) by hydrodynamic counter flow when the gate was opened. Then the magnetic beads were magnetically drawn into the lysis chamber preloaded with RIPA lysis buffer (Thermo Fisher Scientific) and reacted for 5 min. The gate was then opened to connect lysis chamber with detection chamber, and the exosome lysate was incubated for 2 h at room temperature. After the capture of standard HER2 or exosomal HER2, 10 μL washing buffer was pumped within 2 min. Then 10 μL of 180 ng mL^{-1} anti-HER2 detection antibody was pumped from the second vessel through detection chamber for 1 h, followed by 10 μL washing buffer within 2 min. Afterwards, 10 μL of 1000-fold ALP dilution was pumped from the second vessel through detection chamber for 30 min, followed by 10 μL washing buffer within 2 min. Finally, 7.5 μL of 0.5 mM ELF 97 was quickly pumped from the second vessel through detection chamber within 2 min and incubated for 30 min at 35 °C with the valves on both sides of the detection chamber closed. Fluorescence images were acquired using an inverted epifluorescence microscope (Nikon) equipped with a 20× objective, an automatic stage, and a scientific CMOS camera (Prime 95B, Teledyne Photometrics), and analyzed with ImageJ (NIH, https://imagej.nih.gov/ij/) to measure the signal counts.

5.3 Results and Discussion

5.3.1 Chip Design and Operation

The surface patterning chip consists of four incubation chambers corresponding to the detection chambers on the two-layer microfluidic assay chip (Figure 5-1A). An APTES treated glass slide was activated with glutaraldehyde and coated with anti-HER2 capture antibody in surface patterning chip. Then the surface patterning chip was peeled

off and the glass slide was aligned with the two-layer PDMS chip to assemble the whole assay chip. The microfluidic assay chip integrates four parallel channels (45 μm high), each consisting of two vessels (~10 μL) from μCOVE design,[79] a lysis chamber with two on-chip pumps, a detection chamber with micropillars (15 μm high, 15 μm in diameter and 15 μm interval), and a waste reservoir in the bottom flow layer (Figure 5-1B). The adjacent functional units are disconnected by the normally-closed gates that can be lifted by the pneumatic channels in the top layer. The microfluidic immunoassay workflow is schematically illustrated in Figure 5-2A. The performance of the hydrodynamic flow induced by hydrostatic pressure for bead washing and pneumatically gated magnetic manipulation of beads were characterized in our previous work.[79] The second gate (input) and the two on-chip pumps (diaphragm and output) compose the pneumatically actuated on-chip pumping system (Figure 5-2A). The five-step pumping mode is automatically controlled by a LabVIEW program. Initially all the three valves are closed. Then the three valves are subsequently on (vacuum) or off (pressure) in a proper order (Figure 5-2B). The flow rate can be controlled by adjusting the time of each pumping step. For example, when the first step is 36 s and the rest of steps are 500 ms, the flow rate is approximately 10 μL h^{-1}.

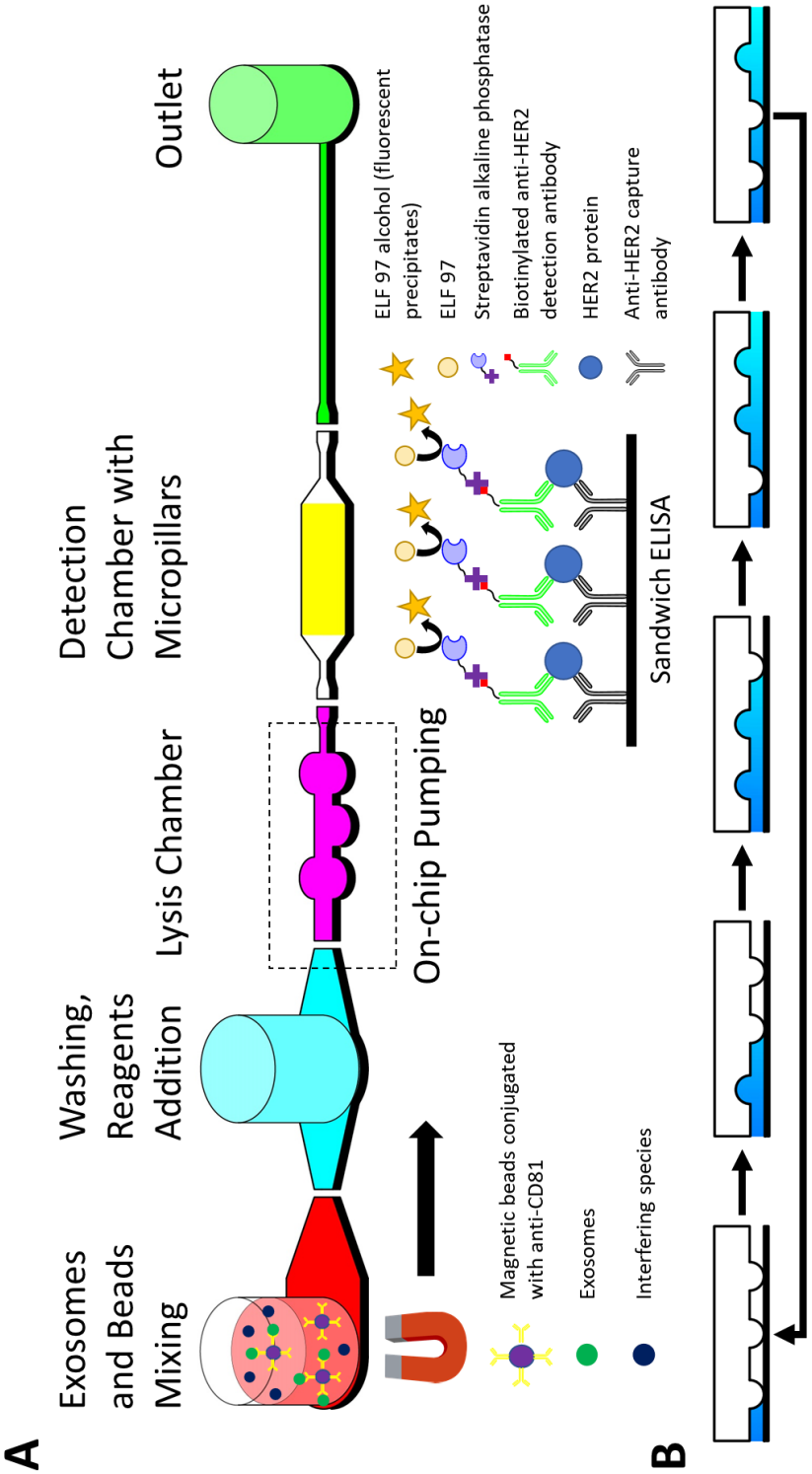

Figure 5-2. (**A**) Schematic illustration of the assay workflow. Magnetic beads are mixed with exosomes in the first vessel. After incubation, lysis buffer is pre-loaded into lysis chamber and the second chamber is refilled with more washing buffer. The first two gates

are pneumatically opened one at a time to pull the beads across the second vessel with a magnet. The beads are moved into the lysis chamber and all gates are closed. The second and third gates as well as the detection chamber are then opened after exosome lysis to drive lysate into detection chamber, and the second gate is immediately closed. After exosomal proteins are captured, the second, third and fourth gates are opened to flow the washing buffer and reaction reagents (biotinylated detection antibody, ALP, and ELF 97) sequentially into detection chamber. During the last enzymatic reaction, micropillars are pushed back and the third and fourth gates are closed to prevent flow. The fluorescent precipitates, ELF 97 alcohol, are produced by the enzymatic reaction and measured by an inverted epifluorescence microscope. (**B**) Schematic illustration of the 5-step pumping system that consists of the second gate (input), and the two on-chip pumps (diaphragm and output). The three pumps are pneumatically actuated in a proper order by software. Flow rate is controlled by adjusting frequency of each step.

5.3.2 Signal Digitization

We selected ELF 97 on purpose. ELF 97 is normally used for cell staining and biomolecule labeling.[214,215] Due to the distinct fluorescence spectra with large Stokes shift (excitation: 345 nm, emission: 530 nm) of its dephosphorylated product, ELF-97 alcohol, fluorescence signals can be easily distinguished from sample autofluorescence with lower background and more sensitivity. More importantly, ELF 97 alcohol is a water-insoluble precipitate that can well localize to the enzymatic activity site (Figure 5-3A). This unique property makes ELF 97 promising for digital detection of biomarkers. However, to our knowledge, ELF 97 has not been used in digital ELISA. Digital detection measures signal counts rather than analog detection measures signal intensity in a bulk solution. Compared with analog detection, digital detection has much lower LOD that can even achieve single molecule measurement.[100,101] The digitization of signals in previously developed methods is highly dependent on multi-phase (oil/water) based sample dispersion and geometry of the microfluidic devices. We used ELF 97 for digitization of signals without assistance of multi-phase. Even the signals were digitized, the tiny precipitates might vibrate due to Brownian motion, resulting in a blurry

background in an open chamber (Figure 5-3B). We addressed this problem by fabricating the detection chamber with micropillars. The micropillars can enhance the localization of ELF 97 precipitates to improve the accuracy of signal readout (Figure 5-3C).

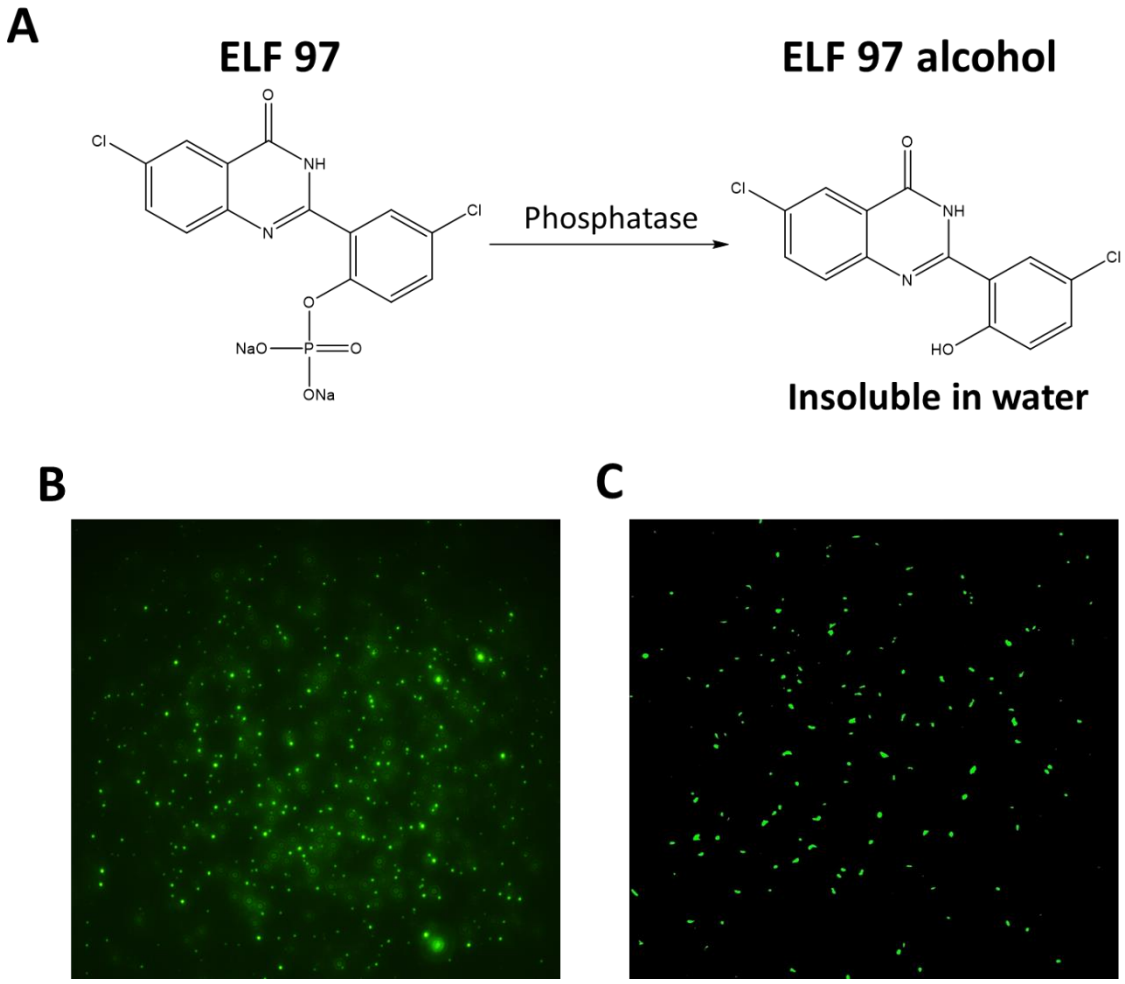

Figure 5-3. (**A**) Dephosphorylation of ELF 97. The production ELF 97 alcohol is insoluble in water. Digitization of signals in (**B**) open detection chamber and (**C**) detection chamber with micropillars. Signals generated in detection chamber with micropillars are better localized.

Quantification of HER2

For standard HER2 quantification, reaction reagents (*i.e.*, standard HER2, detection antibody, ALP, and ELF 97) were successively pumped from the second vessel through detection chamber. Washing buffers are quickly pumped in between each incubation step. We demonstrated quantitative detection of the HER2 from 0.5 pg mL^{-1} to 100 pg mL^{-1}. Figure 5-4A shows the representative fluorescence images of the detection chamber acquired after 30 min of enzymatic signal amplification reaction. A logarithmic calibration curve was constructed by plotting the signal counts as a function of the HER2 concentration (Figure 5-4B). The theoretical LOD was 32 fg mL^{-1}, calculated by blank signal plus three standard deviations (S.D.). Such a low LOD is comparable with that of other microfluidic digital ELISA.[210]

For quantification of HER2 expression level in MDA-MB-453 exosomes, exosomes were mixed with anti-CD81 labeled magnetic beads in the first vessel with all gates closed. After incubation, the beads were transferred into the second vessel and washed by hydrodynamic counter flow. Benefiting from the μCOVE design, the isolation and washing of beads were near-instantaneous with minimal residue and bead loss. The beads were then transferred into the lysis chamber preloaded with RIPA lysis buffer and the exosomes were lysed for 5 min with all gates closed. The gate between the lysis chamber and the detection chamber was opened, and vacuum was applied on the detection chamber to suck exosome lysate. The exosome lysate was incubated in the detection chamber, followed by addition of anti-HER2 detection antibody, ALP, ELF 97 and washing buffer as described above. The expression level of HER2 in MDA-MB-453 exosomes was 8.36×10^{-10} pg per exosome, calculated based on the calibration curve.

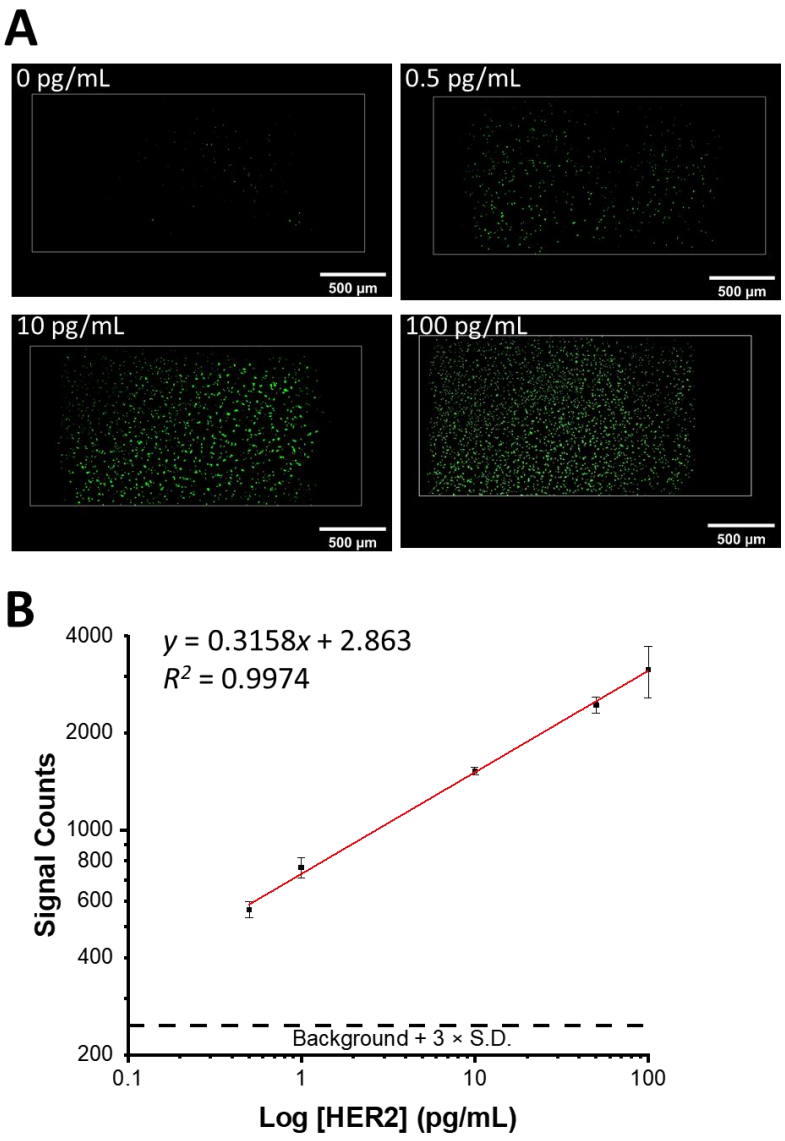

Figure 5-4. Detection of standard HER2 proteins. (**A**) Representative fluorescence images (false color). The white lines indicate the detection chamber. (**B**) Log–log calibration curve of detecting a serial dilution of HER2 proteins. Error bars represent one standard deviation (S.D., n = 3) obtained from different chips. The linear plot was obtained by least-squares fitting. Dashed line indicates the background plus three times the S.D. measured with the PBSW blank.

5.4 Conclusion

To summarize, we have developed a prototype of integrated microfluidic chip for on-chip exosome isolation, lysis, and digital detection of exosomal proteins. The near-

instantaneous bead washing and isolation with minimal residue and bead loss is benefiting from μCOVE units. The signal digitization takes advantage of precipitation of dephosphorylated ELF97 product without multi-phase assisted sample dispersion, which simplifies the chip design and operation. The specifically designed detection chambers with micropillars facilitate signal localization with more accuracy. This microfluidic chip successfully quantified standard HER2 and HER2 expression level in MDA-MB-453 exosomes. The LOD of HER2 is 32 fg mL^{-1} that comparable with that of other microfluidic digital ELISA.[210] Overall, our work should present a novel microfluidic platform for on-chip exosome isolation, lysis, and digital detection of exosomal proteins. This platform holds a potential for detections of other biomolecules in clinical applications.

Chapter 6 Conclusions and Future Directions

Cancer has become a severe health concern as the second leading cause of death in the US. Statistical data indicate that increased survival rate can be achieved if cancer is diagnosed at the early stage. However, early stage cancer diagnosis remains challenging. Conventional imaging-based cancer screening methods, including CT, PET, ultrasounds and MRI, have been developed for cancer diagnosis, but these methods are insufficient to diagnose cancer at early stage. Recently more and more studies put efforts on liquid biopsy. Many cancer biomarkers, such as CTCs, ctDNA, and EVs, have been applied in liquid biopsy for early stage cancer diagnosis. Due to the high abundance and comprehensive molecular profile, EVs, particularly exosomes, are very promising as cancer biomarkers in liquid biopsy.

In our first and second projects, we developed a microfluidic ExoSearch chip for multiplexed exosome detection. The ExoSearch chip enables simultaneous, quantitative evaluation of three exosomal tumor markers (CA-125, EpCAM, CD24) from the same exosome subpopulation with much improved measurement reproducibility (CV < 10%) and good robustness for non-invasive diagnosis of ovarian cancer. The results show comparable accuracy and diagnostic power (a.u.c. = 1.0, $p = 0.001$) with the standard Bradford assay (a.u.c. = 1.0, $p = 0.0009$). In addition, the ExoSearch chip significantly reduces consumption of sample volume (20 μL) and time (40 min), compared with Bradford assay (1 mL, 12 h). As a proof-of-concept, this work could serve as a basic platform for developing clinical tests in other diseases.

In our third project, we developed a μCOVE chip for expedited and automated immunomagnetic assays. The μCOVE chip enables near-instantaneous isolation of magnetic beads with rapid and effective washing by generating a fast transient hydrodynamic flow based on the communicating vessel principle. This single-phase μCOVE chip overcomes the limitations of residue removal and bead loss associated with the multi-phase operation. The μCOVE device can achieve highly sensitive and quantitative detection of two protein biomarkers with a LOD as low as the sub-picogram per mL level. Direct detection of EGFR expression level in A431 whole cell lysate was also investigated to further validate the capability of the μCOVE device for rapid and quantitative protein analysis in complex biological matrices.

In our fourth project, we further integrated the μCOVE units with other functional compartments for on-chip exosome isolation, lysis, and digital detection of exosomal proteins. The μCOVE units contribute to near-instantaneous bead washing and isolation with minimal residue and bead loss. ELF 97 was intentionally selected to for generating digitized signals, due to the production of ELF 97 alcohol precipitates. The detection chamber was distinctively fabricated with micropillars to reduce Brownian motion of the precipitates and enhance the localization of signals for better accuracy of signal readout. Compared to other signal digitization methods, our microfluidic chip does not require multi-phase for sample dispersion, which dramatically simplifies the chip design and operation. The LOD of HER2 is 32 fg mL^{-1}, indicating our microfluidic platform is comparable with other microfluidic ELISA. We demonstrated the feasibility of this microfluidic platform in clinical applications by quantifying the HER2 expression level in MDA-MB-453 exosomes.

Although we successfully validated that ELF 97 was potential for digital ELISA, we did not further characterize and optimize the performance of this novel microfluidic platform. For instance, we did not change the geometry of the chip including the height of the detection chamber and the size and density of the micropillars. Denser micropillars may improve the localization of digital signals, though occupy more detection areas and impede enzymatic reaction. Such variables are essential to the performance of this microfluidic platform. We can fabricate the detection chamber with different dimensions and number of micropillars to further understand how the geometry of the chip potentially change the assay performance.

Additionally, we also intend to characterize the capture efficiency of the immunomagnetic beads. In the ExoSearch chip, the mixing is driven by the continuous flow. However, in the μCOVE chip, the mixing relies on the diffusion driven by rotation. Therefore, the mixing efficiency in the μCOVE chip may not be as good as that in the ExoSearch chip. We can estimate the capture efficiency by labeling the exosomes with fluorescent dyes and detecting the fluorescence intensities before and after mixing. This can help us determine the optimal number of beads to avoid less capture efficiency (too few beads) or less lysis efficiency (too many beads in lysis chamber).

Furthermore, we are willing to advance the ELF 97 based microfluidic platform for multiplexed detection of exosomal proteins and nucleic acids. Normally the profile of a single type of molecule is not sufficient for cancer diagnosis. A panel of multiple molecular profiles is essential for clinical tests. We can modify the design of the surface patterning chip with multiple channels for immobilizing multiple capture probes. In addition, we can detect different sorts of biomarkers such as proteins and nucleic acids

simultaneously on a single microfluidic device. We can integrate the device with multiple detection units for different types of target molecules. For example, immunoassay chambers are used for protein quantification and PCR chambers are used for nucleic acid quantification. If this microfluidic device enables multiplexed detection of 3–5 or more targets, it will be very appealing to clinical applications.

The ultimate goal of our research is to achieve single-exosome profiling. Due to the tumor heterogeneity, the expression of cancer biomarkers from the same cellular origin may differ notably at single-cell level.[216] Although some works have been reported as a proof-of-concept,[217,218] single-exosome profiling still remains difficult. The high abundance makes exosomes more applicable to studying tumor heterogeneity rather than CTCs. Compared to currently developed single-cell analysis,[91-93] this microfluidic platform would be a big step forward to precision medicine if we could achieve single-exosome profiling.

References

(1) Heron, M. *Natl. Vital Stat. Rep.* **2019**, *68*, 1-76.
(2) Siegel, R. L.; Miller, K. D.; Jemal, A. *CA Cancer J. Clin.* **2019**, *69*, 7-34.
(3) Henschke, C. I. *Clin Cancer Res* **2005**, *11*, 4984s-4987s.
(4) Swensen, S. J.; Jett, J. R.; Hartman, T. E.; Midthun, D. E.; Sloan, J. A.; Sykes, A. M.; Aughenbaugh, G. L.; Clemens, M. A. *Radiology* **2003**, *226*, 756-761.
(5) Lowe, V. J.; Boyd, J. H.; Dunphy, F. R.; Kim, H.; Dunleavy, T.; Collins, B. T.; Martin, D.; Stack, B. C., Jr.; Hollenbeak, C.; Fletcher, J. W. *J. Clin. Oncol.* **2000**, *18*, 651-658.
(6) Tsuyoshi, H.; Yoshida, Y. *J. Obstet. Gynaecol. Res.* **2017**, *43*, 1687-1699.
(7) Zhi, H.; Ou, B.; Luo, B. M.; Feng, X.; Wen, Y. L.; Yang, H. Y. *J. Ultrasound Med.* **2007**, *26*, 807-815.
(8) Halpern, E. J. *Rev. Urol.* **2006**, *8 Suppl 1*, S29-37.
(9) Morrow, M.; Waters, J.; Morris, E. *Lancet* **2011**, *378*, 1804-1811.
(10) DeMartini, W.; Lehman, C.; Partridge, S. *Acad. Radiol.* **2008**, *15*, 408-416.
(11) Valk, P. E.; Abella-Columna, E.; Haseman, M. K.; Pounds, T. R.; Tesar, R. D.; Myers, R. W.; Greiss, H. B.; Hofer, G. A. *Arch. Surg.* **1999**, *134*, 503-511; discussion 511-503.
(12) Ambrosini, V.; Nicolini, S.; Caroli, P.; Nanni, C.; Massaro, A.; Marzola, M. C.; Rubello, D.; Fanti, S. *Eur. J. Radiol.* **2012**, *81*, 988-1001.
(13) Rosen, E. L.; Eubank, W. B.; Mankoff, D. A. *Radiographics* **2007**, *27 Suppl 1*, S215-229.
(14) Raes, F.; Sobilo, J.; Le Mee, M.; Retif, S.; Natkunarajah, S.; Lerondel, S.; Le Pape, A. *PLoS One* **2016**, *11*, e0153532.
(15) Kransdorf, M. J.; Murphey, M. D. *AJR Am. J. Roentgenol.* **2000**, *175*, 575-587.
(16) Fei, B.; Schuster, D. M. *AJR Am. J. Roentgenol.* **2017**, *209*, 255-269.
(17) De Rubis, G.; Rajeev Krishnan, S.; Bebawy, M. *Trends Pharmacol. Sci.* **2019**, *40*, 172-186.
(18) Ilie, M.; Hofman, V.; Long-Mira, E.; Selva, E.; Vignaud, J. M.; Padovani, B.; Mouroux, J.; Marquette, C. H.; Hofman, P. *PLoS One* **2014**, *9*, e111597.
(19) Cristofanilli, M.; Budd, G. T.; Ellis, M. J.; Stopeck, A.; Matera, J.; Miller, M. C.; Reuben, J. M.; Doyle, G. V.; Allard, W. J.; Terstappen, L. W.; Hayes, D. F. *N. Engl. J. Med.* **2004**, *351*, 781-791.
(20) Kapeleris, J.; Kulasinghe, A.; Warkiani, M. E.; Vela, I.; Kenny, L.; O'Byrne, K.; Punyadeera, C. *Front. Oncol.* **2018**, *8*, 311.
(21) Krebs, M. G.; Sloane, R.; Priest, L.; Lancashire, L.; Hou, J. M.; Greystoke, A.; Ward, T. H.; Ferraldeschi, R.; Hughes, A.; Clack, G.; Ranson, M.; Dive, C.; Blackhall, F. H. *J. Clin. Oncol.* **2011**, *29*, 1556-1563.
(22) Riethdorf, S.; Muller, V.; Zhang, L.; Rau, T.; Loibl, S.; Komor, M.; Roller, M.; Huober, J.; Fehm, T.; Schrader, I.; Hilfrich, J.; Holms, F.; Tesch, H.; Eidtmann, H.; Untch, M.; von Minckwitz, G.; Pantel, K. *Clin Cancer Res* **2010**, *16*, 2634-2645.
(23) Nicolazzo, C.; Raimondi, C.; Mancini, M.; Caponnetto, S.; Gradilone, A.; Gandini, O.; Mastromartino, M.; Del Bene, G.; Prete, A.; Longo, F.; Cortesi, E.; Gazzaniga, P. *Sci. Rep.* **2016**, *6*, 31726.

(24) Smerage, J. B.; Barlow, W. E.; Hortobagyi, G. N.; Winer, E. P.; Leyland-Jones, B.; Srkalovic, G.; Tejwani, S.; Schott, A. F.; O'Rourke, M. A.; Lew, D. L.; Doyle, G. V.; Gralow, J. R.; Livingston, R. B.; Hayes, D. F. *J. Clin. Oncol.* **2014**, *32*, 3483-3489.
(25) Antonarakis, E. S.; Lu, C.; Wang, H.; Luber, B.; Nakazawa, M.; Roeser, J. C.; Chen, Y.; Mohammad, T. A.; Chen, Y.; Fedor, H. L.; Lotan, T. L.; Zheng, Q.; De Marzo, A. M.; Isaacs, J. T.; Isaacs, W. B.; Nadal, R.; Paller, C. J.; Denmeade, S. R.; Carducci, M. A.; Eisenberger, M. A., et al. *N. Engl. J. Med.* **2014**, *371*, 1028-1038.
(26) Leary, R. J.; Kinde, I.; Diehl, F.; Schmidt, K.; Clouser, C.; Duncan, C.; Antipova, A.; Lee, C.; McKernan, K.; De La Vega, F. M.; Kinzler, K. W.; Vogelstein, B.; Diaz, L. A., Jr.; Velculescu, V. E. *Sci. Transl. Med.* **2010**, *2*, 20ra14.
(27) Beck, J.; Urnovitz, H. B.; Riggert, J.; Clerici, M.; Schutz, E. *Clin. Chem.* **2009**, *55*, 730-738.
(28) Dawson, S. J.; Tsui, D. W.; Murtaza, M.; Biggs, H.; Rueda, O. M.; Chin, S. F.; Dunning, M. J.; Gale, D.; Forshew, T.; Mahler-Araujo, B.; Rajan, S.; Humphray, S.; Becq, J.; Halsall, D.; Wallis, M.; Bentley, D.; Caldas, C.; Rosenfeld, N. *N. Engl. J. Med.* **2013**, *368*, 1199-1209.
(29) Olsson, E.; Winter, C.; George, A.; Chen, Y.; Howlin, J.; Tang, M. H.; Dahlgren, M.; Schulz, R.; Grabau, D.; van Westen, D.; Ferno, M.; Ingvar, C.; Rose, C.; Bendahl, P. O.; Ryden, L.; Borg, A.; Gruvberger-Saal, S. K.; Jernstrom, H.; Saal, L. H. *EMBO Mol. Med.* **2015**, *7*, 1034-1047.
(30) Fackler, M. J.; Lopez Bujanda, Z.; Umbricht, C.; Teo, W. W.; Cho, S.; Zhang, Z.; Visvanathan, K.; Jeter, S.; Argani, P.; Wang, C.; Lyman, J. P.; de Brot, M.; Ingle, J. N.; Boughey, J.; McGuire, K.; King, T. A.; Carey, L. A.; Cope, L.; Wolff, A. C.; Sukumar, S. *Cancer Res.* **2014**, *74*, 2160-2170.
(31) Gray, E. S.; Rizos, H.; Reid, A. L.; Boyd, S. C.; Pereira, M. R.; Lo, J.; Tembe, V.; Freeman, J.; Lee, J. H.; Scolyer, R. A.; Siew, K.; Lomma, C.; Cooper, A.; Khattak, M. A.; Meniawy, T. M.; Long, G. V.; Carlino, M. S.; Millward, M.; Ziman, M. *Oncotarget* **2015**, *6*, 42008-42018.
(32) Riethdorf, S.; O'Flaherty, L.; Hille, C.; Pantel, K. *Adv. Drug Del. Rev.* **2018**, *125*, 102-121.
(33) Kwapisz, D. *Ann. Transl. Med.* **2017**, *5*, 46.
(34) Miller, M. C.; Doyle, G. V.; Terstappen, L. W. *J. Oncol.* **2010**, *2010*, 617421.
(35) Blumenreich, M. S. In *Clinical Methods: The History, Physical, and Laboratory Examinations*, 3rd ed.; Walker, H. K.; Hall, W. D.; Hurst, J. W., Eds.; Butterworths: Boston, 1990, pp 724-727.
(36) Barrett, K. E.; Barman, S. M.; Brooks, H. L.; Yuan, J. X.-J. In *Ganong's Review of Medical Physiology*, 26th ed.; Weitz, M.; Boyle, P. J., Eds.; McGraw-Hill Education: New York, NY, 2019, pp 543-574.
(37) van Niel, G.; D'Angelo, G.; Raposo, G. *Nat. Rev. Mol. Cell Biol.* **2018**, *19*, 213-228.
(38) Raposo, G.; Stoorvogel, W. *J. Cell Biol.* **2013**, *200*, 373-383.
(39) Slomka, A.; Urban, S. K.; Lukacs-Kornek, V.; Zekanowska, E.; Kornek, M. *Front. Immunol.* **2018**, *9*, 2723.
(40) Thery, C. *F1000 Biol. Rep.* **2011**, *3*, 15.
(41) Pan, B. T.; Johnstone, R. M. *Cell* **1983**, *33*, 967-978.
(42) Maia, J.; Caja, S.; Strano Moraes, M. C.; Couto, N.; Costa-Silva, B. *Front. Cell Dev. Biol.* **2018**, *6*, 18.

(43) Meldolesi, J. *Curr. Biol.* **2018**, *28*, R435-R444.
(44) Weidle, U. H.; Birzele, F.; Kollmorgen, G.; Ruger, R. *Cancer Genom. Proteom.* **2017**, *14*, 1-15.
(45) Costa-Silva, B.; Aiello, N. M.; Ocean, A. J.; Singh, S.; Zhang, H.; Thakur, B. K.; Becker, A.; Hoshino, A.; Mark, M. T.; Molina, H.; Xiang, J.; Zhang, T.; Theilen, T. M.; Garcia-Santos, G.; Williams, C.; Ararso, Y.; Huang, Y.; Rodrigues, G.; Shen, T. L.; Labori, K. J., et al. *Nat. Cell Biol.* **2015**, *17*, 816-826.
(46) Melo, S. A.; Sugimoto, H.; O'Connell, J. T.; Kato, N.; Villanueva, A.; Vidal, A.; Qiu, L.; Vitkin, E.; Perelman, L. T.; Melo, C. A.; Lucci, A.; Ivan, C.; Calin, G. A.; Kalluri, R. *Cancer Cell* **2014**, *26*, 707-721.
(47) O'Brien, K.; Rani, S.; Corcoran, C.; Wallace, R.; Hughes, L.; Friel, A. M.; McDonnell, S.; Crown, J.; Radomski, M. W.; O'Driscoll, L. *Eur. J. Cancer* **2013**, *49*, 1845-1859.
(48) Melo, S. A.; Luecke, L. B.; Kahlert, C.; Fernandez, A. F.; Gammon, S. T.; Kaye, J.; LeBleu, V. S.; Mittendorf, E. A.; Weitz, J.; Rahbari, N.; Reissfelder, C.; Pilarsky, C.; Fraga, M. F.; Piwnica-Worms, D.; Kalluri, R. *Nature* **2015**, *523*, 177-182.
(49) Muller, L.; Hong, C. S.; Stolz, D. B.; Watkins, S. C.; Whiteside, T. L. *J. Immunol. Methods* **2014**, *411*, 55-65.
(50) Bellingham, S. A.; Guo, B. B.; Coleman, B. M.; Hill, A. F. *Front. Physiol.* **2012**, *3*, 124.
(51) Palmirotta, R.; Lovero, D.; Cafforio, P.; Felici, C.; Mannavola, F.; Pelle, E.; Quaresmini, D.; Tucci, M.; Silvestris, F. *Ther. Adv. Med. Oncol.* **2018**, *10*, 1758835918794630.
(52) Witwer, K. W.; Buzas, E. I.; Bemis, L. T.; Bora, A.; Lasser, C.; Lotvall, J.; Nolte-'t Hoen, E. N.; Piper, M. G.; Sivaraman, S.; Skog, J.; Thery, C.; Wauben, M. H.; Hochberg, F. *J. Extracell. Vesicles* **2013**, *2*, 20360.
(53) Li, X.; Corbett, A. L.; Taatizadeh, E.; Tasnim, N.; Little, J. P.; Garnis, C.; Daugaard, M.; Guns, E.; Hoorfar, M.; Li, I. T. S. *APL Bioeng* **2019**, *3*, 011503.
(54) Armstrong, D.; Wildman, D. E. *J. Pathol. Transl Med.* **2018**, *52*, 1-8.
(55) Ding, M.; Wang, C.; Lu, X.; Zhang, C.; Zhou, Z.; Chen, X.; Zhang, C. Y.; Zen, K.; Zhang, C. *Anal Bioanal Chem* **2018**, *410*, 3805-3814.
(56) Li, W.; Li, C.; Zhou, T.; Liu, X.; Liu, X.; Li, X.; Chen, D. *Mol. Cancer* **2017**, *16*, 145.
(57) Wu, T. L.; Sun, Y. C.; Chang, P. Y.; Tsao, K. C.; Sun, C. F.; Wu, J. T. *J. Clin. Lab. Anal.* **2003**, *17*, 241-246.
(58) Cassaday, J.; Shah, T.; Murray, J.; O'Donnell, G. T.; Kornienko, O.; Strulovici, B.; Ferrer, M.; Zuck, P. *Assay Drug Dev. Technol.* **2007**, *5*, 493-500.
(59) Hermanson, G. T. *Bioconjugate Techniques*, 3rd ed.; Elsevier, Academic Press: Waltham, MA, 2013.
(60) Wong, L. S.; Khan, F.; Micklefield, J. *Chem Rev* **2009**, *109*, 4025-4053.
(61) Reinholt, S. J.; Baeumner, A. J. *Angew Chem Int Ed Engl* **2014**, *53*, 13988-14001.
(62) Bienvenue, J. M.; Legendre, L. A.; Ferrance, J. P.; Landers, J. P. *Forensic Sci. Int. Genet.* **2010**, *4*, 178-186.
(63) Gossett, D. R.; Weaver, W. M.; Mach, A. J.; Hur, S. C.; Tse, H. T.; Lee, W.; Amini, H.; Di Carlo, D. *Anal Bioanal Chem* **2010**, *397*, 3249-3267.
(64) Mogensen, K. B.; Klank, H.; Kutter, J. P. *Electrophoresis* **2004**, *25*, 3498-3512.

(65) Terry, S. C.; Jerman, J. H.; Angell, J. B. *IEEE Trans. Electron Devices* **1979**, *26*, 1880-1886.
(66) Harrison, D. J.; Fluri, K.; Seiler, K.; Fan, Z.; Effenhauser, C. S.; Manz, A. *Science* **1993**, *261*, 895-897.
(67) Martinez, A. W.; Phillips, S. T.; Butte, M. J.; Whitesides, G. M. *Angew Chem Int Ed Engl* **2007**, *46*, 1318-1320.
(68) Duffy, D. C.; McDonald, J. C.; Schueller, O. J.; Whitesides, G. M. *Anal. Chem.* **1998**, *70*, 4974-4984.
(69) Becker, H.; Gartner, C. *Anal Bioanal Chem* **2008**, *390*, 89-111.
(70) Unger, M. A.; Chou, H. P.; Thorsen, T.; Scherer, A.; Quake, S. R. *Science* **2000**, *288*, 113-116.
(71) Thorsen, T.; Maerkl, S. J.; Quake, S. R. *Science* **2002**, *298*, 580-584.
(72) Studer, V.; Hang, G.; Pandolfi, A.; Ortiz, M.; French Anderson, W.; Quake, S. R. *J. Appl. Phys.* **2004**, *95*, 393-398.
(73) Hosokawa, K.; Maeda, R. *J. Micromech. Microeng.* **2000**, *10*, 415-420.
(74) Grover, W. H.; Skelley, A. M.; Liu, C. N.; Lagally, E. T.; Mathies, R. A. *Sens. Actuators B Chem.* **2003**, *89*, 315-323.
(75) Irimia, D.; Liu, S. Y.; Tharp, W. G.; Samadani, A.; Toner, M.; Poznansky, M. C. *Lab Chip* **2006**, *6*, 191-198.
(76) Au, A. K.; Lai, H.; Utela, B. R.; Folch, A. *Micromachines* **2011**, *2*, 179-220.
(77) Herr, A. E.; Hatch, A. V.; Throckmorton, D. J.; Tran, H. M.; Brennan, J. S.; Giannobile, W. V.; Singh, A. K. *Proc. Natl. Acad. Sci. U. S. A.* **2007**, *104*, 5268-5273.
(78) Zheng, C.; Wang, J.; Pang, Y.; Wang, J.; Li, W.; Ge, Z.; Huang, Y. *Lab Chip* **2012**, *12*, 2487-2490.
(79) Yang, Y.; Zeng, Y. *Lab Chip* **2018**, *18*, 3830-3839.
(80) Zhou, X.; Ravichandran, G. C.; Zhang, P.; Yang, Y.; Zeng, Y. *Lab Chip* **2019**, *19*, 4104-4116.
(81) Pal, R.; Yang, M.; Lin, R.; Johnson, B. N.; Srivastava, N.; Razzacki, S. Z.; Chomistek, K. J.; Heldsinger, D. C.; Haque, R. M.; Ugaz, V. M.; Thwar, P. K.; Chen, Z.; Alfano, K.; Yim, M. B.; Krishnan, M.; Fuller, A. O.; Larson, R. G.; Burke, D. T.; Burns, M. A. *Lab Chip* **2005**, *5*, 1024-1032.
(82) Pekin, D.; Skhiri, Y.; Baret, J. C.; Le Corre, D.; Mazutis, L.; Salem, C. B.; Millot, F.; El Harrak, A.; Hutchison, J. B.; Larson, J. W.; Link, D. R.; Laurent-Puig, P.; Griffiths, A. D.; Taly, V. *Lab Chip* **2011**, *11*, 2156-2166.
(83) Cheng, X.; Irimia, D.; Dixon, M.; Sekine, K.; Demirci, U.; Zamir, L.; Tompkins, R. G.; Rodriguez, W.; Toner, M. *Lab Chip* **2007**, *7*, 170-178.
(84) Baret, J. C.; Miller, O. J.; Taly, V.; Ryckelynck, M.; El-Harrak, A.; Frenz, L.; Rick, C.; Samuels, M. L.; Hutchison, J. B.; Agresti, J. J.; Link, D. R.; Weitz, D. A.; Griffiths, A. D. *Lab Chip* **2009**, *9*, 1850-1858.
(85) Wang, M. M.; Tu, E.; Raymond, D. E.; Yang, J. M.; Zhang, H.; Hagen, N.; Dees, B.; Mercer, E. M.; Forster, A. H.; Kariv, I.; Marchand, P. J.; Butler, W. F. *Nat. Biotechnol.* **2005**, *23*, 83-87.
(86) Lan, F.; Demaree, B.; Ahmed, N.; Abate, A. R. *Nat. Biotechnol.* **2017**, *35*, 640-646.
(87) Abate, A. R.; Hung, T.; Sperling, R. A.; Mary, P.; Rotem, A.; Agresti, J. J.; Weiner, M. A.; Weitz, D. A. *Lab Chip* **2013**, *13*, 4864-4869.
(88) Dittrich, P. S.; Manz, A. *Nat. Rev. Drug Discov.* **2006**, *5*, 210-218.

(89) Kang, L.; Chung, B. G.; Langer, R.; Khademhosseini, A. *Drug Discov. Today* **2008**, *13*, 1-13.
(90) Stephenson, W.; Donlin, L. T.; Butler, A.; Rozo, C.; Bracken, B.; Rashidfarrokhi, A.; Goodman, S. M.; Ivashkiv, L. B.; Bykerk, V. P.; Orange, D. E.; Darnell, R. B.; Swerdlow, H. P.; Satija, R. *Nat. Commun.* **2018**, *9*, 791.
(91) Streets, A. M.; Zhang, X.; Cao, C.; Pang, Y.; Wu, X.; Xiong, L.; Yang, L.; Fu, Y.; Zhao, L.; Tang, F.; Huang, Y. *Proc. Natl. Acad. Sci. U. S. A.* **2014**, *111*, 7048-7053.
(92) White, A. K.; VanInsberghe, M.; Petriv, O. I.; Hamidi, M.; Sikorski, D.; Marra, M. A.; Piret, J.; Aparicio, S.; Hansen, C. L. *Proc. Natl. Acad. Sci. U. S. A.* **2011**, *108*, 13999-14004.
(93) Qin, Y.; Wu, L.; Schneider, T.; Yen, G. S.; Wang, J.; Xu, S.; Li, M.; Paguirigan, A. L.; Smith, J. L.; Radich, J. P.; Anand, R. K.; Chiu, D. T. *Angew. Chem. Int. Ed. Engl.* **2018**, *57*, 11378-11383.
(94) Huang, S. B.; Wu, M. H.; Lin, Y. H.; Hsieh, C. H.; Yang, C. L.; Lin, H. C.; Tseng, C. P.; Lee, G. B. *Lab Chip* **2013**, *13*, 1371-1383.
(95) Dharmasiri, U.; Njoroge, S. K.; Witek, M. A.; Adebiyi, M. G.; Kamande, J. W.; Hupert, M. L.; Barany, F.; Soper, S. A. *Anal. Chem.* **2011**, *83*, 2301-2309.
(96) Kim, C. J.; Park, J.; Sunkara, V.; Kim, T. H.; Lee, Y.; Lee, K.; Kim, M. H.; Cho, Y. K. *Lab Chip* **2018**, *18*, 1320-1329.
(97) Gorgannezhad, L.; Umer, M.; Islam, M. N.; Nguyen, N. T.; Shiddiky, M. J. A. *Lab Chip* **2018**, *18*, 1174-1196.
(98) He, M.; Zeng, Y. *J. Lab. Autom.* **2016**, *21*, 599-608.
(99) Zhao, Z.; Yang, Y.; Zeng, Y.; He, M. *Lab Chip* **2016**, *16*, 489-496.
(100) Rissin, D. M.; Kan, C. W.; Campbell, T. G.; Howes, S. C.; Fournier, D. R.; Song, L.; Piech, T.; Patel, P. P.; Chang, L.; Rivnak, A. J.; Ferrell, E. P.; Randall, J. D.; Provuncher, G. K.; Walt, D. R.; Duffy, D. C. *Nat. Biotechnol.* **2010**, *28*, 595-599.
(101) Yung, T. K.; Chan, K. C.; Mok, T. S.; Tong, J.; To, K. F.; Lo, Y. M. *Clin Cancer Res* **2009**, *15*, 2076-2084.
(102) Walt, D. R. *Anal. Chem.* **2013**, *85*, 1258-1263.
(103) Guo, M. T.; Rotem, A.; Heyman, J. A.; Weitz, D. A. *Lab Chip* **2012**, *12*, 2146-2155.
(104) Teh, S. Y.; Lin, R.; Hung, L. H.; Lee, A. P. *Lab Chip* **2008**, *8*, 198-220.
(105) Shembekar, N.; Chaipan, C.; Utharala, R.; Merten, C. A. *Lab Chip* **2016**, *16*, 1314-1331.
(106) Witters, D.; Knez, K.; Ceyssens, F.; Puers, R.; Lammertyn, J. *Lab Chip* **2013**, *13*, 2047-2054.
(107) Decrop, D.; Pardon, G.; Brancato, L.; Kil, D.; Zandi Shafagh, R.; Kokalj, T.; Haraldsson, T.; Puers, R.; van der Wijngaart, W.; Lammertyn, J. *ACS Appl. Mater. Interfaces* **2017**, *9*, 10418-10426.
(108) Ottesen, E. A.; Hong, J. W.; Quake, S. R.; Leadbetter, J. R. *Science* **2006**, *314*, 1464-1467.
(109) Sun, Y.; Zhou, X.; Yu, Y. *Lab Chip* **2014**, *14*, 3603-3610.
(110) Trantidou, T.; Friddin, M. S.; Salehi-Reyhani, A.; Ces, O.; Elani, Y. *Lab Chip* **2018**, *18*, 2488-2509.
(111) Duan, B. K.; Cavanagh, P. E.; Li, X.; Walt, D. R. *Anal. Chem.* **2018**, *90*, 3091-3098.

(112) Wendler, F.; Bota-Rabassedas, N.; Franch-Marro, X. *J. Extracell. Vesicles* **2013**, *2*, 22390.
(113) Alderton, G. K. *Nat. Rev. Cancer* **2012**, *12*, 447.
(114) Camussi, G.; Deregibus, M. C.; Bruno, S.; Cantaluppi, V.; Biancone, L. *Kidney Int.* **2010**, *78*, 838-848.
(115) Théry, C.; Zitvogel, L.; Amigorena, S. *Nat. Rev. Immunol.* **2002**, *2*, 569-579.
(116) Iero, M.; Valenti, R.; Huber, V.; Filipazzi, P.; Parmiani, G.; Fais, S.; Rivoltini, L. *Cell Death Differ.* **2008**, *15*, 80-88.
(117) Alikhani, V. S.; Malmer, A.; Ekstrom, K.; Bossios, A.; Sjostrand, M.; Lotvall, J. *Allergy* **2007**, *62*, 452.
(118) Valero Liñán, A. S.; Serrano-Heras, G.; Cifuentes Tebar, J.; González Masiá, J. A.; Miota de Llama, J. I.; Rueda Martínez, J. L.; Prat Calero, A.; Abad Martínez, M.; Moreno Flores, B.; Bueno Lozano, G.; Osorio Manyari, A. A.; Camacho Dorado, C.; Cascales Sánchez, P.; González Masegosa, P. *Br. J. Surg.* **2015**, *102*, 8.
(119) Alderton, G. K. *Nat. Rev. Cancer* **2015**, *15*, 453.
(120) Momen-Heravi, F.; Balaj, L.; Alian, S.; Mantel, P. Y.; Halleck, A. E.; Trachtenberg, A. J.; Soria, C. E.; Oquin, S.; Bonebreak, C. M.; Saracoglu, E.; Skog, J.; Kuo, W. P. *Biol. Chem.* **2013**, *394*, 1253-1262.
(121) Greening, D. W.; Xu, R.; Ji, H.; Tauro, B. J.; Simpson, R. J. *Methods Mol. Biol.* **2015**, *1295*, 179-209.
(122) Taylor, D. D.; Zacharias, W.; Gercel-Taylor, C. *Methods Mol. Biol.* **2011**, *728*, 235-246.
(123) Jeppesen, D. K.; Hvam, M. L.; Primdahl-Bengtson, B.; Boysen, A. T.; Whitehead, B.; Dyrskjot, L.; Orntoft, T. F.; Howard, K. A.; Ostenfeld, M. S. *J. Extracell. Vesicles* **2014**, *3*, 25011.
(124) Li, M.; Rai, A. J.; DeCastro, G. J.; Zeringer, E.; Barta, T.; Magdaleno, S.; Setterquist, R.; Vlassov, A. V. *Methods* **2015**, *87*, 26-30.
(125) Schageman, J.; Zeringer, E.; Li, M.; Barta, T.; Lea, K.; Gu, J.; Magdaleno, S.; Setterquist, R.; Vlassov, A. V. *BioMed Res. Int.* **2013**, *2013*, 253957.
(126) Rekker, K.; Saare, M.; Roost, A. M.; Kubo, A. L.; Zarovni, N.; Chiesi, A.; Salumets, A.; Peters, M. *Clin. Biochem.* **2014**, *47*, 135-138.
(127) Lobb, R. J.; Becker, M.; Wen, S. W.; Wong, C. S.; Wiegmans, A. P.; Leimgruber, A.; Moller, A. *J. Extracell. Vesicles* **2015**, *4*, 27031.
(128) Peng, P.; Yan, Y.; Keng, S. *Oncol. Rep.* **2011**, *25*, 749-762.
(129) Beach, A.; Zhang, H. G.; Ratajczak, M. Z.; Kakar, S. S. *J Ovarian Res.* **2014**, *7*, 14.
(130) Fontana, S.; Saieva, L.; Taverna, S.; Alessandro, R. *Proteomics* **2013**, *13*, 1581-1594.
(131) Aliotta, J. M. *J. Gastrointest. Oncol.* **2011**, *2*, 203-205.
(132) Kalra, H.; Adda, C. G.; Liem, M.; Ang, C. S.; Mechler, A.; Simpson, R. J.; Hulett, M. D.; Mathivanan, S. *Proteomics* **2013**, *13*, 3354-3364.
(133) Koga, K.; Matsumoto, K.; Akiyoshi, T.; Kubo, M.; Yamanaka, N.; Tasaki, A.; Nakashima, H.; Nakamura, M.; Kuroki, S.; Tanaka, M.; Katano, M. *Anticancer Res.* **2005**, *25*, 3703-3707.
(134) Liga, A.; Vliegenthart, A. D.; Oosthuyzen, W.; Dear, J. W.; Kersaudy-Kerhoas, M. *Lab Chip* **2015**, *15*, 2388-2394.

(135) He, M.; Crow, J.; Roth, M.; Zeng, Y.; Godwin, A. K. *Lab Chip* **2014**, *14*, 3773-3780.
(136) Davies, R. T.; Kim, J.; Jang, S. C.; Choi, E. J.; Gho, Y. S.; Park, J. *Lab Chip* **2012**, *12*, 5202-5210.
(137) Santana, S. M.; Antonyak, M. A.; Cerione, R. A.; Kirby, B. J. *Biomed. Microdevices* **2014**, *16*, 869-877.
(138) Kanwar, S. S.; Dunlay, C. J.; Simeone, D. M.; Nagrath, S. *Lab Chip* **2014**, *14*, 1891-1900.
(139) Zhu, L.; Wang, K.; Cui, J.; Liu, H.; Bu, X.; Ma, H.; Wang, W.; Gong, H.; Lausted, C.; Hood, L.; Yang, G.; Hu, Z. *Anal. Chem.* **2014**, *86*, 8857-8864.
(140) Vaidyanathan, R.; Naghibosadat, M.; Rauf, S.; Korbie, D.; Carrascosa, L. G.; Shiddiky, M. J.; Trau, M. *Anal. Chem.* **2014**, *86*, 11125-11132.
(141) Im, H.; Shao, H.; Park, Y. I.; Peterson, V. M.; Castro, C. M.; Weissleder, R.; Lee, H. *Nat. Biotechnol.* **2014**, *32*, 490-495.
(142) Shao, H.; Chung, J.; Balaj, L.; Charest, A.; Bigner, D. D.; Carter, B. S.; Hochberg, F. H.; Breakefield, X. O.; Weissleder, R.; Lee, H. *Nat. Med.* **2012**, *18*, 1835-1840.
(143) Thomas, S. N.; Liao, Z.; Clark, D.; Chen, Y.; Samadani, R.; Mao, L.; Ann, D. K.; Baulch, J. E.; Shapiro, P.; Yang, A. J. *Proteomes* **2013**, *1*, 87-108.
(144) Ji, H.; Greening, D. W.; Barnes, T. W.; Lim, J. W.; Tauro, B. J.; Rai, A.; Xu, R.; Adda, C.; Mathivanan, S.; Zhao, W.; Xue, Y.; Xu, T.; Zhu, H. J.; Simpson, R. J. *Proteomics* **2013**, *13*, 1672-1686.
(145) Crescitelli, R.; Lässer, C.; Szabó, T. G.; Kittel, A.; Eldh, M.; Dianzani, I.; Buzás, E. I.; Lötvall, J. *J. Extracell. Vesicles* **2013**, *2*, 20677.
(146) Tauro, B. J.; Greening, D. W.; Mathias, R. A.; Ji, H.; Mathivanan, S.; Scott, A. M.; Simpson, R. J. *Methods* **2012**, *56*, 293-304.
(147) Bobrie, A.; Colombo, M.; Krumeich, S.; Raposo, G.; Théry, C. *J. Extracell. Vesicles* **2012**, *1*, 18397.
(148) Jiang, F.; Drese, K. S.; Hardt, S.; Küpper, M.; Schönfeld, F. *AIChE J.* **2004**, *50*, 2297-2305.
(149) Martel, J. M.; Toner, M. *Sci. Rep.* **2013**, *3*, 3340.
(150) Ng, A. H. C.; Uddayasankar, U.; Wheeler, A. R. *Anal. Bioanal. Chem.* **2010**, *397*, 991-1007.
(151) Lamparski, H. G.; Metha-Damani, A.; Yao, J. Y.; Patel, S.; Hsu, D. H.; Ruegg, C.; Le Pecq, J. B. *J. Immunol. Methods* **2002**, *270*, 211-226.
(152) Kharaziha, P.; Ceder, S.; Li, Q.; Panaretakis, T. *Biochim. Biophys. Acta* **2012**, *1826*, 103-111.
(153) Mahaweni, N. M.; Kaijen-Lambers, M. E. H.; Dekkers, J.; Aerts, J. G. J. V.; Hegmans, J. P. J. J. *J. Extracell. Vesicles* **2013**, *2*, 22492.
(154) Runz, S.; Keller, S.; Rupp, C.; Stoeck, A.; Issa, Y.; Koensgen, D.; Mustea, A.; Sehouli, J.; Kristiansen, G.; Altevogt, P. *Gynecol. Oncol.* **2007**, *107*, 563-571.
(155) Liang, B.; Peng, P.; Chen, S.; Li, L.; Zhang, M.; Cao, D.; Yang, J.; Li, H.; Gui, T.; Li, X.; Shen, K. *J. Proteomics* **2013**, *80*, 171-182.
(156) Kristiansen, G.; Denkert, C.; Schluns, K.; Dahl, E.; Pilarsky, C.; Hauptmann, S. *Am. J. Pathol.* **2002**, *161*, 1215-1221.
(157) Nolen, B. M.; Lokshin, A. E. *Mol. Diagn. Ther.* **2013**, *17*, 139-146.

(158) Sokolova, V.; Ludwig, A. K.; Hornung, S.; Rotan, O.; Horn, P. A.; Epple, M.; Giebel, B. *Colloids Surf. B. Biointerfaces* **2011**, *87*, 146-150.
(159) Suresh, K. P.; Chandrashekara, S. *J. Hum. Reprod. Sci.* **2012**, *5*, 7-13.
(160) van Stralen, K. J.; Stel, V. S.; Reitsma, J. B.; Dekker, F. W.; Zoccali, C.; Jager, K. J. *Kidney Int.* **2009**, *75*, 1257-1263.
(161) Zou, K. H.; O'Malley, A. J.; Mauri, L. *Circulation* **2007**, *115*, 654-657.
(162) van der Pol, E.; Coumans, F. A. W.; Grootemaat, A. E.; Gardiner, C.; Sargent, I. L.; Harrison, P.; Sturk, A.; van Leeuwen, T. G.; Nieuwland, R. *J. Thromb. Haemost.* **2014**, *12*, 1182-1192.
(163) Srivastava, A.; Filant, J.; Moxley, K. M.; Sood, A.; McMeekin, S.; Ramesh, R. *Curr. Gene Ther.* **2015**, *15*, 182-192.
(164) Tighe, P. J.; Ryder, R. R.; Todd, I.; Fairclough, L. C. *Proteomics Clin. Appl.* **2015**, *9*, 406-422.
(165) Omi, K.; Ando, T.; Sakyu, T.; Shirakawa, T.; Uchida, Y.; Oka, A.; Ise, N.; Aoyagi, K.; Goishi, K. *Clin. Chem.* **2015**, *61*, 627-635.
(166) Zhang, P.; He, M.; Zeng, Y. *Lab Chip* **2016**, *16*, 3033-3042.
(167) Yu, X.; Xia, Y.; Tang, Y.; Zhang, W. L.; Yeh, Y. T.; Lu, H.; Zheng, S. Y. *Small* **2017**, *13*, 1700425.
(168) Ahmed, A.; Rushworth, J. V.; Hirst, N. A.; Millner, P. A. *Clin. Microbiol. Rev.* **2014**, *27*, 631-646.
(169) Myung, J. H.; Hong, S. *Lab Chip* **2015**, *15*, 4500-4511.
(170) Zeng, Y.; Wang, T. *Anal. Bioanal. Chem.* **2013**, *405*, 5743-5758.
(171) Chiu, D. T.; deMello, A. J.; Di Carlo, D.; Doyle, P. S.; Hansen, C.; Maceiczyk, R. M.; Wootton, R. C. R. *Chem* **2017**, *2*, 201-223.
(172) Han, K. N.; Li, C. A.; Seong, G. H. *Annu. Rev. Anal. Chem.* **2013**, *6*, 119-141.
(173) Hughes, A. J.; Spelke, D. P.; Xu, Z.; Kang, C. C.; Schaffer, D. V.; Herr, A. E. *Nat. Methods* **2014**, *11*, 749-755.
(174) Sinkala, E.; Sollier-Christen, E.; Renier, C.; Rosas-Canyelles, E.; Che, J.; Heirich, K.; Duncombe, T. A.; Vlassakis, J.; Yamauchi, K. A.; Huang, H.; Jeffrey, S. S.; Herr, A. E. *Nat. Commun.* **2017**, *8*, 14622.
(175) Lu, Y.; Xue, Q.; Eisele, M. R.; Sulistijo, E. S.; Brower, K.; Han, L.; Amir el, A. D.; Pe'er, D.; Miller-Jensen, K.; Fan, R. *Proc. Natl. Acad. Sci. U. S. A.* **2015**, *112*, E607-615.
(176) Cui, X.; Liu, Y.; Hu, D.; Qian, W.; Tin, C.; Sun, D.; Chen, W.; Lam, R. H. W. *Lab Chip* **2018**, *18*, 522-531.
(177) Mauk, M.; Song, J.; Bau, H. H.; Gross, R.; Bushman, F. D.; Collman, R. G.; Liu, C. *Lab Chip* **2017**, *17*, 382-394.
(178) Song, Y.; Zhang, Y.; Bernard, P. E.; Reuben, J. M.; Ueno, N. T.; Arlinghaus, R. B.; Zu, Y.; Qin, L. *Nat. Commun.* **2012**, *3*, 1283.
(179) Xue, Q.; Bettini, E.; Paczkowski, P.; Ng, C.; Kaiser, A.; McConnell, T.; Kodrasi, O.; Quigley, M. F.; Heath, J.; Fan, R.; Mackay, S.; Dudley, M. E.; Kassim, S. H.; Zhou, J. *J. ImmunoTher. Cancer* **2017**, *5*, 85.
(180) Peterson, V. M.; Castro, C. M.; Chung, J.; Miller, N. C.; Ullal, A. V.; Castano, M. D.; Penson, R. T.; Lee, H.; Birrer, M. J.; Weissleder, R. *Proc. Natl. Acad. Sci. U. S. A.* **2013**, *110*, E4978-4986.
(181) Wang, T.; Zhang, M.; Dreher, D. D.; Zeng, Y. *Lab Chip* **2013**, *13*, 4190-4197.
(182) Gao, R.; Cheng, Z.; deMello, A. J.; Choo, J. *Lab Chip* **2016**, *16*, 1022-1029.

(183) Yu, Z. T.; Guan, H.; Cheung, M. K.; McHugh, W. M.; Cornell, T. T.; Shanley, T. P.; Kurabayashi, K.; Fu, J. *Sci. Rep.* **2015**, *5*, 11339.
(184) Bechstein, D. J.; Lee, J. R.; Ooi, C. C.; Gani, A. W.; Kim, K.; Wilson, R. J.; Wang, S. X. *Sci. Rep.* **2015**, *5*, 11693.
(185) Serra, M.; Ferraro, D.; Pereiro, I.; Viovy, J. L.; Descroix, S. *Lab Chip* **2017**, *17*, 3979-3999.
(186) Shikida, M.; Takayanagi, K.; Inouchi, K.; Honda, H.; Sato, K. *Sens. Actuators B Chem.* **2006**, *113*, 563-569.
(187) Shi, X.; Chen, C. H.; Gao, W.; Chao, S. H.; Meldrum, D. R. *Lab Chip* **2015**, *15*, 1059-1065.
(188) Okochi, M.; Tsuchiya, H.; Kumazawa, F.; Shikida, M.; Honda, H. *J. Biosci. Bioeng.* **2010**, *109*, 193-197.
(189) Chen, H.; Abolmatty, A.; Faghri, M. *Microfluid. Nanofluid.* **2010**, *10*, 593-605.
(190) den Dulk, R. C.; Schmidt, K. A.; Sabatte, G.; Liebana, S.; Prins, M. W. *Lab Chip* **2013**, *13*, 106-118.
(191) Berry, S. M.; Alarid, E. T.; Beebe, D. J. *Lab Chip* **2011**, *11*, 1747-1753.
(192) Berry, S. M.; Maccoux, L. J.; Beebe, D. J. *Anal. Chem.* **2012**, *84*, 5518-5523.
(193) Casavant, B. P.; Guckenberger, D. J.; Berry, S. M.; Tokar, J. T.; Lang, J. M.; Beebe, D. J. *Lab Chip* **2013**, *13*, 391-396.
(194) Berry, S. M.; Pezzi, H. M.; LaVanway, A. J.; Guckenberger, D. J.; Anderson, M. A.; Beebe, D. J. *ACS Appl. Mater. Interfaces* **2016**, *8*, 15040-15045.
(195) Liu, W.; Chen, D.; Du, W.; Nichols, K. P.; Ismagilov, R. F. *Anal. Chem.* **2010**, *82*, 3276-3282.
(196) Tsuchiya, H.; Okochi, M.; Nagao, N.; Shikida, M.; Honda, H. *Sens. Actuators B Chem.* **2008**, *130*, 583-588.
(197) Long, Z.; Shetty, A. M.; Solomon, M. J.; Larson, R. G. *Lab Chip* **2009**, *9*, 1567-1575.
(198) Duffy, M. J. *Clin. Chem.* **2001**, *47*, 624-630.
(199) John, T.; Liu, G.; Tsao, M. S. *Oncogene* **2009**, *28*, S14-S23.
(200) Barbosa, A. I.; Reis, N. M. *Analyst* **2017**, *142*, 858-882.
(201) Wu, Y.; Xue, P.; Kang, Y.; Hui, K. M. *Anal. Chem.* **2013**, *85*, 8661-8668.
(202) Tian, L.; Liu, L.; Li, Y.; Wei, Q.; Cao, W. *Sci. Rep.* **2016**, *6*, 30849.
(203) Wang, H.; Wang, Y.; Zhang, Y.; Wang, Q.; Ren, X.; Wu, D.; Wei, Q. *Sci. Rep.* **2016**, *6*, 27385.
(204) Li, X.-H.; Sun, W.-M.; Wu, J.; Gao, Y.; Chen, J.-H.; Chen, M.; Ou, Q.-S. *Anal. Methods* **2018**, *10*, 1552-1559.
(205) Gaster, R. S.; Hall, D. A.; Nielsen, C. H.; Osterfeld, S. J.; Yu, H.; Mach, K. E.; Wilson, R. J.; Murmann, B.; Liao, J. C.; Gambhir, S. S.; Wang, S. X. *Nat. Med.* **2009**, *15*, 1327-1332.
(206) Obayashi, Y.; Iino, R.; Noji, H. *Analyst* **2015**, *140*, 5065-5073.
(207) Rissin, D. M.; Fournier, D. R.; Piech, T.; Kan, C. W.; Campbell, T. G.; Song, L.; Chang, L.; Rivnak, A. J.; Patel, P. P.; Provuncher, G. K.; Ferrell, E. P.; Howes, S. C.; Pink, B. A.; Minnehan, K. A.; Wilson, D. H.; Duffy, D. C. *Anal. Chem.* **2011**, *83*, 2279-2285.
(208) Nam, J. M.; Thaxton, C. S.; Mirkin, C. A. *Science* **2003**, *301*, 1884-1886.

(209) Armani, A. M.; Kulkarni, R. P.; Fraser, S. E.; Flagan, R. C.; Vahala, K. J. *Science* **2007**, *317*, 783-787.
(210) Kan, C. W.; Rivnak, A. J.; Campbell, T. G.; Piech, T.; Rissin, D. M.; Mosl, M.; Peterca, A.; Niederberger, H. P.; Minnehan, K. A.; Patel, P. P.; Ferrell, E. P.; Meyer, R. E.; Chang, L.; Wilson, D. H.; Fournier, D. R.; Duffy, D. C. *Lab Chip* **2012**, *12*, 977-985.
(211) Liu, D.; Li, X.; Zhou, J.; Liu, S.; Tian, T.; Song, Y.; Zhu, Z.; Zhou, L.; Ji, T.; Yang, C. *Biosens. Bioelectron.* **2017**, *96*, 332-338.
(212) Greening, D. W.; Xu, R.; Ji, H.; Tauro, B. J.; Simpson, R. J. In *Proteomic Profiling*, 1st ed.; Posch, A., Ed.; Humana Press: New York, NY, 2015, pp 179-209.
(213) De Rubis, G.; Rajeev Krishnan, S.; Bebawy, M. *Trends Pharmacol. Sci.* **2019**, *40*, 172-186.
(214) Paragas, V. B.; Zhang, Y. Z.; Haugland, R. P.; Singer, V. L. *J. Histochem. Cytochem.* **1997**, *45*, 345-357.
(215) Paragas, V. B.; Kramer, J. A.; Fox, C.; Haugland, R. P.; Singer, V. L. *J. Microsc.* **2002**, *206*, 106-119.
(216) Lawson, D. A.; Kessenbrock, K.; Davis, R. T.; Pervolarakis, N.; Werb, Z. *Nat. Cell Biol.* **2018**, *20*, 1349-1360.
(217) Kibria, G.; Ramos, E. K.; Lee, K. E.; Bedoyan, S.; Huang, S.; Samaeekia, R.; Athman, J. J.; Harding, C. V.; Lotvall, J.; Harris, L.; Thompson, C. L.; Liu, H. *Sci. Rep.* **2016**, *6*, 36502.
(218) Liu, C.; Xu, X.; Li, B.; Situ, B.; Pan, W.; Hu, Y.; An, T.; Yao, S.; Zheng, L. *Nano Lett.* **2018**, *18*, 4226-4232.